ALTERATION IDENTIFICATION BY HYPERSPECTRAL REMOTE SENSING IN SISORTA GOLD PROSPECT
(SİVAS-TURKEY)

A THESIS SUBMITTED TO
THE GRADUATE SCHOOL OF NATURAL AND APPLIED SCIENCES
OF
MIDDLE EAST TECHNICAL UNIVERSITY

BY

ERDEM YETKİN

IN PARTIAL FULFILLMENT OF THE REQUIREMENTS
FOR
THE DEGREE OF DOCTOR OF PHILOSOPHY
IN
GEOLOGICAL ENGINEERING

SEPTEMBER 2009

Approval of the thesis:

ALTERATION IDENTIFICATION BY HYPERSPECTRAL REMOTE SENSING IN SISORTA GOLD PROSPECT (SİVAS-TURKEY)

submitted by **ERDEM YETKİN** in partial fulfillment of the requirements for the degree of **Doctor of Philosophy in Geological Engineering Department, Middle East Technical University** by,

Prof. Dr. Canan Özgen _____________________
Dean, Graduate School of **Natural and Applied Sciences**

Prof. Dr. Zeki Çamur _____________________
Head of Department, **Geological Engineering**

Prof. Dr. Vedat Toprak _____________________
Supervisor, **Geological Engineering Dept., METU**

Examining Committee Members:

Prof. Dr. Can Ayday _____________________
Satellite and Space Res. Sci. Ins., Anadolu University

Prof. Dr. Vedat Toprak _____________________
Geological Engineering Dept., METU

Assoc. Prof. Dr. Bora Rojay _____________________
Geological Engineering Dept., METU

Assoc. Prof. Dr. Lütfi Süzen _____________________
Geological Engineering Dept., METU

Dr. Mesut Soylu _____________________
Eurasia Madencilik Ltd.

Date: 02. 09. 2009

I hereby declare that all information in this document has been obtained and presented in accordance with academic rules and ethical conduct. I also declare that, as required by these rules and conduct, I have fully cited and referenced all material and results that are not original to this work.

Name, Last Name: Erdem Yetkin

Signature:

ABSTRACT

ALTERATION IDENTIFICATION BY HYPERSPECTRAL REMOTE SENSING IN SISORTA GOLD PROSPECT (SİVAS-TURKEY)

Yetkin, Erdem
Ph.D., Department of Geological Engineering
Supervisor: Prof. Dr. Vedat Toprak

September 2009, 112 pages

Imaging spectrometry data or hyperspectral imagery acquired using airborne systems have been used in the geologic community since the early 1980's and represent a mature technology. The solar spectral range 0.4–2.5 μm provides abundant information about hydroxyl-bearing minerals, sulfates and carbonates common to many geologic units and hydrothermal alteration assemblages. Satellite based Hyperion image data is used to implement and test hyperspectral processing techniques to identify alteration minerals and associate the results with the geological setting. Sisorta gold prospect is characterized by porphyry related epithermal and mesothermal alteration zones that are mapped through field studies. Image specific corrections are applied to obtain error free image data. Extensive field mapping and spectroscopic survey are used to identify nine endmembers from the image. Partial unmixing techniques are applied and used to assess the endmembers. Finally the spectral correlation mapper is used to map the endmembers which are kaolinite, dickite, halloysite, illite, montmorillonite and alunite as clay group and hematite, goethite and jarosite as the iron oxide group. The clays and iron oxides are mapped with approximately eighty percent accuracy. The study introduces an image specific algorithm for alteration minerals identification and discusses the outcomes within the geological perspective.

Keywords: Hyperspectral, Alteration, Epithermal, Hyperion, Sisorta

ÖZ

HİPERSPEKTRAL UZAKTAN ALGILAMA İLE ALTERASYON BELİRLENMESİ: SİSORTA ALTIN SAHASI (SİVAS-TÜRKİYE)

Yetkin, Erdem
Doktora, Jeoloji Mühendisliği Bölümü
Tez Yöneticisi: Prof. Dr. Vedat Toprak

Eylül 2009, 112 sayfa

Havadan uçakla elde edilen spektrometrik imaj datası ya da hiperspektral data 1980 lerden bu yana gelişmiş bir teknoloji ile jeolojik amaçlarla kullanılmaktadır. Güneş ışığının 0.4–2.5 μm spektral aralığı hidrotermal alterasyon gruplarına özgü hidroksil içeren mineraller, sülfatlar ve karbonatlar hakkında oldukça yeterli bilgi sağlar. Alterasyon minerallerini ayıklamak ve jeolojik açıdan değerlendirmek amacıyla uygulanan ve test edilen hiperspektral analiz teknikleri Hyperion uydu görüntüsü kullanılarak gerçekleştirilmiştir. Sisorta altın cevherleşmesi bölgesi arazi çalışmalarıyla tanımlanmış porfiriye bağlı epitermal ve mezotermal alterasyon zonları içerir. Hatasiz görüntü verisi elde etmek için çekilen uydu görüntüsüne has düzeltmeler uygulanmıştır. Geniş çaplı arazi haritalaması ve spektroskopik çalışma verileri kullanılarak uydu görüntüsü verisinden dokuz mineral spektrası ayıklanmıştır. Kısmi ayrıştırma teknikleri uygulanmış ve sonuçlar mineral bazında değerlendirilmiştir. Son aşamada spektral korelasyon haritalama tekniği ile kil grubu mineralleri olan kaolinit, dikit, halloysit, illit, montmorillonit ve alünit ve demir oksit grubu mineralleri olan hematit, götit ve jarosit haritalanmıştır. Kil ve demir oksit grubu mineralleri yaklaşık yüzde seksen kesinlikle saptanmıştır. Bu çalışma ile alterasyon mineralleri ayıklanması için uydu görüntüsüne has bir algoritma önerilmiş ve sonuçları jeolojik açıdan değerlendirilmiştir.

Anahtar kelimeler: Hiperspektral, Alterasyon, Epitermal, Hyperion, Sisorta

To my beloved family

ACKNOWLEDGEMENTS

For the endless support, trust, and motivation I am very grateful and very lucky to have worked with my supervisor Prof. Dr. Vedat Toprak.

I would like to thank to Assoc. Prof. Dr. Lütfi Süzen for sharing his invaluable vision and wisdom.

I would like to thank to Dr. Mesut Soylu for letting me digging through the company data.

I would like to express my appreciation to my colleagues Murat Öntaç in Eurasia Madencilik and Murat Çetintaş in Chesser Arama, for helping through the field survey.

Also I would like to thank to Dr. David W. Coulter for helping me dealing with the scripting.

I would like to express my sincere thanks to my family for their inestimable tolerance and support.

TABLE OF CONTENTS

CHAPTERS

LIST OF TABLES

TABLES

LIST OF FIGURES

FIGURES

LIST OF ABBREVIATIONS

AA	Advanced Argillic
AAHS	Advanced Argillic High Sulfide
ACORN	Atmospheric Correction Now
ASTER	Advanced Spaceborne Thermal Emission and Reflection Radiometer
ATCOR	Atmospheric Correction
BE	Binary Encoding
BIL	Band Interleaved by Length
CEM	Constrained Energy Minimization
CS	Cataclastic Silica
CTIC	Cross Track Illumination Correction
D	Diorite
DEM	Digital Elevation Model
DN	Digital Number
DP	Diorite Porphyry
ED	Euclidean Distance Measure
EMR	Electromagnetic Radiation
EPGS	EO-1 Product Generation System
ET	Evliya Tepe
FF	Flat Field
FIR	Far Infrared
FLAASH	Fast Line of Sight Atmospheric Analysis of Spectral Hypercubes
FOV	Field of View
FWHM	Full Width at Half Maximum
GCP	Ground Control Point
GDP	Granodiorite Porphyry
HDF	Hierarchical Data Format
HSE	High Sulfidation Epithermal
IAR	Internal Average Reflectance
IFOV	Instantaneous Field of View
IGFOV	Instantaneous Ground Field of View
LSU	Linear Spectral Unmixing
MF	Matched Filtering
MG	Monzo Gabbro
MIR	Mid Infrared

MNF	Minimum Noise Fraction
MTMF	Mixture Tuned Matched Filtering
NASA	National Aeronautics and Space Administration
NDVI	Normalized Difference Vegetation Index
NIR	Near Infrared
PPI	Pixel Purity Index
QBX	Undifferentiated Quartz Breccia
QD	Quartz Diorite
QM	Quartz Monzonite
QMD	Quartz Monzodiorite
RGB	Red Green Blue
RMS	Root Mean Square
ROI	Region of Interest
SAM	Spectral Angle Measure
SCM	Spectral Correlation Mapper
SFF	Spectral Feature Fitting
SID	Spectral Information Divergence
SMACC	Sequential Maximum Angle Convex Cone
SNR	Signal to Noise Ratio
SWIR	ShortWave InfraRed
TM	Thematic Mapper
TRW	Thompson Ramo Woolridge
TSA	The Spectral Assistant
USGS	United States Geological Survey
UTM	Universal Transverse Mercator
UV	Ultraviolet
VMS	Volcanogenic Massive Sulphide
VNIR	Visible Near InfraRed
VS	Vuggy Silica

CHAPTER 1

INTRODUCTION

1.1 Purpose and Scope

Recent advances in remote sensing and geographic information gathering has led the way for the development of hyperspectral sensors. Hyperspectral remote sensing, also known as imaging spectroscopy, is a relatively new technology that is currently being investigated by researchers and scientists with regard to the detection and identification of minerals, terrestrial vegetation, and man-made materials.

Imaging spectroscopy has been used in the laboratory by physicists and chemists for over a long period of time for identification of materials and their composition. In detection of individual absorption features due to specific chemical bonds in a solid, liquid, or gas; spectroscopy can be used. Recently, the Earth has become the current focus of imaging spectroscopy with advancing technology. The concept of hyperspectral remote sensing began in the mid-80s and up to now has been most widely used by geologists for the mapping of minerals. The detection of materials is dependent on the spectral coverage, spectral resolution, and signal-to-noise of the spectrometer, the abundance of the material and the strength of absorption features for that material in the wavelength region measured.

Use of remote sensing technologies in various geological applications has considerably increased in the recent years due to the fruitful results provided by the analysis. Two main reasons for this increase are: 1) new methods and interpretation techniques are suggested by researchers that tend to extract reliable information from satellite images, and 2) new satellite images with better spatial and spectral resolutions are available that provide more information to the user about the investigation area. Developments in the software technology should also be considered as a positive contribution to such studies.

The purpose of this study is to characterize the alteration through hyperspectral remote sensing methods. For this reason Hyperion image belonging to a well developed mineralization area is selected that will be introduced in the next chapter.

From the geological perspective, the area is well studied for which the mineralized area is mapped at 1:5000 scale and different types of mineralization are identified. Additionally, there is a rich database of the spectral measurements of the altered samples collected during the field survey. This database is used as a reference spectral library for the final assessment of the results.

From the remote sensing perspective, this research introduces an algorithm for the processing of Hyperion data including all necessary steps in logical order. As it is known from the literature, in most of the previous studies, the results are not satisfactory mainly due to the noisy nature of the Hyperion data. Therefore, the main contribution of this study is expected to introduce a comprehensive application that aims to increase the accuracy of the results.

1.2 Study area

The study area is located in Sivas province, north-central Turkey. Sisorta, prospect site is approximately at 120 km northeast of Sivas. The transportation network is well developed, with maintained roads allowing two wheel drive vehicles to access the project area from May until November. Access is limited at the higher elevations during the winter months due to snow cover. Locally, the property is 45 kilometers from the town of Koyulhisar (population 5,500). From Koyulhisar, access is on two lane, all weather paved highway D100 for 18 kilometers to the turnoff for the Sisorta village road, and then east 27 kilometers on paved road to Ortakent village. From Ortakent to the nearby Güzelyurt village (population 293), access is on a well maintained dirt road for 18 km, and from Güzelyurt to the property is another three kilometers along maintained forest and drill roads (Figure 1.1). The highest point in the study area is Evliya

Tepe with its 2203 m of elevation and is located at the center of the prospect (38°2’8”Easting, 40°27’3”Northing). Study area covers a 5 km by 5 km area. Topographical contours show an elliptical morphology with a 6 km of long axis and 4 km of short axis (Figure 1.2). As a result of this circular / elliptical dome-like morphology, radial drainage pattern is developed with seasonal streams. Melet Stream is the main stream flowing from east to west lining the southern border of study area. Prospect site is covered with dense green vegetation mainly as pine trees (Figure 1.3).

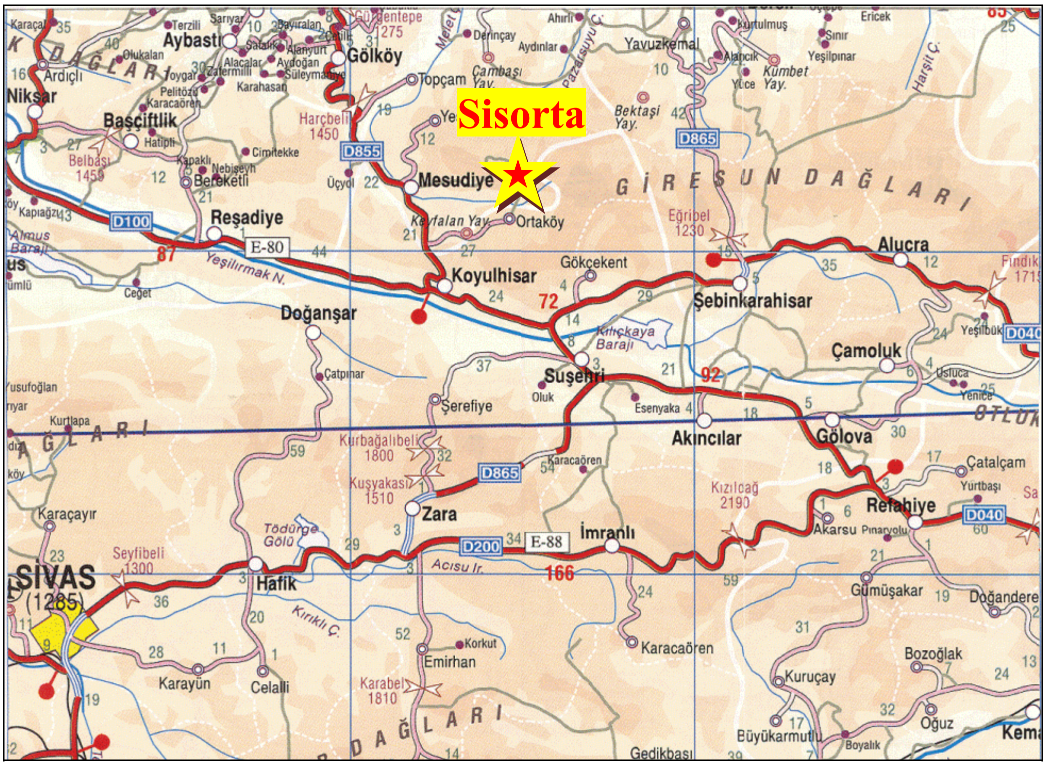

Figure 1.1 Location map of the study area.

1.3 Method of Study

The study integrates the digital image processing methods with the conventional field work. Geological mapping and spectrometer sampling carried out during the field study, formed the basis for decision making rules through several steps of image processing.

With the addition to routines data analysis carried out in ENVI 4.5, for mapping the results ArcGIS 9.2 is used and for spectroscopic survey The Spectral Assistant (TSA) software is used.

1.4 Organization of thesis

The thesis includes six chapters that are organized to reflect the corresponding subjects in a clear and well defined fashion. A brief description of each chapter is as follows:

Chapter 1 is the introduction to thesis and includes information about what will be included in the proceeding chapters.

Chapter 2 is the geology chapter. Regional and local geological setting is described combined with alteration, structure and mineralization.

Chapter 3 gives the background information about the technical details about what is meant by ‘alteration mapping by remote sensing techniques’. This chapter is divided into two parts, one of which summarizes the literally known methods in alteration mapping and the other introduces the proposed mineral mapping technique.

Chapter 4 introduces data and provides the analysis results of the techniques that are applied. Alteration maps produced by different methods are compared with themselves and in the accuracy assessment with ground survey data.

Chapter 5 states the reliability of the outcome of this study. The analysis results are discussed in every aspect.

Chapter 6 includes the conclusions and recommendations for further studies.

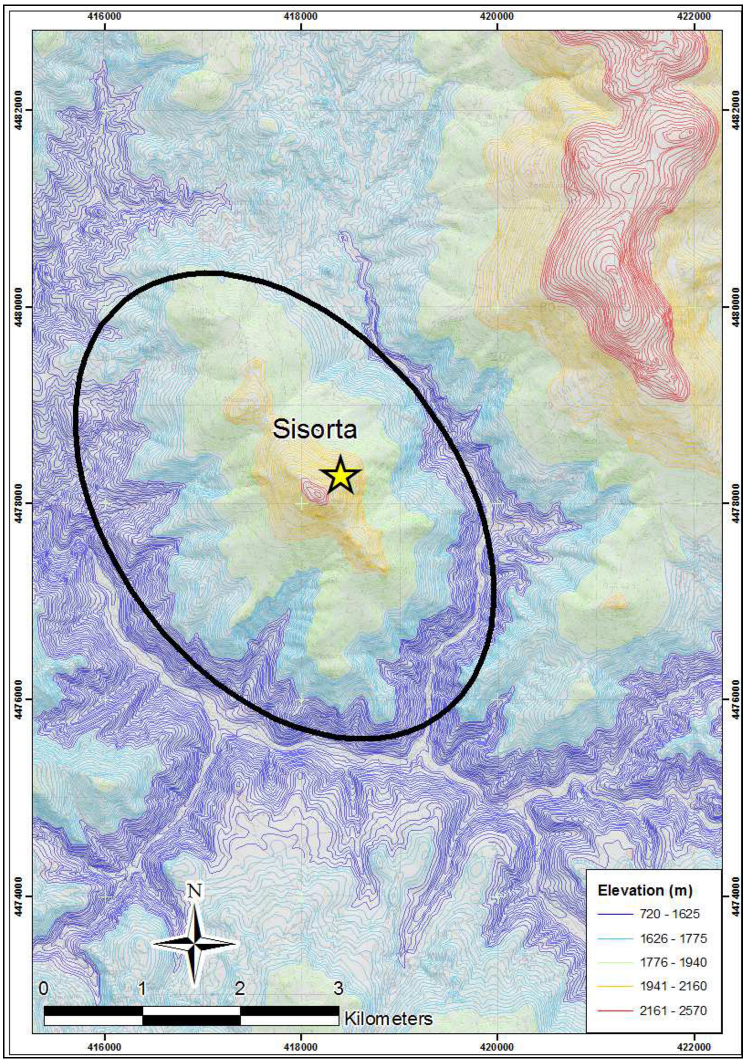

Figure 1.2 Topographical contours with 10 m intervals showing the circular / elliptical morphology of the study area.

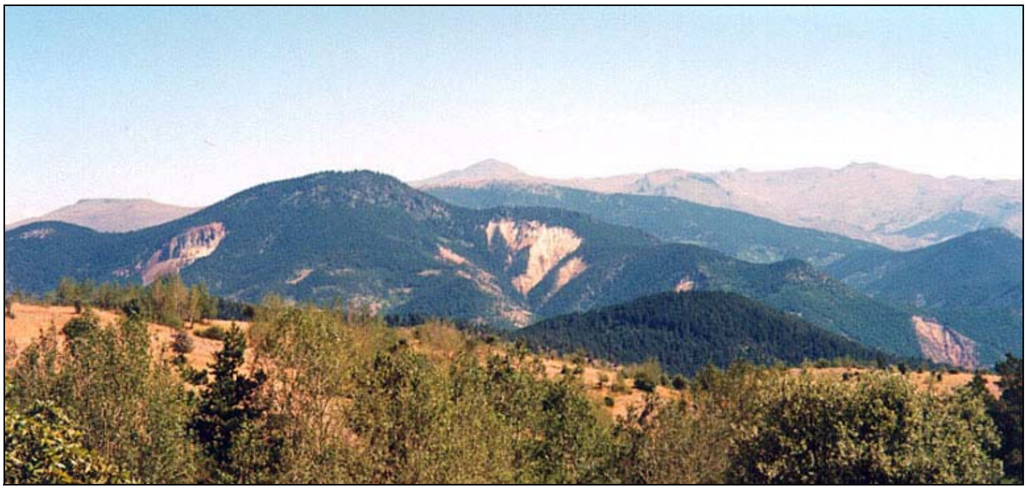

Figure 1.3 A general view of study area (looking north).

CHAPTER 2

GEOLOGY

Turkey consists of several tectonic units which are combined during the Tertiary to give the current shape of the landmass. These are from south to north Border Folds, Taurides, Anatolides and Pontides (Ketin, 1966) (Figure 2.1). Geographically, Pontides extends from Bulgaria to Caucasus with approximately 1500 km length and 100 km width. Geologically it comprises larger entities including the margins of Black Sea in the north and Ankara-Erzincan suture in the south. The study area (Sisorta prospect) is located in the eastern portion of Pontides.

The Eastern Pontides represent a complex convergent plate margin and island arc assemblage formed during the Early Jurassic through Miocene evolution of the Paleo-Tethys (Akıncı, 1980, 1984; Şengör et al., 1980; Schneider and Özgür, 1988; Tokel, 1977; Adamia et al., 1981; Khain, 1984; Soylu, 1999). The assemblage is represented by 350 km long belt of east-west trending tectonic zone; a magmatic belt, a fore-arc basin fill, a belt of metamorphic massif, an ophiolitic suture zone and a remnant basin fill which are of Jurassic to Miocene ages (Akın, 1979; Akıncı, 1980).

During Mesozoic, Eastern Pontides had an uncollisional tectonic regime where the maximum compressional stresses were created by consumption zones. Such horizontal compressional stresses are transmitted from the front margin to the inner parts of plates with a decreasing intensity due to the non rigid nature of the plates. As a result, maximum compressional stresses are formed in front margins and extensional stresses in backarc regions. Strike slip fault zones with normal and reverse control are formed during this period (Bektaş, 1984).

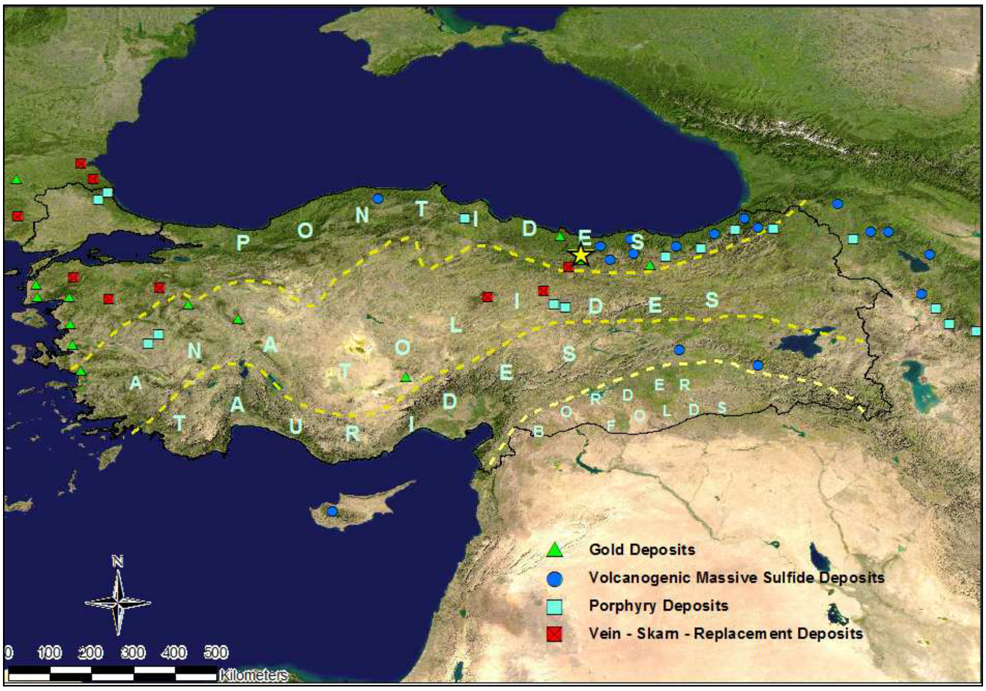

Figure 2.1 Major tectonic units and mineral occurrences of Turkey (Ketin, 1966).

This belt contains a number of important VMS deposits and epithermal Au-Ag deposits. The belt is interpreted to be the relic of a complex volcanic arc system (Akın, 1979; Akıncı, 1980).

2.1 Prospect Geology

Three main units exposed in the area are Upper Cretaceous volcanic rocks, Upper Cretaceous intrusive rocks and Quaternary deposits. A generalized columnar section of the study area is shown in Figure 2.2. The basement rocks of the study area are composed of Upper Cretaceous (Lower Maastrichtian) andesitic agglomerates which are conformably overlain by Upper Cretaceous (Upper Maastrichtian) andesitic unit. These volcanic units are in cross cutting relation with Upper Cretaceous (Upper Maastrichtian) intrusive rocks of mainly granodiorite, monzonite and diorite. Volcanic and intrusive units are unconformably overlain by Quaternary alluvium and soil cover (Bedi, 1998).

Geological map of study area is provided from General Directorate of Mineral Research and Exploration of Turkey (Çakır and Kesgin, 1999) at 1:25.000 scale (Figure 2.3). This map also shows the alteration types in the study area.

However, being the main focus of this study, alteration is given in detail with a separate map in the next section. Therefore the geological map will be explained in relation to lithology and structure.

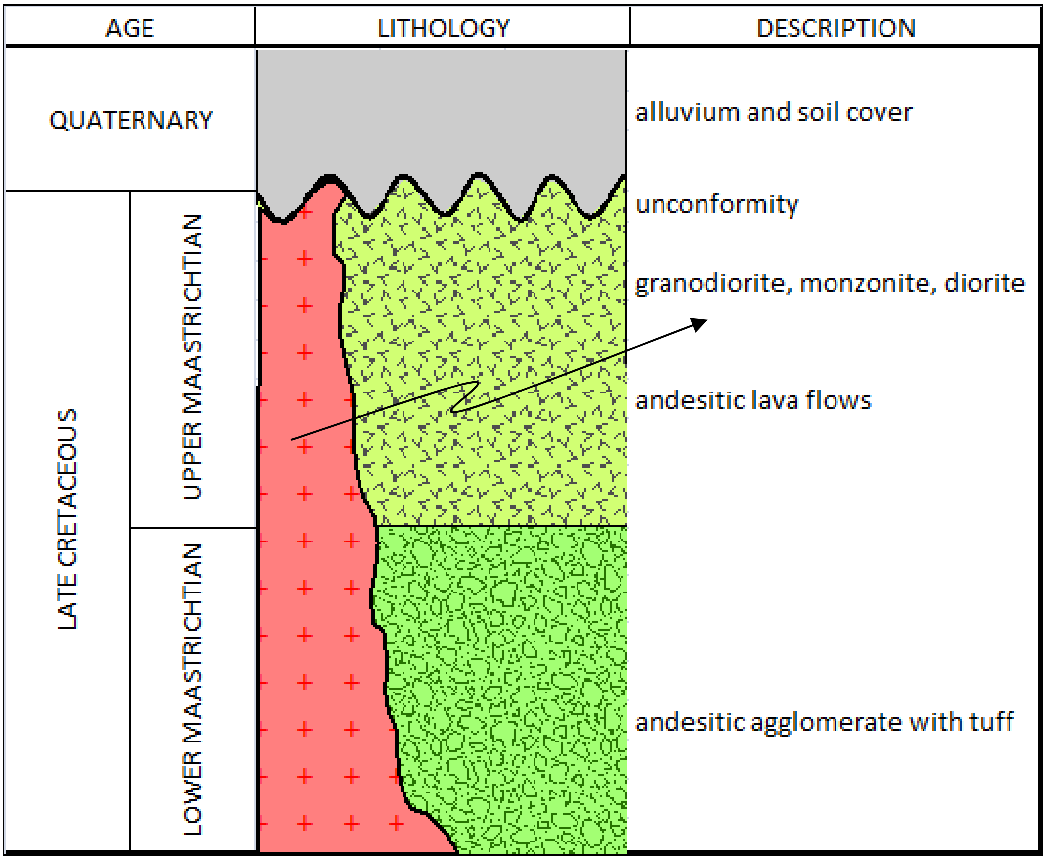

Figure 2.2 Generalized columnar section of the study area (modified from Çakır and Kesgin, 1999).

2.1.1 Late Cretaceous Volcanics

Two units can be separated as, a Lower Maastrichtian basal unit of andesitic agglomerates and an overlying unit of Upper Maastrichtian andesitic flows and tuffs (Çakır and Kesgin, 1999).

i. Andesitic Agglomerates

Andesitic agglomerates are the most wide spread unit extensively exposed in the northern and western portions of the study area. The base of this unit is not observed within the study area. It is conformably overlain by andesitic lava flows.

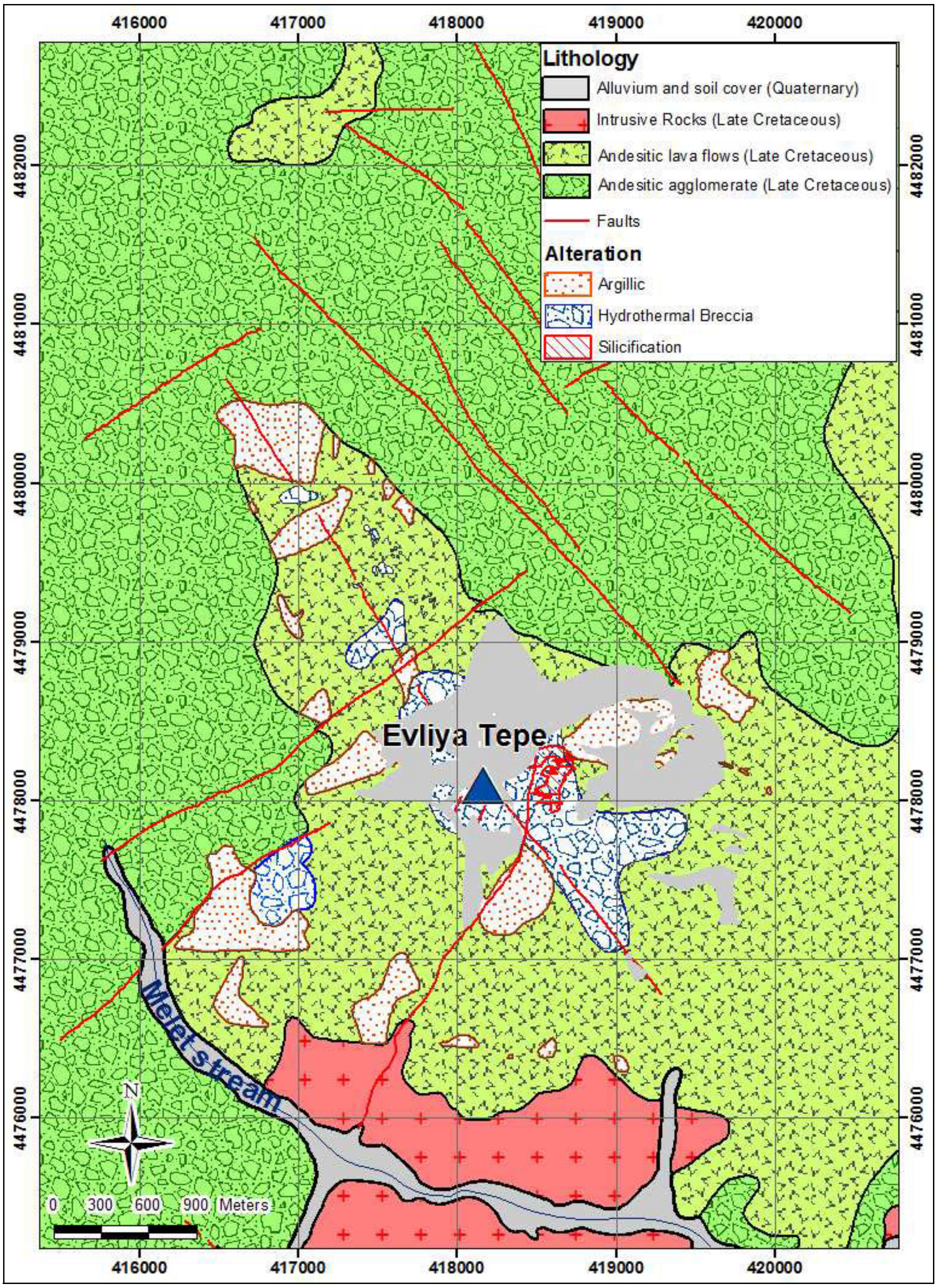

Figure 2.3 Local geology of the study area (Çakır and Kesgin, 1999).

Good flow foliation is locally observable, but agglomeratic textures dominate with fine to coarse cognate clasts in finer andesitic matrix. Andesites are typically fine grained porphyryitic. Crystal composition is primarily andesine to labradorite with some orthoclase and the clino-pryoxene augite. Olivine and opaques are also present in small amounts, the principal opaque being magnetite. Plagioclase, pyroxene and olivine phenocrysts are set in a microlitic matrix of plagioclase and vitrified material.

In general the unit is propylitically altered with byproduct epidote, chlorite, calcite, quartz and pyrite. Minor argillic alteration is seen locally as bleached zones containing green and white clays and pyrite.

Minor chalcopyrite-quartz veining in propylitized agglomerates is observed at the northern slope of Evliya Tepe. Typically the andesitic agglomerates are much less altered than overlying andesitic lava flows and therefore form a rather sharp footwall to the favorable andesitic volcanics.

ii. Andesitic Lava Flows

The unit covers a large area from northwest flanks to Melet stream in the southwest, bounded by intrusives in the south and continues to the east of Evliya Tepe. Andesitic lava flows overlie conformably the agglomerates and are cross cut by intrusives.

The andesites on Evliya Tepe consist of massive lava flows with lesser lithic and well-foliated fine-grained airfall tuffs. Sparsely intercalated volcaniclastic sediments are observed in few locations.

Euhedral to subhedral plagioclase phenocrysts of andesine composition dominate the porphyritic andesites. Two size populations are typical, one of several mm to a cm, and a smaller population around one mm. Other phenocrysts include hornblende, augite and minor quartz. Opaque minerals are rare and include rutile and anatase. The matrix consists primarily of plagioclase microlites, iron oxide and opaques.

The andesitic lava flows are thought to be as the primary host of ore in the Sisorta high-sulfidation epithermal (HSE) Au-Cu deposit. Andesitic lava flows are also the most suitable host to the mesothermal alteration assemblages present. Strong alteration zones are identified within this unit. The alteration products observed in this unit are silica, clay minerals, pyrite and hematite (Çakır and Kesgin, 1999).

2.1.2 Late Cretaceous Intrusive Rocks

Intrusive rocks are largely distributed along Melet stream in the south of Evliya Tepe on the study area.

The clear crosscutting relationship of intrusive rocks with the andesitic lava flows and andesitic agglomerate indicates its possible age as younger than Late Cretaceous (Late Maastrichtian) (Çakır and Kesgin, 1999). Also it is thought to be older than the overlying Eocene (Lutetian) volcanics in the region (Bedi, 1998).

Intrusive rocks in the project area denote a stock-like body with a composition ranging from quartz-monzonitic to monzo-gabbroic in composition, and include quartz-monzonite (QM), granodiorite porphyry (GDP), quartz monzo-diorite (QMD), quartz-diorite (QD), diorite (D), diorite porphyry (DP) and monzo-gabbro (MG).

The intrusive rocks are characterized by holocrystalline groundmass. Quartz is present in all phases of the intrusives, ranging from abundant in QM to minor in the MG. Orthoclase and sodic plagioclase are common in the QM and GDP, while calcic plagioclase from oligoclase to labradorite composition is the predominant feldspar in other phases. Muscovite and biotite are the predominant micas in QM. Amphibole and biotite predominate in all other phases, and pyroxene occurs in the MG. Minor opaques are seen in all rocks, and rutile was noted in the D.

Propylitic-style alteration is observed locally in most phases, including chlorite, epidote, calcite and quartz. Clay and white-mica alteration was observed in minor amount having kaolinite, sericite, quartz and pyrite products. In general alteration is better developed in host volcanics and shades out considerably in intrusive (Chadwick, 2005).

2.1.3 Quaternary deposits

Quaternary deposits are observed along the Melet stream and its branches located in the southern part of the study area. Also a thick soil cover is formed in the area caused by landslides and differentiation due to the high relief and intense weathering around Evliya Tepe.

With the high relief, landslides are observed within soil cover. Landslides are composed of very coarse angular blocks, including resistant rocks; some are large enough for an outcrop size, in debris flow matrix. Found as largely preserved on the north slopes of Evliya Tepe in long tongue-like sheets derived mainly from the higher altitudes. They weather and disintegrate to form talus and soil on south slopes of Evliya Tepe.

Ferricrete is another compound in the Quaternary soil cover. It is characterized by FeOx cemented (hematite, and clay) gravel size deposits. Locations near fault and/or landslide scarps are suitable for ferricrete formation with a high ground water circulation and presence of underlying absorbent argillic rocks. Leached Fe from overlying Quaternary deposits and mineralized bedrock cements the fragments where circulation is enhanced by the impermeable sub unit (Chadwick, 2005).

Quaternary deposits are found with angular unconformity over the underlying volcanic and intrusive units (Çakır and Kesgin, 1999).

2.2 Structures

Main structural elements observed in the area are faults. The alteration and mineralization styles at Sisorta are primarily related to northeast and northwest trending structures. These primary zones are developed in accordance with the activity of North Anatolian Fault Zone and influenced the younger units. The two main structural trends are northeast and northwest trending structures (Bedi, 1998).

2.2.1 Northeast Trending Structures

Evliya Tepe is traversed by several northeast trending structures. There are four main northeast faults found to be exposed immediately north, south and east of the peak. The northernmost fault is discarded as it is not related within the image area.

From south to north the trends are 028° N, 051° N and 056° N respectively with 2.6 km, 2.1 km and 3.2 km lengths.

For the southernmost fault, the southeastern block is down thrown dipping to the southeast and northwest. The fault on the east of Evliya Tepe the north western block is down thrown. For the north fault zone, the northwestern block is down thrown.

2.2.2 Northwest Trending Structures

Northwest trending structures that control the morphology of Evliya Tepe are oriented at a general trend of 325° N. Although a major 5 km fault crossing the highest point of study area is identified, the majority of faults of this trend are mapped on the northwest of Evliya Tepe. All the exposures of silica cap align along this trend.

Left lateral movement is observed within numerous strike slip faults in the northwest structural trend (Çakır and Kesgin, 1999).

2.3 Alteration Groups

Detailed alteration information is given in this section according mostly to the field observations and spectral survey (Chadwick, 2005).

Topographic highs over Evliya Tepe are characterized by competent and very resistant, quartz rich silica cap which is related with epithermal gold system and mesothermal phyllic alteration. High sulfide (chiefly pyrite) content of the mineralized rocks locally produces acidic waters and subsequent leaching near surface. Epithermal and mesothermal related argillically altered portions of the mineralized regions of the system, especially where leached, forms topographic lows, due to the low strength and high tendency to weather easily. Weathering and mass wasting of the argillic rocks with the help of faulting leads to relatively rapid and often catastrophic erosion of the system.

The effects of northeast structures are best exposed in incompetent argillic andesite as a number of landslide scarps and related ferricrete deposits. Importantly, these structures are controlling the majority of phyllic alteration in the area. Phyllic alteration clearly observed at northwest and southeast of Evliya Tepe, and to the northeast and southwest along the structures themselves.

The most extensive silica cap at Sisorta is clearly related to northwest and northeast trending structures at northwest and southeast of Evliya Tepe. The intersection of northeast and northwest therefore introduces a favorable structural setting for the epithermal system related silica bound mineralization (Chadwick, 2005).

Epithermal alteration and mineralization is displayed within the northwest structural trend, which is approximately a kilometer wide 5km along strike. Juxtaposed phyllic alteration against characteristic epithermal alteration zones such as AAHS and VS are found to be exposed along the flanks of the trend. This juxtaposition points out the structural northeast and southwest boundaries of the epithermal system. Although northwest structures are much related with epithermal effects, they do control some porphyry-style propylitic alteration as observed on the southeast end of Evliya Tepe, 2 km southeast of the peak.

Especially around fault-related landslide scarps at the base of the Quaternary, ferricrete occurs. Fe rich ground water has deposited FeOx and cemented the basal deposits. These usually overlie the argillic rocks.

2.3.1 Epithermal Group

With the mineralization and alteration styles Sisorta shows a typical well-preserved High Sulfidation Epithermal (HSE) Au-Cu system. Most of the alteration mineralogy characterized by HSE’s is documented by past studies (Chadwick, 2005).

The alteration types are very distinct and observable throughout the project area (Figure 2.4). With the aid of the field spectroscopy (PIMA) work, classified units are mapped accordingly which are in order of alteration intensity, as follows:

i. Advanced Argillic (AA)

Advanced argillic alteration is observed by intense clay-white mica alteration of host. Typically low level of very fine-grained pyrite is found as dissemination and replacement. Quartz may be found as veinlets and replacement. Barite, alunite and jarosite are common as accessory.

Study of field spectroscopy (PIMA) also confirmed the presence of alunite, dickite, kaolinite, pyrophyllite and diaspore in areas of AA alteration.

ii. Advanced Argillic, High Sulfide (AAHS)

The sulfide amount introduced to the system is the reason of the separation of AAHS and the leached equivalent, AAHS/L from AA. Both groups have similar texture and mineralogy, but AAHS contains more than 10% fine grained pyrite, and locally may reach massive sulfide status with over 50% pyrite content. Enargite and chalcopyrite are found as accessory minerals. Galena and sphalerite are also traced.

AAHS group is identified by spectroscopy with a higher temperature, lower pH suite of potassic minerals than AA, including alunite, dickite, pyrophyllite and diaspore.

Intimate association of AAHS with AA and Vuggy Silica (VS/VSBX) is the result of its transitional origin between the base of Au deposition (AA) and the top (VS).

iii. Silicification

Several map units come under the general heading of silicification, which forms the top of Evliya Tepe as well as the effective silica cap to the HSE system. Silicification in the forms of vuggy silica, cataclastic silica and undifferentiated quartz breccias overlie AAHS and AA.

Vuggy Silica is characterized by greater than 90% quartz-replaced andesite with psuedomorphic vugs where plagioclase phenocrysts have dissolved. VS, typical of many HSE’s is abundant on Evliya Tepe. Over the advanced argillic alteration facies AA and AAHS, it forms a moderately-dipping cap.

Cataclastic Silica also has greater than 90% quartz and consists of angular quartz clasts of varying size cemented by a thin cataclastic matrix. CS is found in several parts of the silica cap in a pipe-like appearance, more restrictedly than VS. The observation of potassic minerals led to very high T and very low pH for the epithermal environment showed a possibility of a hydrothermal feeder.

Undifferentiated Quartz Breccia (QBX) outcrops in several areas and includes quartz breccias not belonging to definitions of VS or CS. Typically they occur accordingly within fault zones and/or fault intersections.

2.3.2 Mesothermal Group

The Sisorta Au-Cu HSE deposit occurs along a northwest structural trend and is telescoped within an extensive mesothermal, porphyry-style alteration zoning. The primary mesothermal alteration types are described below in order of increasing intensity.

i. Propylitic

The propylitic alteration is found largely as peripheral and at lower elevations of the system. Commonly the mineralization has developed in structurally-controlled breccia, stockwork and vein systems mainly in propylitically altered volcanics. The primary northwest trend controlling the Sisorta HSE is also observed with a similar azimuth commonly in many of these prospects.

Propylitic assemblage is found usually disseminated and associated with thin stockworks. Sometimes these stockworks are weakly silicificed and other than quartz, green clay/mica, which is identified as chlorite, epidote, calcite and pyrite are deposited. Propylitic alteration is mainly found in basaltic rocks, since most of the andesites are argillicaly if not phyllically altered.

Very locally weak quartz-chalcopyrite veining is observed at the north border of Evliya Tepe in basalts. Along the southeast flank of Evliya Tepe some propylitic alteration occurs, in andesites, interfingered with argillic alteration. Additionally, on the south flank of Evliya Tepe widespread weak propylitic alteration is hosted by the intrusive stock.

The PIMA work showed that propyilitization in the system is characterized by relatively low T, and moderate pH potassic phases. Accordingly kaolinite and illite/smectite are classified in this group.

ii. Argillic

Weak to strong argillic alteration overlies the majority of Evliya Tepe occuring peripheral to the HSE. Extensive clay/white mica alteration characterizes this group which results much better whitening at surface than AA. Certain amount of pyrite is introduced in this part of the system with rarely quartz-pyrite stockworks and limonitic remnants at surface.

Kaolinite and illite/smectite in the argillic zone are identified by ASD results. Along major northeast structure, alunite, dickite, pyrophyillite and diaspore are also identified locally, representing a structurally-controlled epithermal overprint.

iii. Phyllic

A broad zone of phyllic alteration occurs peripheral to the HSE, adjacent to a major northeast structure, which traverses the Mountain just south of the Evliya Tepe summit. Smaller bodies of phyllic alteration are present on another northeaster north of the summit and along northwest trends on the south and east flanks of Evliya Tepe.

The phyllic zone is characterized by 50-90% quartz, abundant clay/white mica and 1-15% coarse, disseminated, brassy, cubic pyrite. Locally thin quartz-pyrite veinlets are common, but dense stockworking is rare.

Primarily illite, dickite and kaolinite are identified by PIMA. Higher T lower pH suite of phases is detected along the major northeast structure. With a possibility on structurally controlled epithermal overprint, phyllic alteration points out the central portions of the HSE. The epithermal overprint includes alunite, dickite, pyrophillite and diaspore.

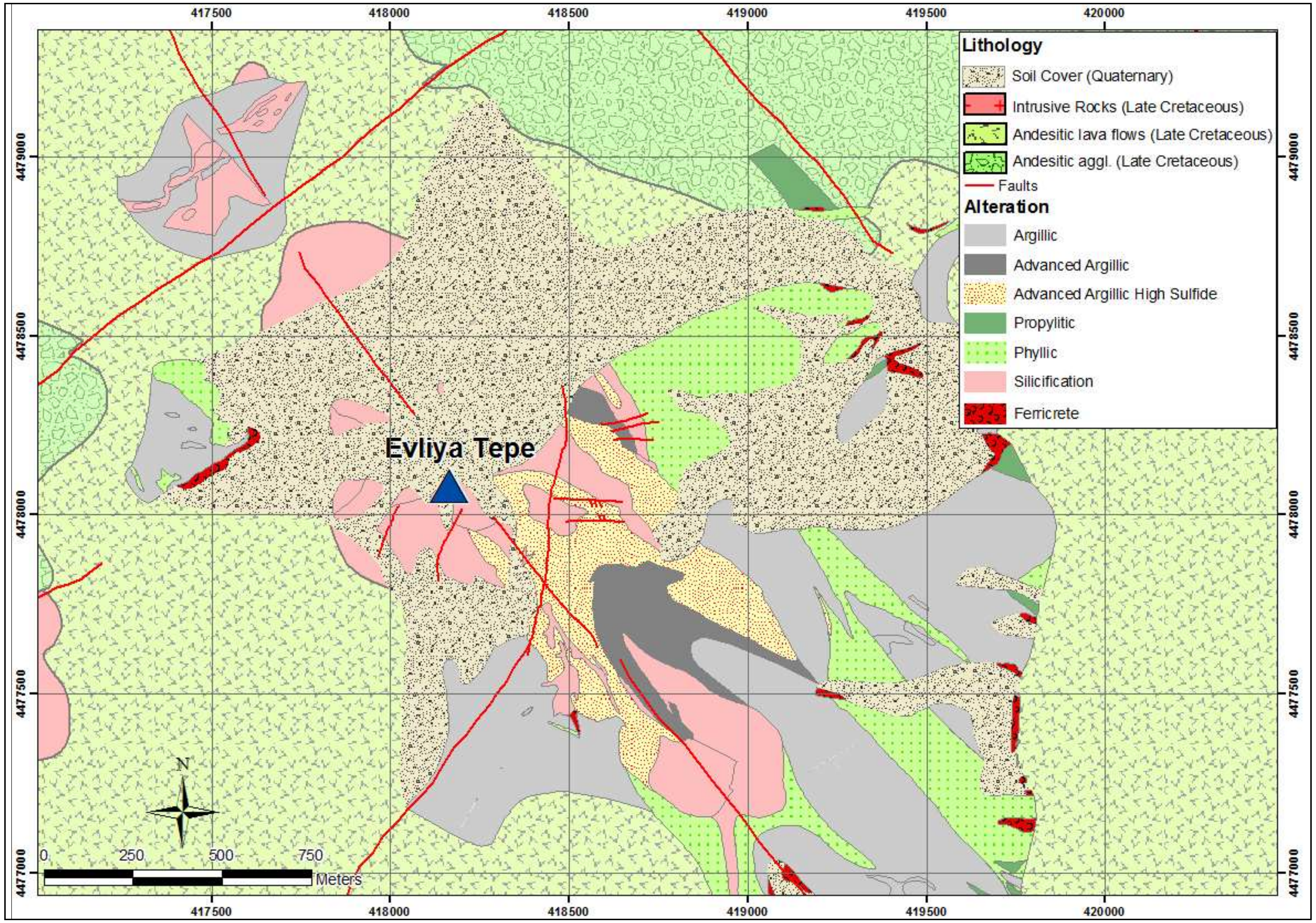

Figure 2.4 Detailed alteration map around Evliya Tepe.

2.4 Mineralization

The Sisorta epithermal and associated porphyry systems include distinctly zoned mineralization. Gold covers the top of the epithermal high-sulfidation system, located within silica cap and immediately below. Copper occurs in low concentration in these oxidized gold rich portions of the system, and increases as gold fades out near the base of the epithermal system (Vigar et al., 2009).

Copper, lead and zinc occur in very low amounts throughout the epithermal system. However, they occur in higher grades within the propylitic zone of the associated porphyry system which is distal to epithermal mineralization. Porphyry and epithermal related hypogene and supergene minerals are summarized accordingly in the order of the abundance.

Pyrite, covellite, enargite, chalcopyrite, galena and sphalerite are the main hypogene minerals. Malachite and chalcocite are deposited by the leaching of the vuggy silica and advanced argillic alteration zones.

Although the productive mining history dates back to the beginning of twentieth century, exploration history of Sisorta actually started in 1970s and 1980s by General Directorate of Mineral Research and Exploration (MTA). In 2004, private exploration company gathered the license and commenced geochemical, geophysical and drilling activities. The results are published in a technical report in detail and a reserve estimation is performed for gold by using a total of 72 diamond drill hole data with a combined length of more than ten kilometers.

The report states an indicated total reserve of 3.170.000 tones with a grade of 0.89 g/t Au (with 0.4 cutoff). An inferred total is reported as 11.380.000 tones of 0.58 g/t Au again by using 0.4 g/t cutoff (Vigar et al., 2009).

CHAPTER 3

BACKGROUND ON HYPERSPECTRAL PROCESSING

3.1 Hyperspectral Remote Sensing

Up to the 1990's remote spectroscopic measurements of Earth and planets have been dominated by multispectral imaging experiments that collect high quality images in a few usually broad-spectral bands. However, a new generation of sensors is now available that combines imaging with spectroscopy to create the new discipline of imaging spectroscopy. Imaging spectrometers acquire data with enough spectral range, resolution and sampling at every pixel in a raster image so that individual absorption features can be identified and spatially mapped (Goetz et al., 1985). Imaging spectroscopy has many names in the remote sensing community, including imaging spectrometry, hyperspectral, and ultraspectral imaging.

Some traditional approaches to remote sensing analysis born in the era of multispectral imaging are based on statistical methods exploiting the large number of samples (pixels) in the remotely sensed data. The proven power of these traditional approaches is vastly multiplied by the rapid increase in information content inherent when the number of spectral bands increases from order 10 to order 100.

Many narrow wavelength samples of reflected electromagnetic radiation (EMR) from the Earth’s surface are sensed by hyperspectral imaging systems. This sampling capability is measured by the spectral resolution in which systems with a spectral resolution of 20 nm or finer per band are generally considered hyperspectral. These imaging systems have optical characteristics like their field of view (FOV). The area that is sensed through the instantaneous field of view (IFOV) is the spatial size of each individual sample and is called the instantaneous ground field of view (IGFOV). The relationship between the pixel size (IGFOV), the IFOV, and the platform altitude is: IGFOV (in meters) = IFOV (in radians) * Altitude (in meters). Thus, each pixel in the image data over an area of the surface is represented by the average spectra measurement. The systems that are used for alteration identification cover approximately the visible blue (400 nm) to shortwave infrared (2500 nm) range of EMR (Clark, 1999).

Despite of this increase in information, the obtained results are by their nature scene-dependent, cannot be applied globally, and the statistical approaches do not exploit the information inherent in each individual spectrum concerning the chemical and nature of the remotely sensed surface. Some analysis tools like signal processing, has had good success at detection of specific spectral signatures but this approach requires that the signature be stable from lab to field. Most geologic, and many biologic materials do not meet this criterion.

3.1.1 Spectroscopy

Capability of a spectrometer is described by 4 general parameters: 1) spectral range, 2) spectral bandwidth, 3) spectral sampling, and 4) signal-to-noise ratio (S/N).

Spectral range is important to cover enough diagnostic spectral absorption to solve a desired problem. There are general spectral ranges that are in common use, each to first order controlled by detector technology: a) ultraviolet (UV): 0.001 to 0.4 µm, b) visible: 0.4 to 0.7 µm, c) near-infrared (NIR): 0.7 to 3.0 µm, d) the mid-infrared (MIR): 3.0 to 30 µm, and d) the far infrared (FIR): 30 µm to 1 mm. The ~0.4 to 1.0-µm wavelength range is sometimes referred to in the remote sensing literature as the VNIR (visible-near-infrared) and the 1.0 to 2.5-µm range is sometimes referred to as the SWIR (short-wave infrared) (Figure 3.1).

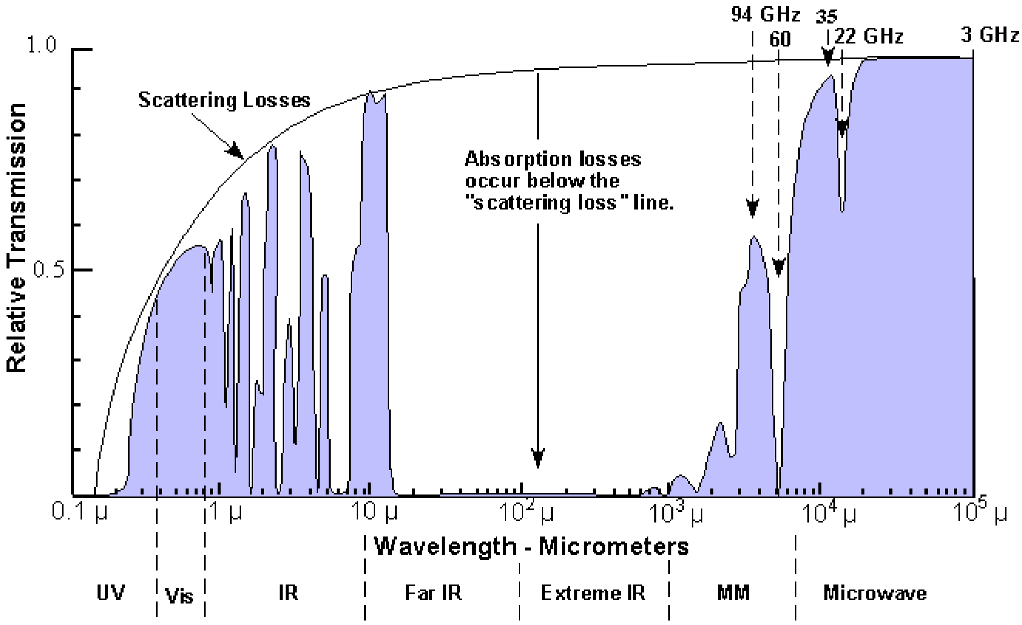

Figure 3.1 Atmospheric absorption of electromagnetic radiation (Clark, 1999).

Spectral bandwidth is the width of an individual spectral channel in the spectrometer. The narrower the spectral bandwidth, the narrower the absorption feature the spectrometer will accurately measure, if enough adjacent spectral samples are obtained.

Spectral sampling is the distance in wavelength between the spectral bandpass profiles for each channel in the spectrometer as a function of wavelength.

A spectrometer must measure the spectrum with enough precision to record details in the spectrum. The signal-to-noise ratio (S/N) required to solve a particular problem will depend on the strength of the spectral features under study. The S/N is dependent on the detector sensitivity, the spectral bandwidth, and intensity of the light reflected or emitted from the surface being measured. A few spectral features are quite strong and a signal to noise of only about 10 will be adequate to identify them, while others are weak, and a S/N of several hundred (and higher) are often needed (Clark, 1999).

Spectroscopy is the study of electromagnetic radiation. Spectrometry is derived from spectro-photometry, a term used for years in astronomy which is the measure of photons as a function of wavelength. However, spectrometry is becoming a term used to indicate the measurement of non-light quantities, such as in mass spectrometry. Hyper means excessive, but no imaging spectrometer in use can be considered hyper-spectral, after all, a couple of hundred channels pales in comparison to truly high resolution spectrometer with millions of channels. Ultraspectral is beyond hyperspectral, a futuristic term which is not currently available. Terms like laboratory spectrometer, spectroscopist, reflectance spectroscopy, thermal emission spectroscopy, etc, are in common use.

Mainly electrical and vibrational processes are the cause for absorption bands in the spectra of materials. Electronic processes important in absorption phenomena are crystal field effects, charge transfer absorptions, conduction bands and color centers. For the clay and iron minerals that dominate alteration products, crystal field effects and charge transfer are the primary mechanisms of electron transitions.

Electromagnetic radiation may cause a bond vibration to switch from a lower to higher vibrational energy state and thus absorb energy (Hunt, 1982). The primary absorption bands resulting from this are centered at thermal wavelengths but have overtones in the shortwave infrared (SWIR). For alteration minerals in the systems used today, Al-OH and Mg-OH bonds are the most important and produce absorption bands near 2200 nm and 2300 nm.

3.1.2 Alteration Identification

Hydrothermal alteration is defined as the reflection of response of pre-existing, rock-forming minerals to physical and chemical conditions different than those, under which they originally formed, especially by the action of hydrothermal fluids (Beane, 1982).

The nature of the alteration products depends on 1) the character of the wall rock, 2) the character of the invading fluid, which defines such factors as Eh, pH, vapor pressure of various volatile species, anion-cation composition, and degree of hydrolysis, and 3) the temperatures and pressures at which the reactions take place (Guilbert and Park, 1986).

Alteration may result from 1) diagenesis in sediments, 2) regional processes, such as metamorphism, 3) postmagmatic or post-volcanic processes associated with cooling, and 4) direct mineralization processes.

Reactions that are important to alteration are of many times: 1) hydrolysis, 2) hydration-dehydration, 3) alkali or alkali-earth metasomatism, 4) decarbonation, 5) silication, 6) silicification, 7) oxidation-reduction and finally, a number of addition-removal interactions such as carbonatization, desulfidation, sulfidation, and fluoridation.

3.1.2.1 Alteration Types

The principle alteration assemblages and associates found in aluminosilicate rocks are explained below (Yetkin, 2003).

Potassic or biotite-orthoclase alteration, also known as K-silicate, involves the presence of introduced or recrystallized K-feldspar in a rock with or without biotite and sericite, commonly with traces of any of the characterizing calcium salt accessory minerals anhydrite, apatite, fluorite, calcite and scheelite also chalcopyrite, molybdenite, pyrite, magnetite or hematite.

Phyllic or sericitic alteration is characterized by the dominance of the phyllosilicate sericite, a name reserved for fine-grained white mica (muscovite) which results from alteration and metamorphism. All primary rock-forming silicates such as feldspars, micas and mafic minerals are converted to sericite plus quartz.

Propylitic alteration involves the alteration-generation of epidote, chlorite, and carbonates typically replacing plagioclase (epidote, chlorite, calcite) and hornblende-biotite (chlorite, epidote, montmorillonite).

Argillic assemblages are formed by the dominance of kaolinite after plagioclase, montmorillonite after the amphiboles and plagioclase. K-feldspar is metastable and not affected, but alkali and alkali-earth leaching and removal are substantial, except for potassium.

Advanced argillic represents low K+ / H+ and Na+ / H+ through both low activities of the alkalies and strongly acid, high H+ fluids. Strong leaching of all alkalies occurs. At higher temperatures above about 300 °C, pyrophyllite or pyrophyllite-andalusite occurs; at lower temperatures, kaolinite and dickite prevail. Quartz is abundant, and alunite, topaz, tourmaline and other hydro-chloro-fluoro-boro-aluminosilicates also occur.

The alteration types that are important for this study and the representing minerals are shown in Table 3.1.

Table 3.1 Alteration types and representing minerals

Alteration Types	Representing Minerals
Potassic	Orthoclase
Propylitic	Epidote, Chlorite
Argillic	Kaolinite, Illite, Montmorillonite
Advanced Argillic	Pyrophyllite, Alunite
Oxidation (Fe)	Hematite, Goethite, Jarosite
Silicification	Quartz

3.1.3 Spectral Fingerprint

The supergene iron minerals are identified by their characteristic visible to near infrared (VNIR) spectra (Figure 3.2). Electron transition absorptions around 900 nm vary subtly in wavelength and intensity based on the crystal structure and bonds around the Fe cations. These absorptions are displayed as broad, relatively weak features.

The hydrothermal alteration minerals are identified by characteristic absorption features in the SWIR (Figure 3.2). Molecular vibrations cause these features and are manifested as narrow, relatively strong, absorptions. Due to the change in the Al content Illite has absorption minimum around 2210 nm (Clark, 1999).

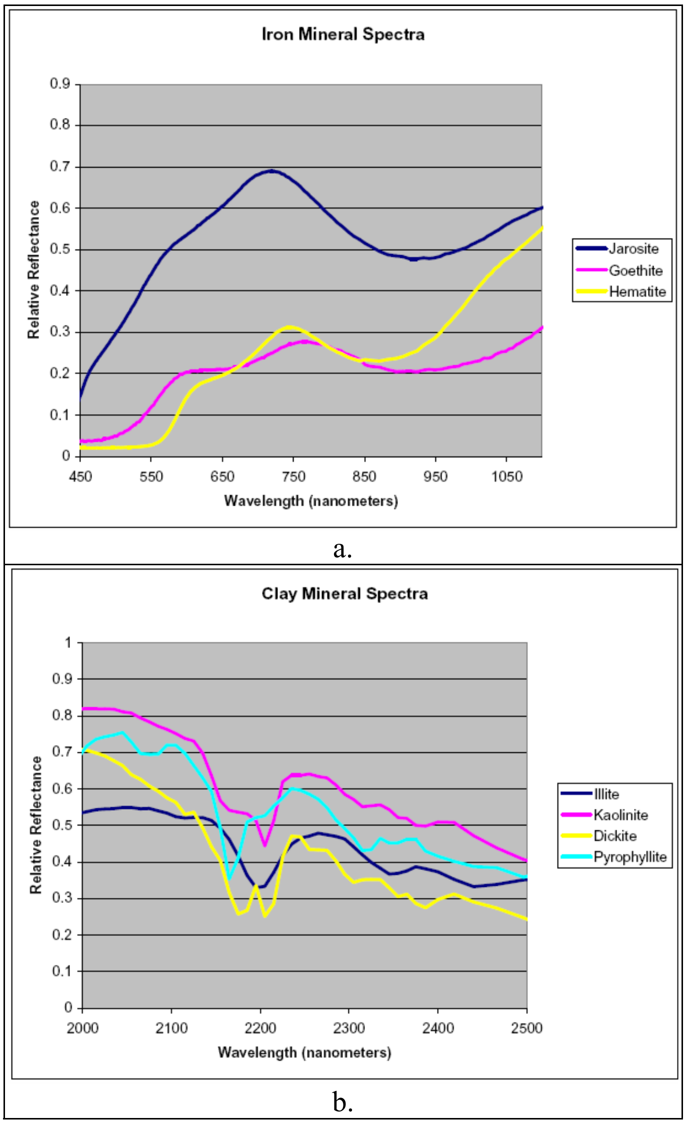

a.

b.

Figure 3.2 Characteristic spectra for selected a. iron and b. clay minerals (Coulter, 2006).

3.2 Techniques of Hyperspectral Remote Sensing

Field and laboratory spectra have been used to relate absorption features to the chemical composition of samples in soil science and mineralogy. For the analysis of hyperspectral image data and information extraction like surface mineralogy there are several techniques developed (van der Meer, 2004).

Throughout the numerous techniques a road map can be created with the generalized methods (Figure 3.3). After a successful data gathering step, calibration comes. Numerous data providers today correct the sensed imagery for sensor related radiometric and geometric errors, but it is not possible to have data as error-free. To manage good analysis results it is obligatory to apply scene specific data correction.

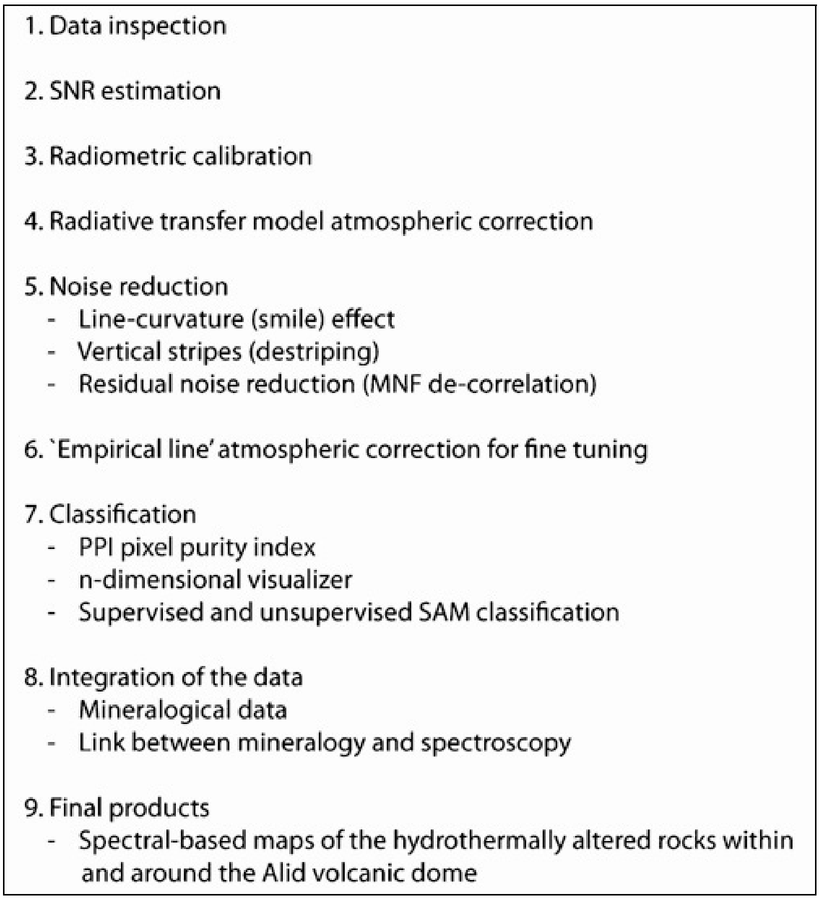

1. Data inspection

2. SNR estimation

3. Radiometric calibration

4. Radiative transfer model atmospheric correction

5. Noise reduction
   - Line-curvature (smile) effect
   - Vertical stripes (destriping)
   - Residual noise reduction (MNF de-correlation)

6. `Empirical line' atmospheric correction for fine tuning

7. Classification
   - PPI pixel purity index
   - n-dimensional visualizer
   - Supervised and unsupervised SAM classification

8. Integration of the data
   - Mineralogical data
   - Link between mineralogy and spectroscopy

9. Final products
   - Spectral-based maps of the hydrothermally altered rocks within and around the Alid volcanic dome

Figure 3.3 Typical hyperspectral image analysis flowchart (van der Meer, 2004).

3.2.1 Data Specific Correction

As discussed previously, the hyperspectral data are provided with basic systematic corrections applied. Further corrections are needed, however, to radiometrically calibrate the data to reflectance and geometrically tie the data accurately to the ground.

3.2.1.1 Radiometric Correction

The identification and mapping of minerals with hyperspectral data require that the image data be corrected to relative reflectance so that direct comparison with field and library spectra can be undertaken. There are a number of approaches for achieving this correction. These are Internal Average Reflectance (IAR), Flatfield Correction and Fast Line-of-sight Atmospheric Analysis of Spectral Hypercubes (FLAASH).

i. Internal Average Reflectance (IAR)

IAR Reflectance calibration is used to normalize images to a scene average spectrum. This is particularly effective for reducing hyperspectral data to relative reflectance in an area where no ground measurements exist and little is known about the scene. It works best for arid areas with no vegetation. An average spectrum is calculated from the entire scene and is used as the reference spectrum, which is then divided into the spectrum at each pixel of the image (RSI, 2005).

ii. Flatfield Correction

The flatfield correction assumes that there exists and identifiable pixel or pixel group that are reflecting all the sun radiance without absorbing being spectrally flat. It is important to select a spectrally flat pixel by studying the image by means of spectral response. Ideally pure white high reflectant flat field is placed to the study area that before the time of data acquisition.

iii. Fast Line-of-sight Atmospheric Analysis of Spectral Hypercubes (FLAASH)

FLAASH is a separate model in ENVI which is designed to model the radiance it reflectance conversion and carrying out atmospheric correction. This is done by simulating the solar irradiance at the time of data collection and comparing it with the radiance at the sensor (image data).

3.2.1.2 Geometric Correction

Digital image data can often contain errors in geometry due to the motion of the scanners, sensor characteristics, the curvature of the earth, or other factors. Geometric correction uses information such as GCPs and/or camera characteristics to rectify these errors. Today most of the data providers perform sensor related geometric correction but to get high accuracy manual rectification is performed usually after the data analysis.

In order to increase the geometric accuracy in image registration the third dimension is used. The orthorectification uses geometric projections to produce geometrically correct images for mapping and measurement. The idea is to correct local and global distortions by adjusting the image for camera characteristics, platform positions and terrain details. Generally four to six Ground Control Points are required to solve exterior orientation parameters.

To orthorectify the image, camera calibration information, DEM file, GCPs referenced by their x, y, and z coordinates.

3.2.2 Data Analysis

After the correction, the inversion of the calibrated image data into mineral classes or proportions is applied. First of all the minerals of interest need to be identified through a process called endmember identification. There are two general inversion types that may be utilized: mineral classification or mineral unmixing. While classification methods assign a single, unique mineral endmember to each pixel in an image, unmixing methods are more sophisticated and assign a proportional amount of each mineral endmember to each pixel. To speed up calculations, focus the problem and simplify the analysis, a subset of the image feature space is often. This is called feature selection process and involves selecting a subgroup of image bands or re-projection and simplification of the feature space (van der Meer, 2000).

3.2.2.1 Endmember Identification

The starting point for data analysis in hyperspectral image data is the identification of mineral endmember. An endmember means a pure mineral spectrum or a spectral mixture of materials of interest. Endmember selection can be achieved by using a spectral (field or laboratory) library or by picking the purest pixels in the image. Endmembers picked from image data are found to be superior to spectral library or laboratory endmembers because they represent the same residual atmospheric and instrumental characteristics (van der Meer, 2000).

Selection of spectral endmembers for unmixing or other types of analysis is crucial to understand imaging spectrometer data.

Identification of the purest pixels in the scene is done through a method called pixel purity index.

i. Pixel purity Index

The "Pixel-Purity-Index" (PPI) is a means of finding the most "spectrally pure," or extreme, pixels in multispectral and hyperspectral images (Boardman *et al*., 1995). The most spectrally pure pixels typically correspond to mixing endmembers. Due to the large amount of data, PPI is usually performed on MNF transformed data. If the image spectra are plotted in an n-dimensional space, the 'pure' pixels correspond to the corners (i.e. simplex vertices) of the multi-dimensional cloud of data points. The Pixel Purity Index is computed by repeatedly projecting n -dimensional scatter plots onto a random unit vector. The extreme pixels in each projection are recorded and the total number of times each pixel is marked as extreme is noted (Figure 3.4). A Pixel Purity Index (PPI) image is created in which the DN of each pixel corresponds to the number of times that pixel was recorded as extreme (RSI, 2005).

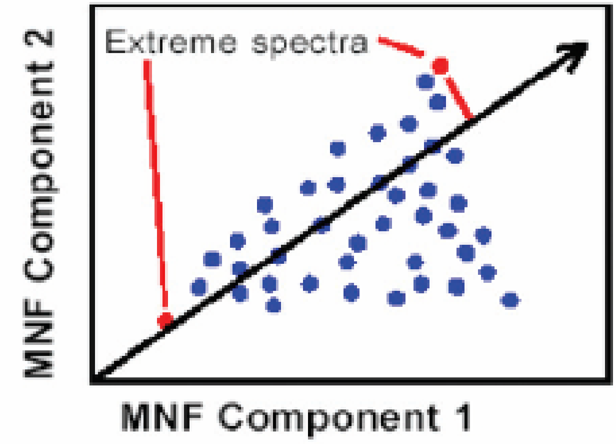

Figure 3.4 Extreme spectra in MNF component plane which used in PPI (RSI, 2005).

ii. Knowledge Based Identification

This approach involves the development of information index from geologic models in the studied area, manual data mining of the spectral response of image pixels, and collection and spectroscopic analysis of field samples. The preliminary activity should be a review of the literature to get a basic understanding of the geologic systems in the study area. This general information about the geology gives clues for the types of minerals that will be found in the field. The manual study of spectral image data is very useful to check the compatibility of image spectroscopy and the geologic model and provides some guidance for field work. Field inspection of the ground is the most critical part of endmember selection. Field sampling sites are planned according to the knowledge based index created by literature, the preliminary image analysis, and geologic experience. Field or laboratory spectroscopic analysis is carried out with the field samples to determine the suite of minerals that is present and important to the study.

There are a number of field portable reflectance spectrometers. Among the others the Labspec spectroradiometer is widely used in the mineral exploration industry. In this study Labspec 2600 is used which detailed in the next chapter.

3.2.2.2 Feature Selection

The vector space over all of the hyperspectral image bands is called feature space. Feature selection and feature extraction are methods for selecting or extracting a subset of the feature space for processing. Imaging spectrometer data are, in general, over determined with high band-to-band correlation (De Backer et al., 2005). The feature selection problem may be approached in a couple of ways. If the hyperspectral sensor has some reported defects on certain bands it is wise to eliminate those bands. The simplest approach is to apply knowledge of what parts of the spectra are important for a specific problem and use only those selected regions, like for clay minerals absorption features are in the SWIR part of the spectrum. The more general approach involves orthogonalization of the vector space and the use of sub-space projections. While technically elegant, orthogonalization can propagate noise through the vector space. While it may be used for noise reduction, this is only feasible in the case of a random noise model.

i. Minimum Noise Fraction

This method, developed by Green et al. (1988), is a principal-component-type orthogonalization rotation that results in components ordered in increasing rank of random noise. Thus, a subset of components may be selected that contains most of the image information and minimum noise. The output of the MNF transform is an image cube of n MNF bands. The output MNF bands are ordered by decreasing signal-to-noise ratio. The low-order components have the highest information content, while most of the noise is concentrated in the higher-order bands (Figure 3.5). The inherent dimensionality can be evaluated by examination of the associated images. In the higher order bands surface features are no longer visible and the image is dominated by noise (Hyperteach, 2006).

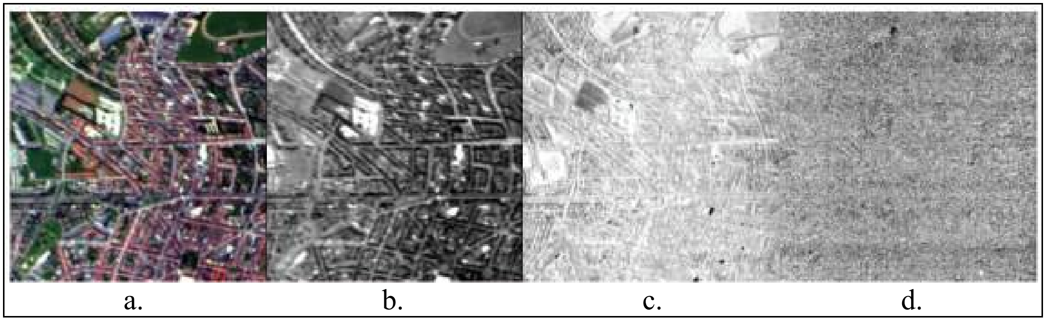

Figure 3.5 Results of MNF transformation starting from the original, respectively b. MNF band 2, c. MNF band 8 and d. MNF band 30 (Hyperteach, 2006).

The MNF rotation and subsetting solves two critical problems with hyperspectral data: it reduces dimensionality and it results in well-conditioned covariance and correlation matrices. After elimination of undesired bands, mineral endmembers may be found using the PPI method or predetermined endmembers may be used. If predetermined endmembers are utilized from the original image data or a spectral library, their spectra must be subjected to the same MNF rotation and subsetting as the image data.

3.2.2.3 Unmixing

The assumption that a pixel is composed of the linear spatial mixing of materials within the volume bounded by the pixel is the main idea behind spectral unmixing, all influencing characteristic spectral signatures together, resulting in the reflected electromagnetic radiation observed in imaging spectrometer data. With the assumption that all end member spectra are known, an inverse mixing process should lead to relative abundances of these end member materials per pixel. For the process of unmixing, endmembers should be properly defined, the mixture model also be formulated mathematically which are not easy steps with hyperspectral imagery (van der Meer and Bakker, 1998).

Because of the complexity of utilizing non-linear mixing models, remote sensing scientists rely almost exclusively on linear models. In the linear model it is assumed that the image spectrum is the concentration weighted sum of the component spectra (1). That is:

$$I = \sum_{i=1}^{n} W_i S_i \qquad (1)$$

Where:

I is the image spectrum

W_i is the ith weight

S_i is the ith component spectrum

These derived endmembers may actually represent mixtures themselves and not pure mineral spectra. Partial unmixing methods are used when a selected but incomplete set of endmembers are used. If not all endmembers are known or if only the abundance of a few endmembers should be mapped, partial unmixing methods like Matched Filtering, Constrained Energy Minimization (CEM) and Mixture Tuned Matched Filtering are performed (Boardman et al., 1995).

i. Matched Filtering (MF)

In matched filtering response of a known endmember is maximized and the response of the composite unknown background, is suppressed thus "matching" the known signature. It provides a rapid detection of specific minerals based on matches to specific library or image endmember spectra. Matched filter results are presented as gray-scale images with values from 0 to 1.0, which provide a means of relative degree of match estimation to the reference spectrum (where 1.0 is a perfect match) (Harsanyi and Chang, 1994).

The Match Filter (MF) forms the basis for most partial unmixing in remote sensing. The approach is to find a vector operator that suppresses the background spectrum and enhances the endmember spectrum. The operator is constrained to have minimum energy across all pixels and have an output of 1.0 for the endmember spectrum (van der Meer, 2000). The solution can be defined as:

$$X = \frac{[\rho]^{-1}[d]}{[d]^{t}[\rho]^{-1}[d]} \qquad (2)$$

Where:

X is the operator

ρ is the full image correlation matrix

d is the endmember spectrum

The operator X is applied for each endmember producing an image of endmember weights or proportions (2).

ii. Constrained Energy Minimization (CEM)

Constrained energy minimization is a spectral unmixing method which aims to increase the response of a target signature and suppresses the response of undesired background signatures on a pixel-by-pixel basis assuming that the foreground and background signatures are mixed linearly. The operator is very identical with the MF operator. The idea behind this is by minimizing the total output energy of all pixels and by assuming that the energy of an individual pixel summed across the wavelength range has to be 1 when applied to a target pixel spectrum. The CEM result is a vector component image that is reflecting the fraction abundance image of endmembers obtained through unmixing (van der Meer and Bakker, 1998).

iii. Mixture Tuned Match Filtering (MTMF)

Mixture Tuned Match Filtering (MTMF) is a partial unmixing method that is used extensively for mineral exploration remote sensing. It was developed by Boardman et al. (1995) and involves a number of processing steps.

MTMF applies matched filtering that also creates an additional output of Infeasibility image to the results. The infeasibility image is used as a tool to reduce the false positives may be found after matched filtering process. Pixels having a high infeasibility are likely to be matched filter false positives. Correctly mapped pixels will have a matched filter score above the background distribution around zero and a low infeasibility value.

The results of the mixture tuned matched filtering appear as a series of gray-scale images for each selected endmember. The matched filtering results provide an estimation of the relative degree of match to the reference spectrum, where 1.0 is a perfect match. The infeasibility results are in noise sigma units and indicate the feasibility of the matched filter result. Pixels that are correctly mapped will have a matched filter value above the background distribution around zero and a low infeasibility value (Figure 3.6). Pixels having a high matched filter result and high infeasibility are identified as "false positive" pixels and are removed from output of MF/CEM (RSI, 2005).

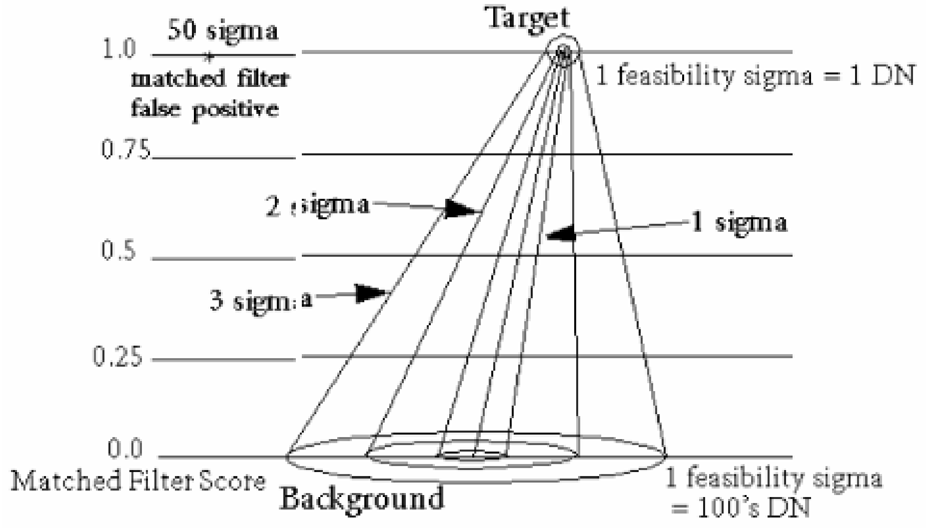

Figure 3.6 Relation between the match score and the infeasibility value (RSI, 2005).

The flowchart for a successful endmember classification from hyperspectral imagery data can be portrayed. Application of MNF to the image that is calibrated to relative reflectance is used for eliminating the noisy bands. The CEM/MF method is then applied using the transformed endmembers in MNF space. The ENVI implementation of MTMF produces an "infeasibility" image for each endmember component image. This image is used to cut out any false positive results produced by the CEM/MF technique.

3.2.2.4 Classification

In geological imaging spectrometry (i.e., hyperspectral remote sensing), mineralogical composition of the surface is obtained by statistical comparison and spectral matching algorithms. This process is called classification and involves the comparing and matching of known field or library spectra to unknown image spectra. Thematically these methods can be grouped as angle calculation (spectral angle measure, SAM), the vector distance (Euclidean distance measure, ED), the vector cross-correlation (spectral correlation measure, SCM), measurement of the discrepancy of probability distributions between two pixel vectors (the spectral information divergence, SID), brightness indexing (binary encoding), absorption feature characterization (waveform characterization), least squares fitting (spectral feature fitting) and use of correlation coefficients (cross-correlogram spectral matching).

i. Binary Encoding

In binary encoding, pixel spectra are encoded such that a one-zero representation of the brightness of a pixel in various spectral bands results using a threshold level equal to the average brightness of the pixel over all channels. Comparison of a pixel and laboratory encoded spectrum can be used to map mineralogy qualitatively. (van der Meer and Bakker, 1998).

ii. Waveform Characterization

In waveform characterization, absorption features known to be attributed to a certain mineral of interest are characterized in terms of their position, depth, width, and asymmetry on a pixel-by-pixel basis. These images can be combined to produce surface mineralogy maps; however, no rules exist to integrate the results nor do they provide absolute measures of abundance. (van der Meer and Bakker, 1998).

iii. Spectral information divergence measure

The spectral information divergence measure (van der Meer, 2006) calculates the distance between the probability distributions produced by the spectral signatures of two pixels (3, 4, 5, 6) defined as

$$\mathrm{SID}(r_i, r_j) = D(r_i \| r_j) + D(r_j \| r_i) \quad (3)$$

where

$$D(r_j \| r_i) = \sum_{l=1}^{L} q_l D_l(r_j \| r_i) = \sum_{l=1}^{L} q_l (I_l(r_i) - I_l(r_j)) \quad (4)$$

and

$$D(r_i \| r_j) = \sum_{l=1}^{L} p_l D_l(r_i \| r_j) = \sum_{l=1}^{L} p_l (I_l(r_j) - I_l(r_i)) \quad (5)$$

derived from the probabilities vectors $p = (p_1, p_2, \ldots, p_L)^T$ and $q = (q_1, q_2, \ldots, q_L)^T$ for the spectral signatures of vectors, s_i and s_j, where

$$p_k = s_{ik} / \sum_{l=1}^{L} s_{il} \quad \text{and} \quad q_k = s_{jk} / \sum_{l=1}^{L} s_{jl} \quad (6)$$

and $I_l(r_j) = -\log q_l$ and similarly $I_l(r_i) = -\log p_l$. Measures $I_l(r_j)$ and $I_l(r_i)$ are referred to as the self-information of r_j for band l. Note that equations above represent the relative entropy of r_j with respect to r_i (indicated with the || symbol) (van der Meer, 2006).

iv. Cross-correlogram Spectral Matching

Cross-correlogram Spectral Matching method as the name implies is based on pixel cross-correlograms (van der Meer and Bakker, 1998). For this approach, endmembers should be identified from a spectral library with the same spectral dimensions as the image data cube or from the scene itself. A pixel cross-correlogram is constructed by calculating the cross-correlation coefficient between a test spectrum (the pixel spectrum) and a reference spectrum (the laboratory or field spectrum) for different match positions by shifting the reference spectrum toward longer and shorter wavelengths over subsequent spectral channels (7). The cross-correlation is calculated as:

$$r_m = \frac{n\Sigma\lambda_r\lambda_t - \Sigma\lambda_r\lambda_t}{\sqrt{[n\Sigma\lambda_r^2 - (\Sigma\lambda_r)^2][n\Sigma\lambda_t^2 - (\Sigma\lambda_t^2]}} \qquad (7)$$

where r_m is the cross-correlation at match position m, λ_t is the test spectrum, λ_r is the reference spectrum, n is the number of overlapping positions (spectral bands), and m the match position.

The statistical assessment for the significance of the cross-correlation coefficient I is performed by using Student's t-test and the skewness as an estimator of the goodness-of-fit. Figure 3.7 shows cross-correlation images for the different match positions represented as a color-coded `3D' image cube. The face of the `3D' image cube displays skewness displayed in red, the significance in green and the cross-correlation at m=0 in blue as a color composite image. Thus, pixels appearing whitish are similar to the reference spectrum whereas other colors are obtained by the contribution of the three components in the RGB image. The top and right-hand sides of the cube are spectral slices which are formed by stacked cross-correlation images for the different match positions. Each line in a slice thus represents a color-coded pixel cross-correlogram which may be interpreted through the color ramp. the 3D cross-correlogram data cubes are used for creation of surface mineralogy maps for the different minerals by extracting pixels that have a high cross-correlation at m=0, a high significance, and a low skewness. From the match between pixel (test) and laboratory/field (reference) spectra which is expressed as a correlation with accompanying statistical significance, the method enables the user to get surface mineralogy information from image data.

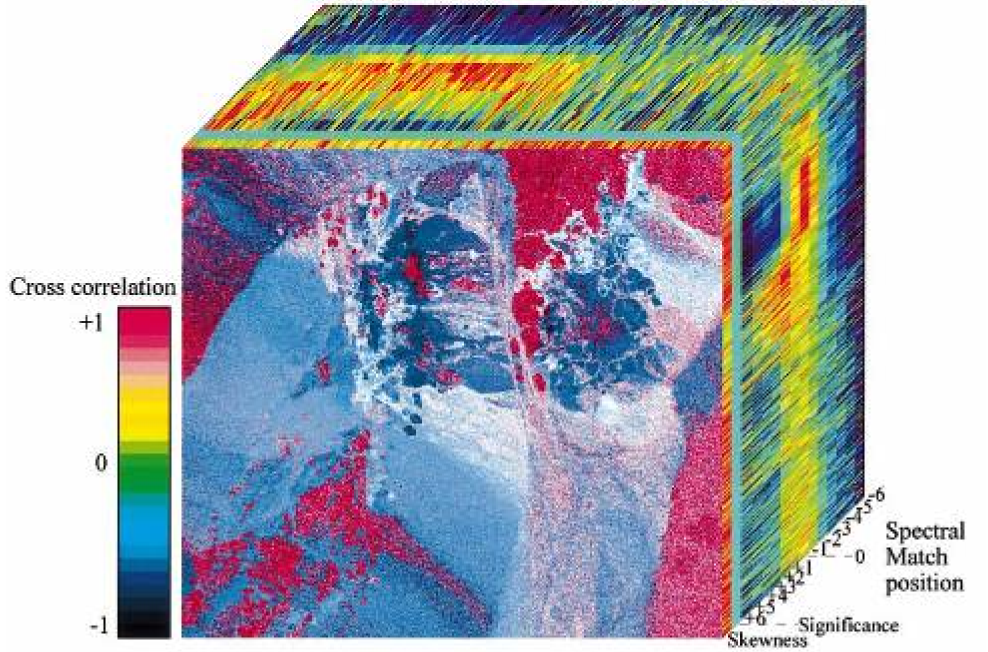

Figure 3.7 `3D' image correlogram cube for alunite. The face of the cube is an RGB image (red=skewness; green=significance; blue=cross-correlation at m=0) where pixels that are more similar to the mineral tested appear in white. The sides of the cube are spectral slices for the top line and right-hand column of the image build-up of cross-correlogram images and the skewness and significance (van der Meer and Bakker, 1998).

v. Spectral Feature Fitting (SFF)

Spectral feature fitting technique is based on waveform characterization. The relative goodness-of-fit between reference spectra and the unknown pixel spectra is calculated by least-squares fitting technique on a band-by-band phases. Result of the method is a root mean square image indicating the relative goodness-of-fit which can be interpreted qualitatively in terms of surface mineralogy (Clark et al., 1999).

Tetracorder is a version of Spectral Feature Fitting which is used by the USGS and also implemented in the ENVI package. Tetracorder includes some expert-system implementations in addition to the basic SFF methodology. The SFF method involves analysis of each spectral absorption feature and comparison of these against absorption features in endmember spectra.

In order to identify a spectral feature by its wavelength position and shape, it should be isolated from other effects, such as level changes and slopes due to other absorbing (or emitting) materials. These other absorbing or emitting sources which can be referred as background and continuum should be isolated and removed. Continuum removed absorption features, the depth and shape of these and endmember features (the endmember spectra are resampled to the image spectra resolution if needed) are compared. The result of the analysis is a feature depth metric and a goodness-of-fit metric (in the case of ENVI an RMS error image). These are typically combined to produce a classification image (Clark et al., 2003).

vi. Spectral Angle Mapper (SAM)

Spectral Angle Mapper is a simple feature space calculation that provides a similarity metric between each image pixel spectrum and endmember spectra in a space with dimensionality equal to the number of bands. In descriptive terms, SAM is the angle between the image spectrum vector and the endmember spectrum vector (8). It is defined mathematically as follows:

$$S = COS^{-1} \frac{\sum_{i=1}^{n} X_i U_i}{\sqrt{\sum_{i=1}^{n} X_i^{2} \sum_{i=1}^{n} U_i^{2}}} \qquad (8)$$

Where:

S is the spectral angle

X is the endmember spectrum

U is the unknown (image) spectrum

The SAM calculation results in a value of zero for good matches between the image spectrum and the endmember spectrum. It can be said that SAM approach is actually a "folded" version of the correlation coefficient. Thus, ideally perfect mirror images between the image and the endmember spectrum also produce a zero SAM angle (van der Meer and Bakker, 1998).

vii. Euclidian distance measure

The Euclidian distance (9) between two pixels in the n-dimensional spectral feature space is derived from the spectral angle measure as

$$\begin{aligned} \mathrm{ED}(s_i, s_j) &= 2\sqrt{1 - \cos\left(\mathrm{SAM}(s_i, s_j)\right)} \\ &= 2\sin\left(\frac{\mathrm{SAM}(s_i, s_j)}{2}\right) \end{aligned} \qquad (9)$$

The main difference of the Euclidean distance measure as compared to the spectral angle is that the ED takes into account the brightness difference between the two vectors, whereas the spectral angle (and the spectral correlation) are invariant with brightness (van der Meer, 2006).

viii. Spectral Correlation Mapper (SCM)

The spectral correlation measure is calculated as the correlation coefficient of the pixel (portrayed as vector in an n-dimensional feature space) and their respective spectral signatures. Classification using a cross-correlation approach provides a direct measurement of the similarity between the shapes of two spectra. SCM calculation is not affected with the amplitude differences between the image and endmember as it takes into account the relative (overall) shape of the spectrum as well as the spectral match (10). The SCM method is defined mathematically as follows:

$$R = \frac{\sum_{i=1}^{n}[(X_i - \overline{X})(U_i - \overline{U})]}{\sqrt{\sum_{i=1}^{n}(X_i - \overline{X})^2 \sum_{i=1}^{n}(U_i - \overline{U})^2}} \qquad (10)$$

Where:

R is the correlation coefficient

X is the endmember spectrum

$\overline{X}$ is the mean of the endmember spectrum

U is the unknown (image) spectrum

$\overline{U}$ is the mean of the unknown (image) spectrum

The correlation can be both positive as well as negative and as such partly takes brightness differences and shape difference between spectra into consideration. As a result, a correlation coefficient image in which each pixel is assigned a value between -1.0 and 1.0 for each endmember mineral spectrum is created. A value of 1.0 denotes an exact match between the endmember spectrum shape and the image spectrum shape whereas a value of -1.0 is an exact inverse match (van der Meer, 2006).

CHAPTER 4

DATA & ANALYSIS

4.1 Methodology of Study

This study is completed in seven major stages. The first stage is the data acquisition that will be used in this study. Next stage is the preprocess stage including spatial and spectral subsettings made in order to reduce the data dimensionality and to increase the validity of the results. CTIC correction, atmospheric correction and masking are also performed during this stage.

Third stage involves the endmember identification procedures. At the end of this stage, minerals that will be used in analysis are determined.

Fourth stage is the analysis carried out to determine the alteration minerals which involves the unmixing and classification procedures.

Fifth stage is the geometric correction of the analysis result for assessing and interpretation.

Sixth stage is the validation of the results obtained in previous stages through accuracy assessment by using the image and field data.

Lastly in the seventh stage the outputs of the analysis are interpreted with the geological background.

Summary of the methodology is illustrated in the flow chart in Figure 4.1.

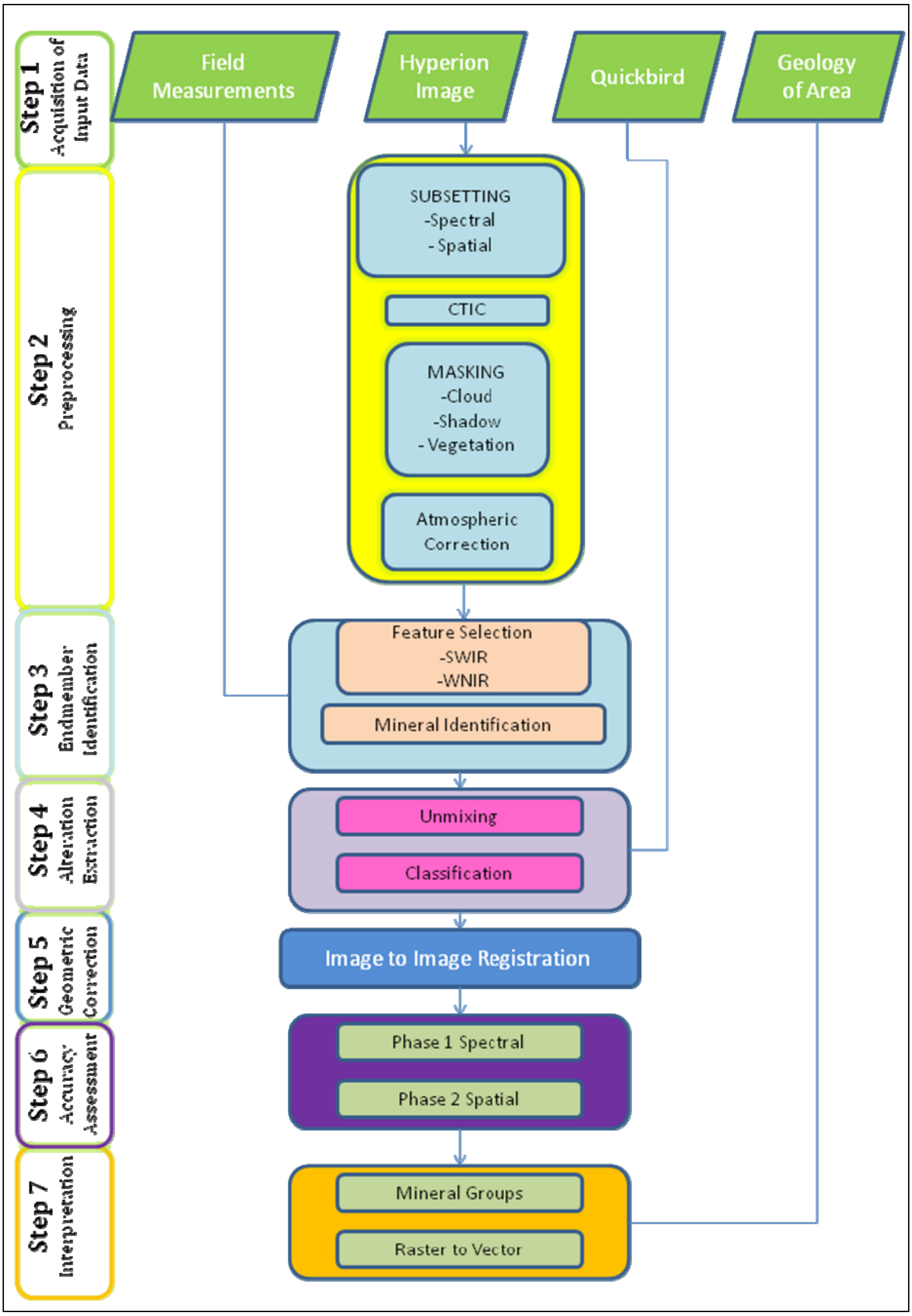

Figure 4.1 Flow chart of the processing steps.

4.2 Data Used

Different input data are used for mineral identification in this study. Image data is gathered from EO-1's (Earth Observing 1) Hyperion sensor. Orthorectified Quickbird image is used in geometric correction. Field spectroscopic measurements are made by using PIMA and ASD spectrometers. Additionally, ancillary digital elevation data (DEM) is used for orthorectification of Quickbird image.

4.2.1 Hyperion

The Hyperion Imaging Spectrometer was the first imaging spectrometer to routinely acquire science-grade data from earth orbit. The Hyperion pushbroom instrument was designed as a technology demonstration and provided high-quality calibrated data for hyperspectral application evaluations. With Hyperion, each pushbroom image frame captured the spectra from an area of 100 km along-track by 7.7 km cross-track with 30 m spatial resolution. The forward motion of the satellite created a sequence of frames that were combined into a 2-D spatial image with a third dimension of spectral information (called a "three-dimensional data cube") (Christian and Krishnayya, 2007).

Hyperion's 242 bands covered the visible, near-infrared, and shortwave infrared bands (400–2500 nm) with 10-nm bandwidths; typically 198 bands are provided in the calibrated data (Table 4.1).

Table 4.1 Number of bands in raw Hyperion data delivered.

Wavelength	Number of bands
VNIR (350-1104 nm)	96
SWIR (1114-2577 nm)	146

The Level 1R radiometrically corrected Hyperion product was supplied by the EO-1 Product Generation System (EPGS). The primary function of the EPGS is to perform radiometric calibration and nominal artifact corrections on the level 0 (‘raw’) Hyperion data. The Hyperion data were initially corrected by TRW (Thompson Ramo Woolridge). Based on the same algorithm, the NASA EO-1 Science Office developed the Level 1R processing code that the EPGS now uses (with slight modifications) to generate the USGS product. These USGS Level 1R products are being provided to the public since December 2001. Level 1R algorithms include many processing steps like pre-1R corrections (SWIR only), background removal, rescaling for DN output, bad pixel mask generation, VNIR/SWIR alignment and output data preparation. The Level 1R algorithm output is provided in scaled at-sensor radiance values, with data stored as 16-bit signed integers. The radiance units are in W/(sq. mSr × μm). The Level 1R data output needs to be rescaled by the user to obtain the original radiance values. The data were scaled by 40 for the VNIR and 80 for the SWIR to convert the Level 1R data to units of radiance.

The first 70 bands were in the VNIR in the spectral range from 356 to 1058 nm with an average full-width at halfmaximum (FWHM) of 10.90 nm and stored as 1.80 × 40 × DN in W/(sq. mSr × μm). The remaining 172 bands were in the SWIR, and ranged from 852 to 2577 nm, with an average FWHM of 10.14 nm. They were stored as 1.18 × 80 × DN in W/(sq. mSr × μm).

A full Hyperion dataset has 256 columns and 6460 rows with the pixel size of 30 m. The data, with 12-bit quantization, were stored in HDF format as signed 16-bit integers with BIL interleaving (Christian and Krishnayya, 2007).

For the image to be used in this study three shots are made by operator (USGS) on August 29th, October 09th , and November 06th 2008 having total cloud coverages as 12 %, 69 % and 64 %, respectively. Because of the lowest cloud coverage, dataset recorded on August 29th 2008 is ordered and used throughout the study (Figure 4.2). Selected dates were decided on seasonal considerations as the region is snow and cloud free for only a couple of months. Hyperion Level 1 product is available in Hierarchical Data Format (HDF) with the bands written as band interleaved (BIL).

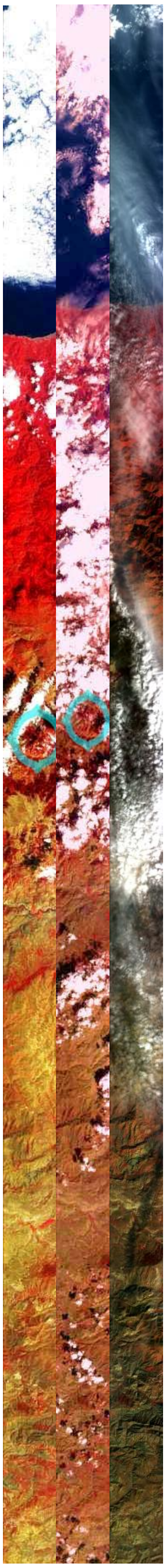

Figure 4.2 Image previews of the 3 shots made on August 29th, October 09th and November 06th 2008 from left to right. (Study area is highlighted with a circle)

4.2.2 Quickbird

Quickbird is a high resolution multispectral imaging satellite having 0.61 m in panchromatic and 2.4 m in multi spectral bandwidths. It is corrected both radiometrically and geometrically in sensor. The bandwidths are summarized in Table 4.2. With the 450 km altitude the swath width is 16.5 km and delivered as square frames.

Table 4.2 Number of bands in Quickbird data delivered.

Wavelength	Number of bands
Panchromatic (445-900 nm)	1
Blue (450-520 nm)	1
Green (520-600 nm)	1
Red (630-690 nm)	1
Near-IR (760-900 nm)	1

The data is ordered as Pan-sharpened which means the multispectral bands are fused with Panchromatic band and delivered as true color images at 0.61 m spatial resolution.

Quickbird image used in this study is ordered to be recorded in August 2004 and it is received on the first shot having 3% cloud coverage. The full image consists of 11691 columns and 20021 rows and the image is not subsetted for the rest of the study (Figure 4.3).

4.2.3 ASD Spectrometric Measurements

The Labspec 2600 spectrometer is a field portable reflectance spectrometer that is commonly used in the mineral exploration industry. The instrument utilizes an internal controlled light source to illuminate a small sample (Figure 4.4). Measurements are made between 350 nm and 2500 nm. The spectral bandwidth is variable: 3 nm @ 700 nm and 6 nm @ 1400/2100 (ASD, 2009).

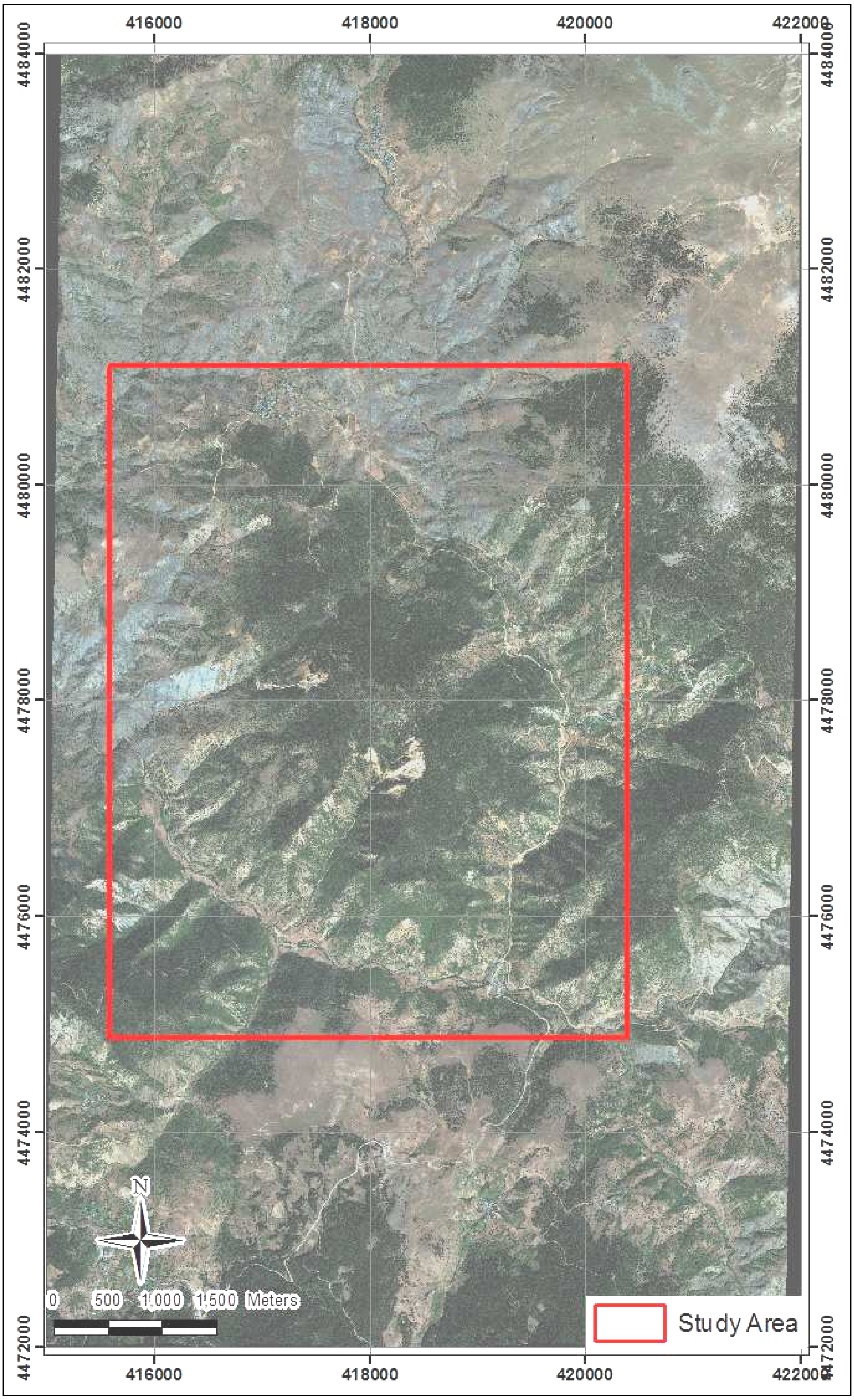

Figure 4.3 Quickbird coverage and the study are highlighted.

The entire spectral range is sampled every 100 milliseconds but multiple samples are normally collected and averaged to reduce the instrument noise. The instrument has a high signal to noise ratio of 14,500 S/N at 1400 nm. A one-dimensional 512-element silicon photodiode array is used for measurements in the VNIR and two cooled indium-gallium-arsenide photodiodes are used for measurements in the SWIR. The SWIR wavelengths are measured sequentially during the 100 ms sample period with a rotating mirror and diffraction grating assembly (ASD, 2009).

Figure 4.4 General view of ASD Labspec 2600 portable spectrometer (ASD, 2009).

ASD field spectrometric survey includes 566 samples. This survey is carried out for all samples with selectively representing grab samples taken from the selected sites. Measurements are performed on the weathered surfaces of the samples in dry conditions in the core shed located in the field. The instrument is not taken to the outcrop as the device generated its own illumination. The result of this survey created a field spectral library that is used for endmember selection and accuracy assessment in the later stages of this study.

4.2.4 PIMA Spectrometric Measurements

Being one of the first deployments of portable spectrometer devices, PIMA is an infrared spectrometer that operates in the short wave infrared region of the electromagnetic spectrum for the analysis of mineral and vegetation species (Figure 4.5). The instrument has high spectral resolution in the SWIR (1300 - 2500 nanometers) with sampling interval of 2 nm at 7 nm spectral resolution (Pima, 2009).

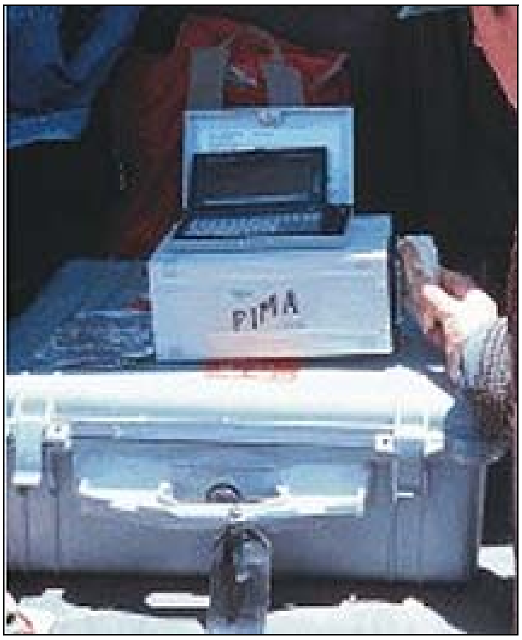

Figure 4.5 The Pima spectrometer (Pima, 2009).

A total of 734 samples are surveyed by using Pima portable spectrometer. The original raw spectrometric data was not available however mineral classifications were provided in a database for all measurements. In endmember identification these mineral classes are used as an ancillary data.

4.2.5 Digital Elevation Model

The elevation model is obtained from digitized 1:25.000 scaled topographical sheets of Turkish General Directorate of Mapping. Originally 10 m elevation contours are digitized with RMS error lower than 0.1. The outputs are all georeferenced to ED50 datum and UTM zone 37 projection (Figure 4.6).

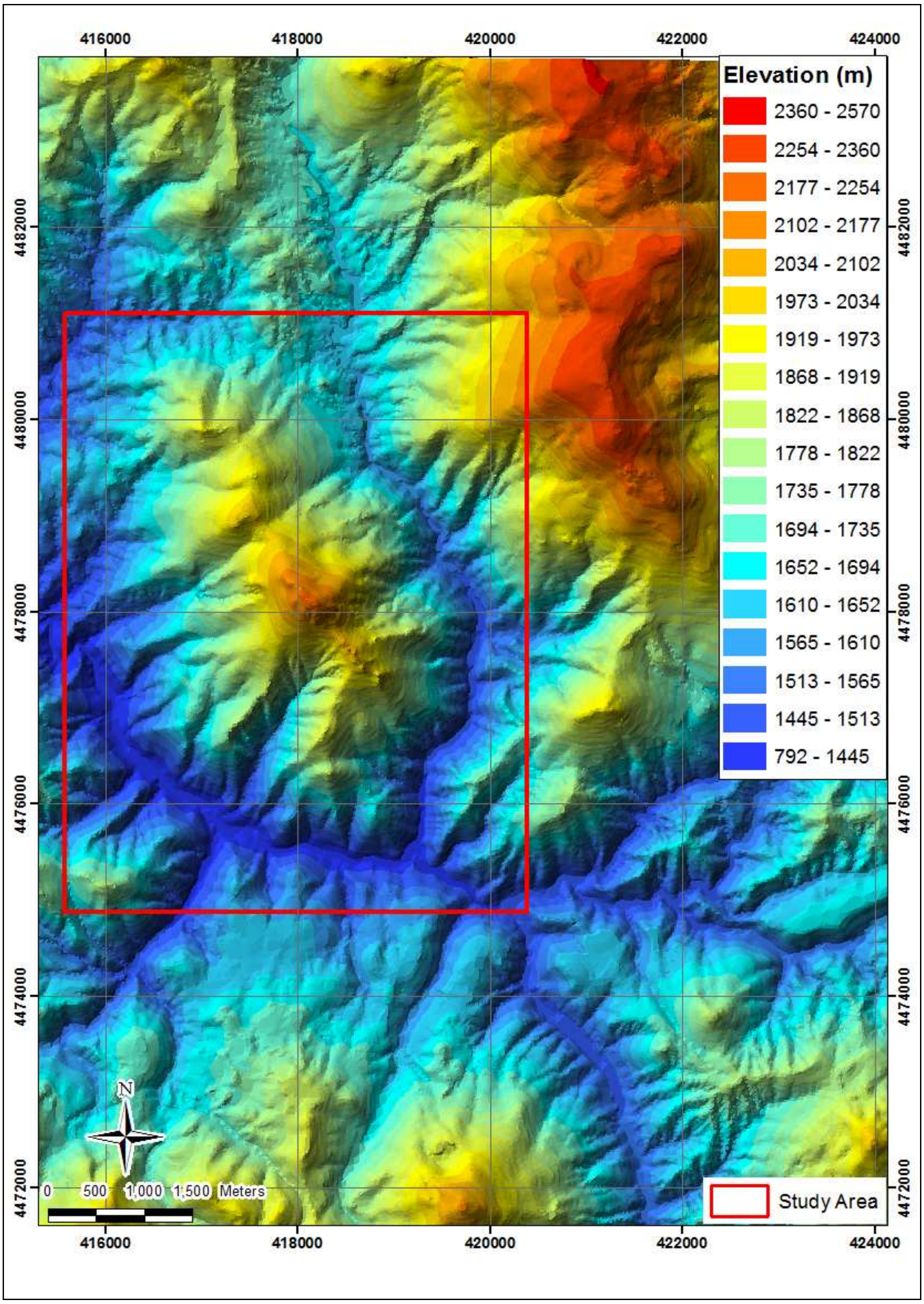

Figure 4.6 Digital Elevation Model of the study area.

The digital elevation model is used in orthorectification of Quickbird image which will be used for the geometric correction of Hyperion image. This process will be described in the fifth stage of the methodology.

4.3 Data Quality

The Level 1 Radiometric product has a total of 242 bands but only 198 bands are calibrated. Because of an overlap between the VNIR and SWIR focal planes, there are only 196 unique channels. Calibrated channels are 8-57 for the VNIR, and 77-224 for the SWIR. The reason for not calibrating all 242 channels is mainly due to the detectors' low responsivity. The bands that are not calibrated are set to zero in those channels (Pearlman et al., 2003).

The delivered USGS Hyperion product contains 242 bands, of which 44 were not calibrated. The main reason for not calibrating all the bands was the decreased sensitivity of the detectors within the non-calibrated spectral regions. Out of the 242 collected bands, bands 1–7 (356– 417 nm) and bands 225–242 (2406–2578 nm) were not calibrated. Bands 58–70 (collected by the VNIR instrument) and bands 71–76 (collected by the SWIR instrument) were also not calibrated (Figure 4.7).

The SWIR spectrum was divided into SWIR-1 (1.3–1.9 nm) and SWIR-2 (1.9–2.5 nm). Thus, the final L1R data product provided a total of 198 bands representing continuous spectra from 427 to 2395 nm.

The collected and calibrated channels also include a small area of spectral overlap between the VNIR and SWIR spectrometers (bands 56–57 and 77–78; from ~912 to ~923 nm). Therefore, out of the 198 calibrated bands, there were 196 unique spectral channels. All bands that were not calibrated were set to zero (null values) in the Level 1R product.

The Hyperion sensor has a signal-to-noise ratio ranging (SNR) from 190 to 40 as measured by Pearlman et al. 2003. This ratio gradually decreases from VNIR to SWIR (Figure 4.8).

Other than the uncalibrated bands the Hyperion sensor has instrumental defects which are striping and goniometric smile effect. The L1R level of correction removed the systematic striping along and across track but the remaining stripes are accepted as scene dependant and are not fully understood (Pearlman et al., 2003).

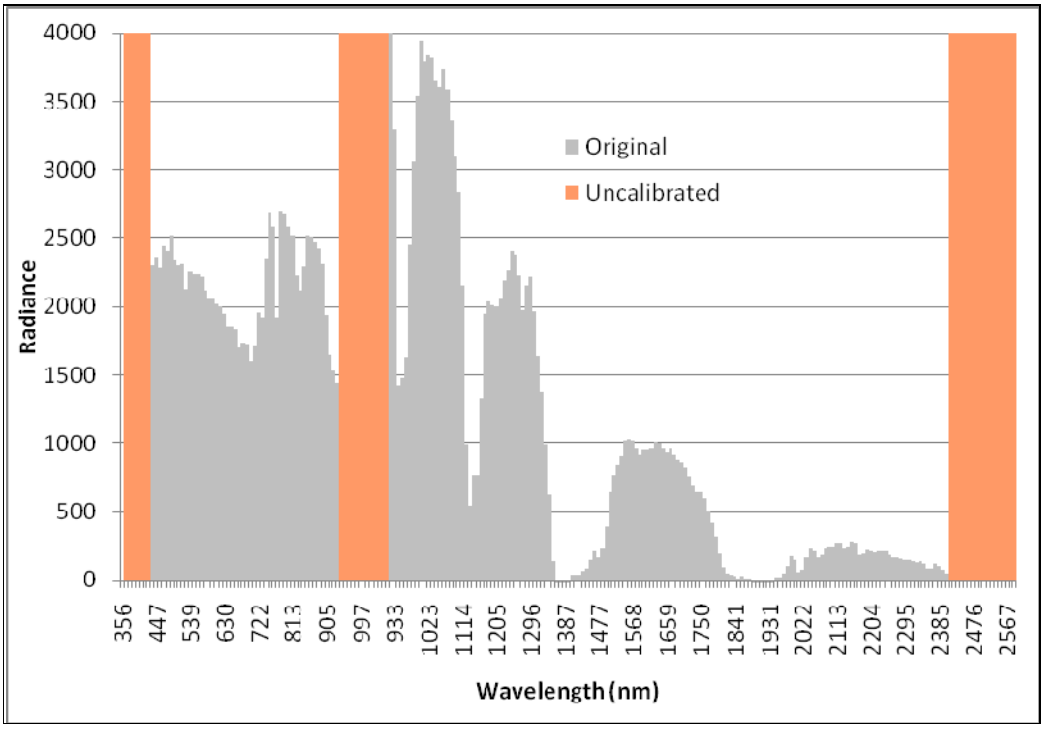

Figure 4.7 Uncalibrated bands (red) in delivered Hyperion image.

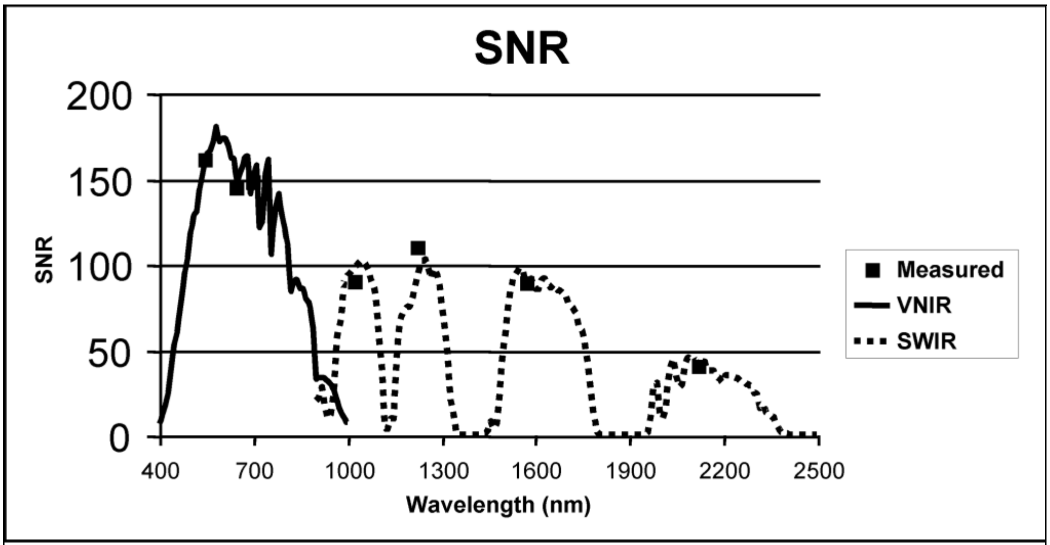

Hyperion Measured SNR						
550 nm	650 nm	700 nm	1025 nm	1225 nm	1575 nm	2125 nm
161	144	147	90	110	89	40

Figure 4.8 Hyperion signal to noise comparison (Pearlman et al., 2003).

Smile effect is generally a pushbroom technology defect. The central wavelengths and/or the FWHMs change across the pixels (samples) of the array up to 3 nm in the VNIR and lower in SWIR. The normal method of correcting this goniometric effect is to fit a curve to the average of the image columns as each column has a consistent contribution to the effect (Landgrebe, 2003). To correct this defect, cross track illumination correction routine in ENVI software used.

The preprocessing of Hyperion data in the following sections includes radiometric correction, atmospheric correction and geometric correction.

Quickbird dataset is received as radiometrically and geometrically corrected. Additional orthorectification is applied with RMS accuracy of 0.5 by using the digital elevation data having. Quickbird dataset is used as a base image for Hyperion geometrical correction and also for the plots in the following chapters.

4.4 Pre-Processing

As discussed previously the Hyperion data is gathered with basic systematic corrections applied. However, to convert the radiance to reflectance and to correct the data, certain preprocessing steps should be applied before further analysis.

The Level 1 product is only radiometrically corrected for systematic errors and is not geometrically corrected. Geometrical correction is carried out at the end of the analysis stage before accuracy assessment level to avoid any side effects caused during the resampling.

Four individual pre-processing steps are carried out as:

- Spatial and spectral Subsetting
- Cross Track Illumination Correction (CTIC)
- Radiometric Correction
- Masking

4.4.1 Subsetting

Although radiometrically standardized, image data include the uncalibrated bands together with the very low SNR bands. Both to reduce the data dimensionality, spatially and spectrally, the image is subsetted.

Spatially the extent of the image selected is based on the available geological map prepared in detail for alteration at 1:5000 scale. The subsetted image data is composed of 256 columns and 400 rows (Figure 4.9). Study area is partly covered by clouds and shadows which will become the primary focus of the next section.

Other than the spatial subsetting the next subsetting issue is the removal of problematic bands from the raw image. These bands consist of two types; first type was the uncalibrated bands that were mentioned above. The second type of elimination is carried out by examining the spectral signatures and bands having spiky and noisy radiance are selected and removed. With the eliminated ones total number of bands are reduced from 242 to 173. Spectral subsetting is summarized in Table 4.3.

4.4.2 Cross Track Illumination Correction

Cross Track Illumination Correction (CTIC) is described as the spectral variation across the field of view (Pearlman et al., 2003). Hyperion data has a “smile” error detected on prelaunch tests. Decreasing magnitudes of this variation was also recorded on VNIR and SWIR spectrometers respectively.

CTIC technique tries to fit the illumination variation to a polynomial equation. The fitted variation is either subtracted from the original data or used to divide it. While correcting the illumination correction, application can create degradation in original illumination in high order removal. All parameters are tested before deciding on the polynomial order and the operator. CTIC effects are best displayed and cross checked in Minimum Noise Fraction (MNF) space. Figures 4.10 and 4.11 display the first MNF images of several orders of CTIC modeled and removed both additively and multiplicatively.

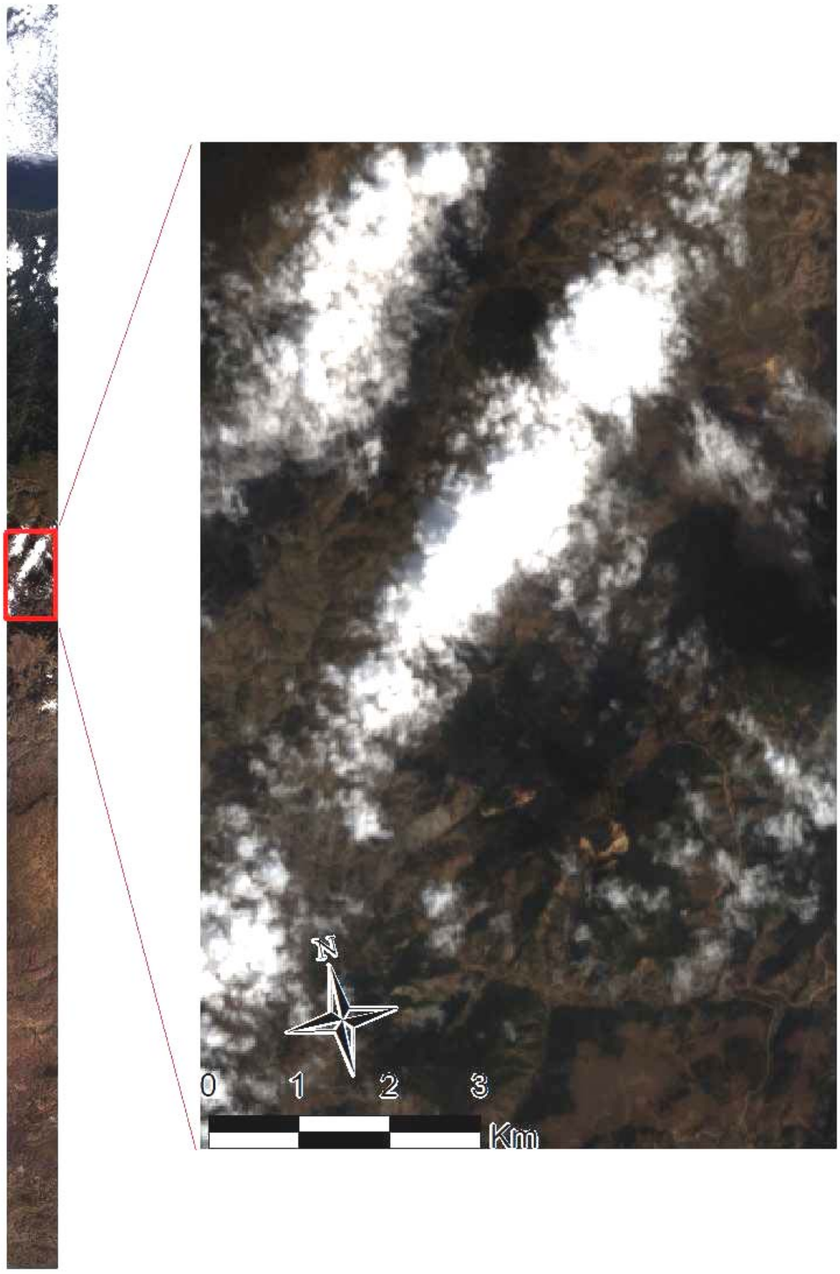

Figure 4.9 Spatial subsetting in True color representation (B29, 20, 11 as RGB).

Table 4.3 First pass of Spectral subsetting

	Spectral Bandwidth	Number of Bands
Original	355 – 2577 nm	242
Subsetted	426 – 2395 nm	173

As the MNF composites display, the best results are observed by applying the third order polynomial using additive model. Figure 4.12 compares the raw and the CTIC corrected image data.

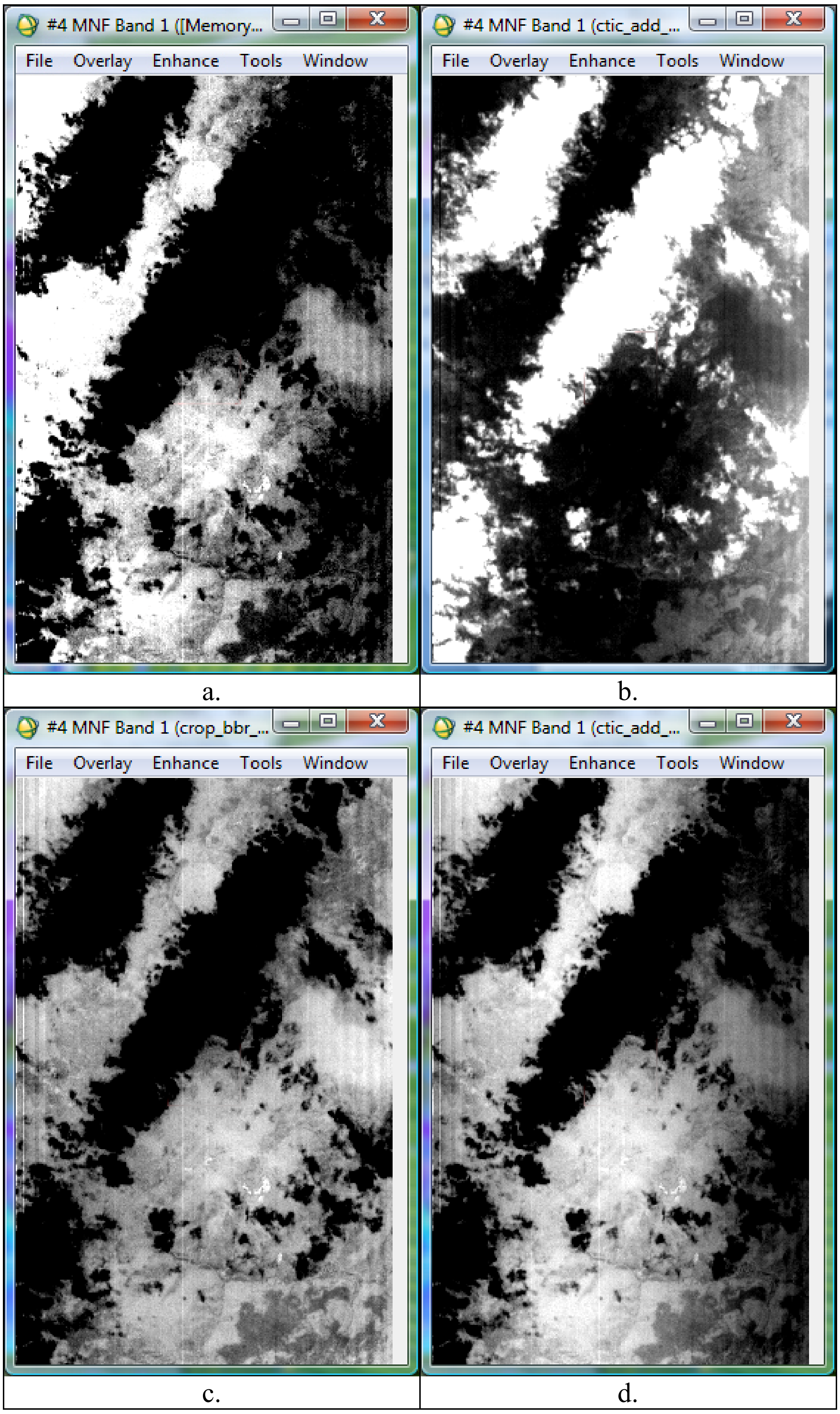

Figure 4.10 First MNF bands of respectively first, second, third and fourth order additive CTIC corrected image.

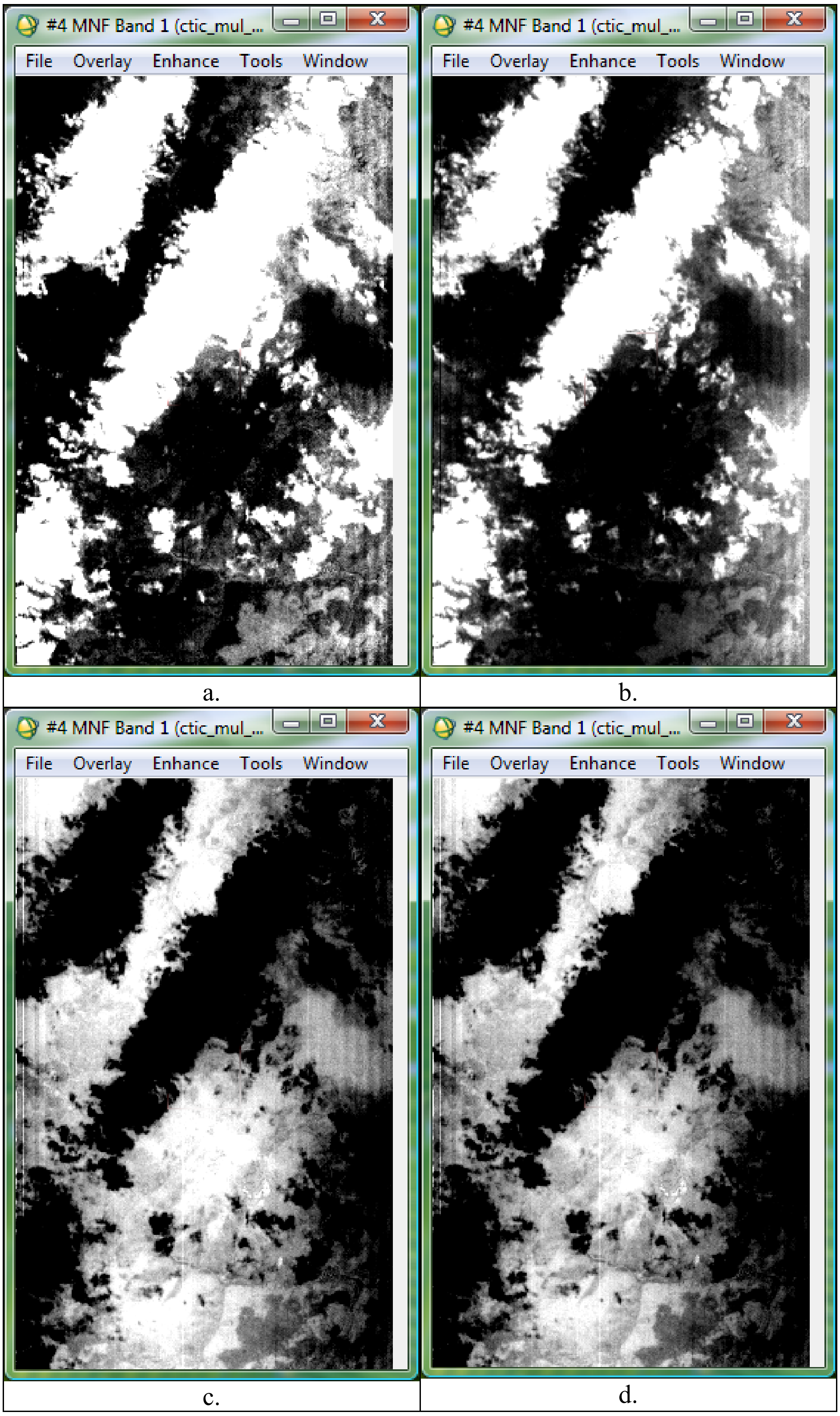

a. b. c. d.

Figure 4.11 First MNF bands of respectively first, second, third and fourth order multiplicative CTIC corrected image.

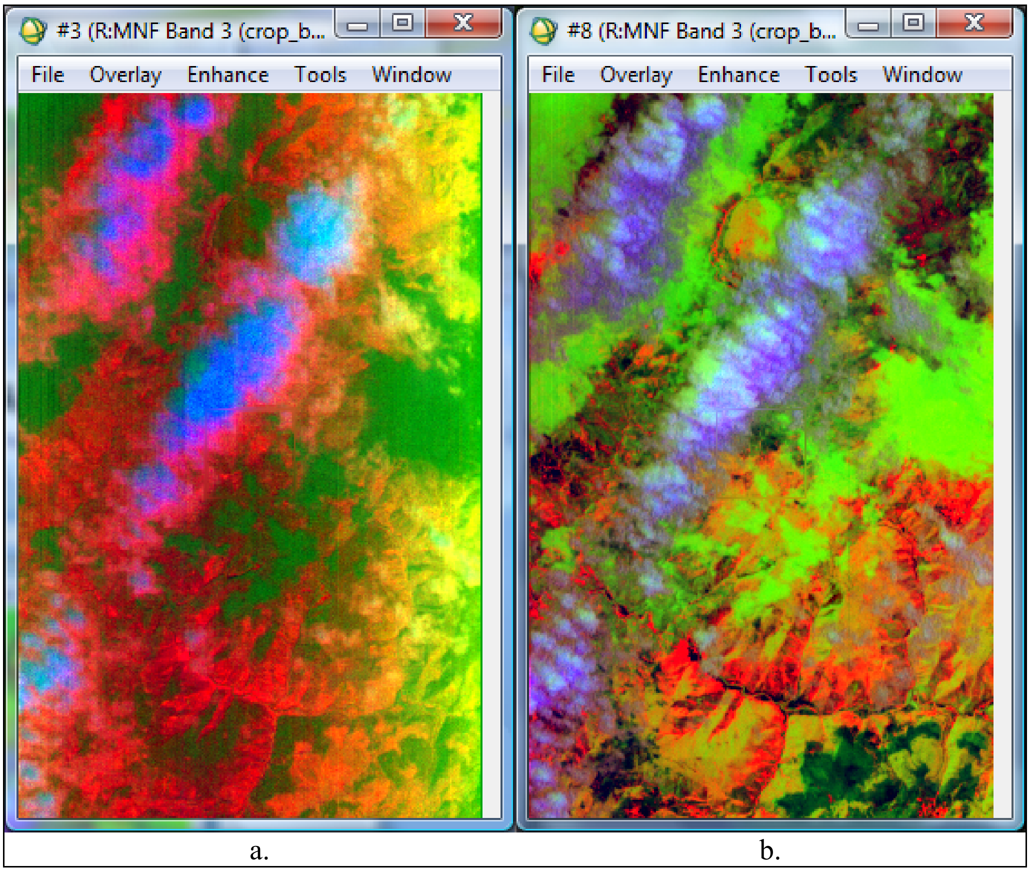

a. b.

Figure 4.12 Comparison of MNF bands. MNF 3,2,1 as RGB. a. Before CTIC b. After CTIC

4.4.3 Masking

This process is carried out to mask three features out of the image data. These are cloud, shadow and vegetation.

i. Cloud Masking

Original image data has a certain amount of recorded cloud pixels which is measured by in-satellite measuring devices. In order to clean the image from any unwanted and noisy pixels the cloud is needed to be identified.

For identification of cloud “water column vapor band” is created by ENVI’s radiometric correction tool (FLAASH). For the first phase of the study, shadow is not masked, only cloud masking is performed. Then this band is used to generate a cloud mask using ENVI Region of Interest (ROI) tool with thresholding the water column index band with maximum value of 1320.

Striping effects are manually removed from the mask. In Figure 4.13 cloud band, the mask and the masking result is shown.

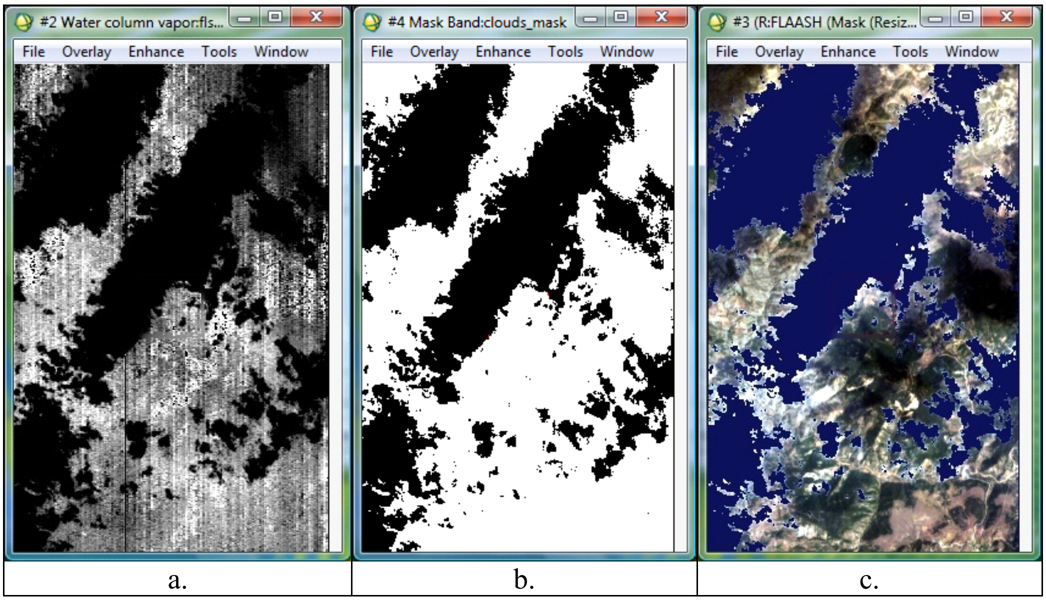

a. b. c.

Figure 4.13 Cloud masking steps, a. Water column vapor band after FLAASH, b. cloud mask, c. masking output.

ii. Shadow Masking

The presence of cloud brings another type of noise which is shadow. Signal processing techniques are experimentally applied for lightening or normalizing the dark pixels, but it is risky to change original values especially with a low signal quality. Therefore shadow is decided to be removed.

Different sources can be incorporated to obtain shadow information from the image. MNF can be used to threshold the shadow manually. ENVI’s Sequential Maximum Angle Convex Cone (SMACC) module, being an automated endmember extraction tool can be used conveniently. The conventional method, visualizing PPI result in n-dimension and selecting endmembers manually, is handled in a faster way. The method generates shadow as one of the endmembers. This shadow abundance band can be thresholded to mask the shadow (Figure 4.14).

iii. Vegetation masking

Green vegetation is another type of unwanted data class known to exist in the image.

Normalized Difference Vegetation Index (NDVI) is used to mask green vegetation in order to concentrate only on vegetation free areas. NDVI is obtained by the equation:

$$NDVI = (P_{NIR} - P_{RED}) / (P_{NIR} + P_{RED})$$

Parameters used are as follows:

P_{NIR}: 762.6 nm

P_{RED}: 640.5 nm

The ratio 0.4 is used to threshold the NDVI result after several trials and comparing with the ground controls.

Figure 4.14 shows the final output for the masking of cloud, shadow and vegetation.

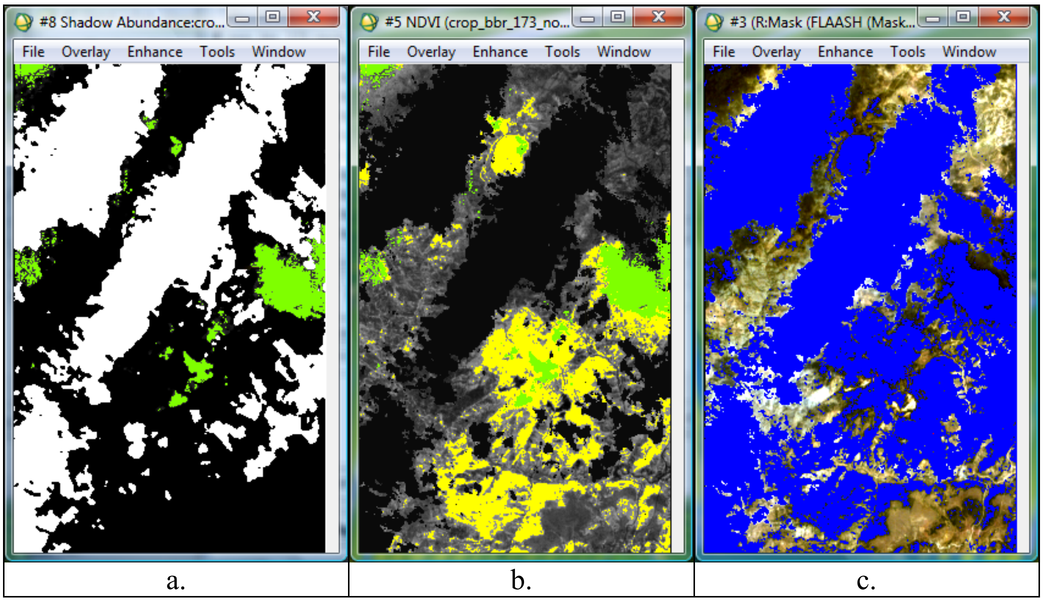

a. b. c.

Figure 4.14 Final masking sequence as a. cloud masking, b. Shadow and NDVI c. Combined.

4.4.4 Radiometric Correction

In order to use the field and library spectra to compare with the image data in mineral identification, hyperspectral image data required to be corrected radiometrically and converted to relative reflectance.

Different methods were tested for the calibration of the Hyperion data. Data dependent internal average reflectance (IAR) and flat-field methods were found to be inappropriate due to intense vegetation cover and lack of spectrally flat areas.

For the removal of the atmospheric effect and to convert radiance at sensor data to reflectance, data modeling is used via help of ENVI Fast Line-of-sight Atmospheric Analysis of Spectral Hypercubes (FLAASH) atmospheric modeling software.

The digital values of Hyperion Level 1 product are 16-bit radiances (L) and are stored as 16-bit signed integer. The VNIR bands have a scaling factor of 40 and the SWIR bands have a scaling factor of 80 applied. The units are in (W) / (m^2 SRμm) (SR).

$$\text{VNIR } L = \text{Digital Number} / 40$$

$$\text{SWIR } L = \text{Digital Number} / 80$$

Hyperion Level 1b data are in units of (W) / (m^2 SRμm x 40) for the VNIR or x 80 for the SWIR. FLAASH atmospheric correction software uses units of (microW) / (cm^2 nm SR) so the scaling factors used in FLAASH should be 400 for the VNIR and 800 for the SWIR because there is an extra factor of 10 when using FLAASH.

Water absorption feature at 1135 nm is used to create cloud mask and water column vapor image as additional outputs as explained in cloud masking section (Figure 4.15). As the image is recorded on 29th of August atmospheric and aerosol models are selected as Mid-Latitude Summer and Rural respectively.

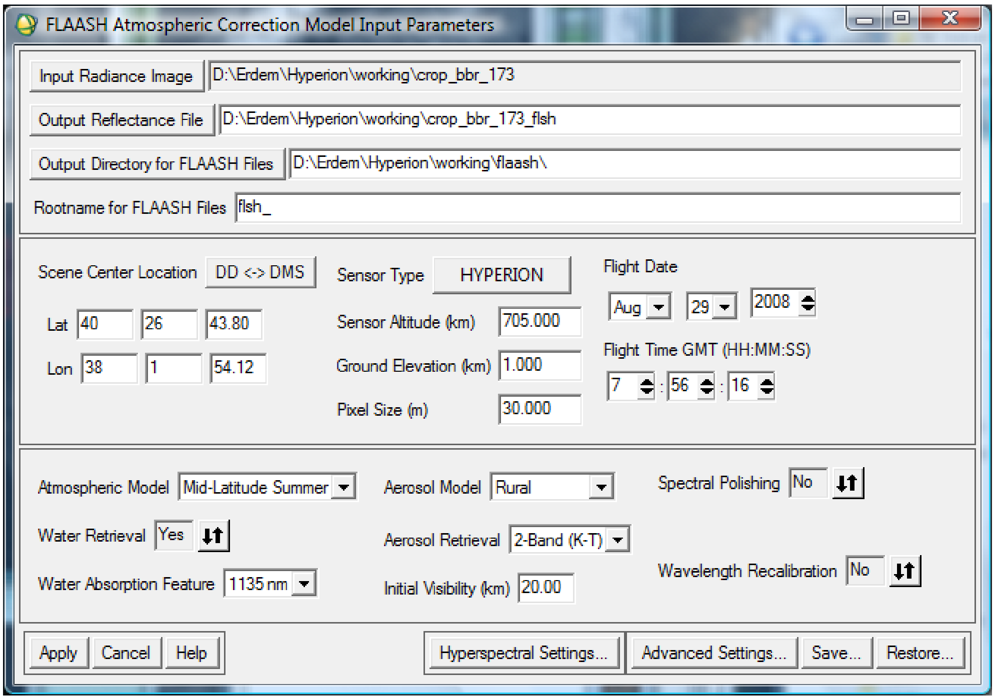

Input Radiance Image: D:\Erdem\Hyperion\working\crop_bbr_173
Output Reflectance File: D:\Erdem\Hyperion\working\crop_bbr_173_flsh
Output Directory for FLAASH Files: D:\Erdem\Hyperion\working\flaash\
Rootname for FLAASH Files: flsh_
Scene Center Location
Lat: 40 26 43.80
Lon: 38 1 54.12
Sensor Type: HYPERION
Sensor Altitude (km): 705.000
Ground Elevation (km): 1.000
Pixel Size (m): 30.000
Flight Date: Aug 29 2008
Flight Time GMT (HH:MM:SS): 7 : 56 : 16
Atmospheric Model: Mid-Latitude Summer
Water Retrieval: Yes
Water Absorption Feature: 1135 nm
Aerosol Model: Rural
Aerosol Retrieval: 2-Band (K-T)
Initial Visibility (km): 20.00
Spectral Polishing: No
Wavelength Recalibration: No

Figure 4.15 FLAASH parameters used for modeling the atmospheric conditions.

4.4.5 Geometric Correction

The geometric correction is conventionally considered as a preprocessing step, however, in order not to degrade the data this step is carried out after the unmixing and classification steps.

Image to image registration is performed by using georeferenced Quickbird as base image and the Hyperion image as the warp image (image to be warped). Forty seven locations are selected as ground control points and nearest neighborhood resampling is used. The calculated root mean square (RMS) score is 1.14 (Figure 4.16).

]

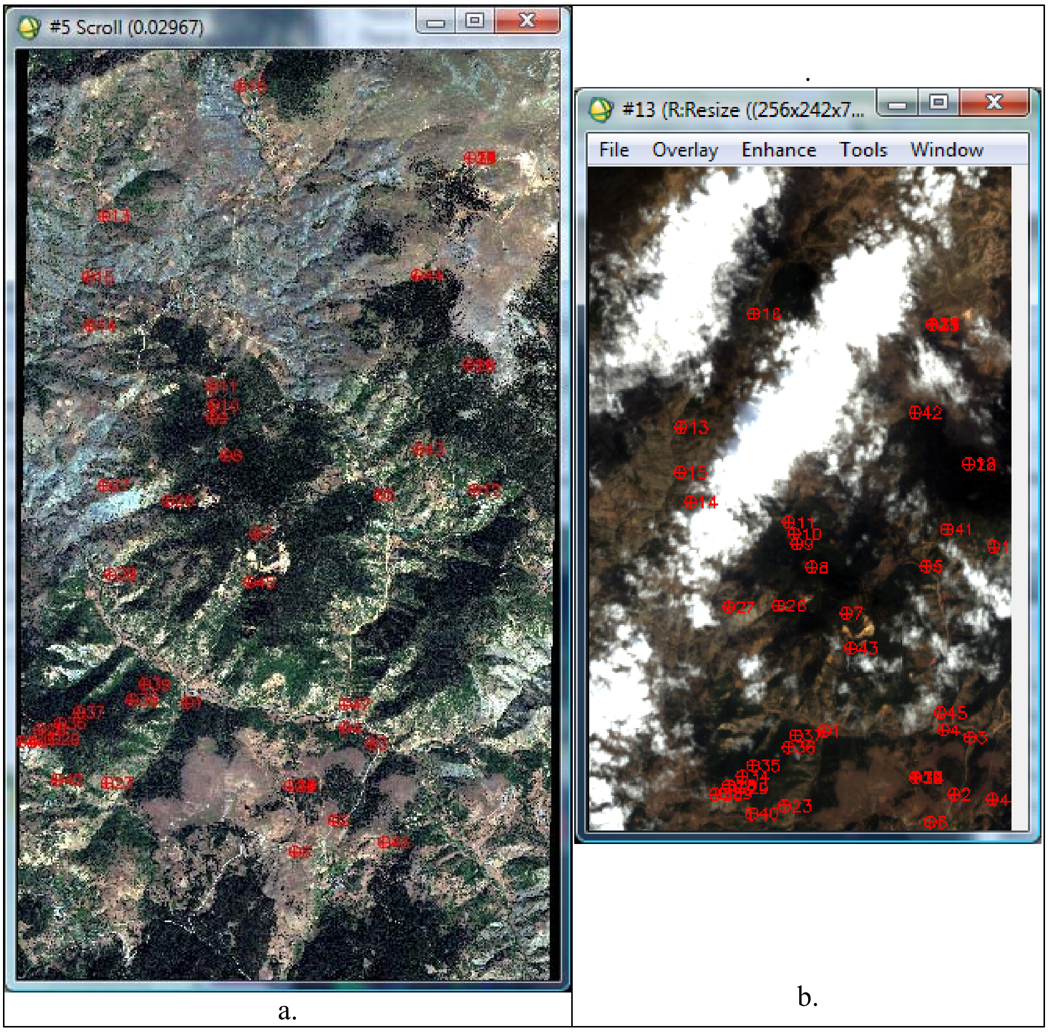

a.

b.

Figure 4.16 Ground control points selected (47) for image-image registration on a. Quickbird and b. Hyperion.

4.5 Analysis

4.5.1 Feature Selection

Identification of clay and iron oxide minerals is the main interest of this study. However, these two mineral groups can be best determined in different portions of the electromagnetic spectrum. Therefore it is decided to focus on the different parts of the spectrum for the identification of two groups of endmembers.

For the identification of clay endmembers SWIR portion of the dataset is used to process with eliminating the atmospheric absorption corridor between wavelengths 1100 nm and 2002 nm (Figure 4.17). Total number of bands used in this section for clay minerals is 49.

For iron analysis, on the other hand, VNIR portion between 400 nm to 1100 nm is used separately. It should be noted that uncalibrated bands are removed in the dataset shown in Figure 4.17. Total number of bands used for this group is 33.

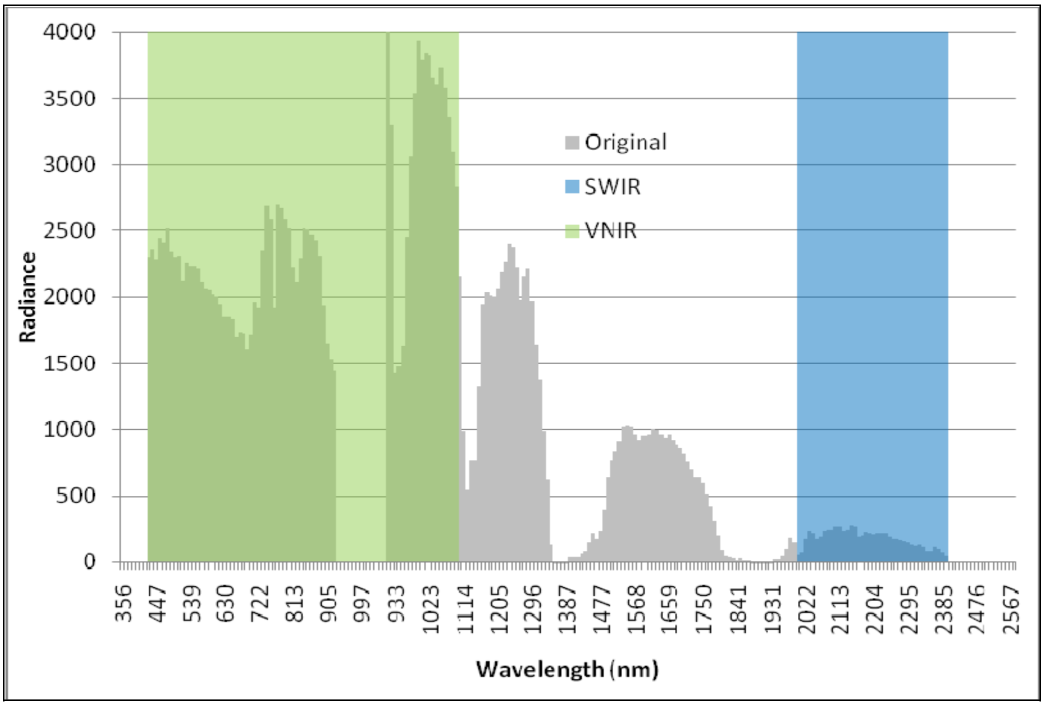

Figure 4.17 Spectral ranges used for the rest of the study.

4.5.2 Endmember Identification

The analyses are based on creation of training data sets from the image called the endmembers. Identification of endmembers is the most important step of the analysis because the identity and the number of endmembers will determine the outcome of this study. The endmembers preferably should be identified by the image itself that is to be analyzed. In this study a combination of field measurements, literature and image itself is used for final endmember identification. The selection criteria for the endmembers are their spectral significance and abundance.

The alteration types and mineral zoning is systematically explained in Lowell and Guilbert (1970). Geological map of the study area by Chadwick (2005) provided a good understanding of the high sulfidation porphyry system and the related alteration products. The field data and the geology are combined to obtain a first set of endmembers.

Pima and ASD surveys carried out in the study area (Figure 4.18) are analyzed according to the abundances of the minerals identified (Table 4.4). Identified minerals are selected with significant spectral properties (Figure 4.19) from the image. For the analyses the ASD survey results are used as spectral library data.

Table 4.4 Field spectrometer survey summary.

Mineral	**ASD Set**	**Pima Set 1**	**Pima Set 2**
Epidote	1	-	-
Montmorillonite	9	1	-
Topaz	14	3	-
Alunite	131	48	159
Pyrophyllite	20	7	7
Halloysite	21	-	-
Muscovite	22	12	-
Kaolinite	27	22	309
Dickite	82	28	95
Silica	106	19	-
Illite	133	14	9
Jarosite	-	1	-
Grand Total	**566**	**155**	**579**

Epidote-Chlorite: Epidote is detected only in one ASD spectral measurement data and not identified in the image. Chlorite is also not observed in the image data. Therefore they are not considered as an endmember.

Montmorillonite: Although it is read in only in nine samples, montmorillonite is found identifiable by the image and selected.

Topaz-Silica: Having a high hit number in ASD survey, silica and topaz; with relatively flat spectral graph found very hard to identify in the image. Not selected as an endmember.

Alunite: Field survey and the mapping, identified alunite and it is found abundantly in the image and selected as an endmember.

Pyrophyllite: Couldn’t be identified accurately from the image and discarded.

Muscovite: Being an important alteration product as sericite, couldn’t be identified conveniently from the image data.

Kaolinite-Dickite-Halloysite: Having the same chemical formula these minerals are distinguishable from spectral survey data and from the image. Thus, they are selected as endmembers.

Illite: Taking the most hit from the spectral survey illite is observed abundantly in the image and selected as an endmember.

Jarosite-Hematite-Goethite: Parallel with the field mapping ironoxide is deposited in different forms as alteration product. Although the spectral survey did not concentrate on iron oxide discrimination image data used to obtain these endmembers.

Therefore nine endmembers are selected for further analyses are kaolinite, dickite, halloysite, alunite, illite, montmorillonite, goethite, hematite and jarosite.

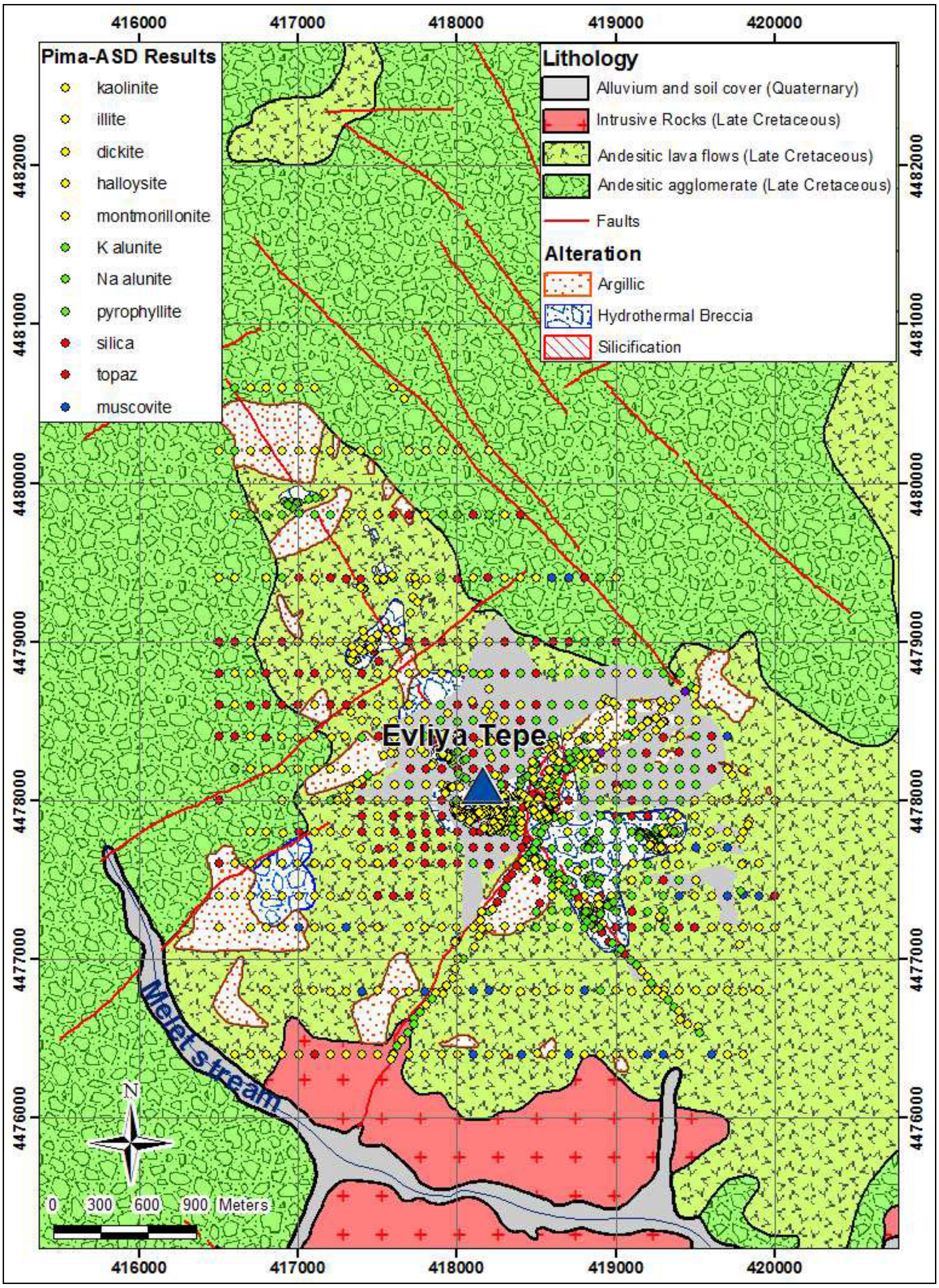

Figure 4.18 Field spectrometer survey.

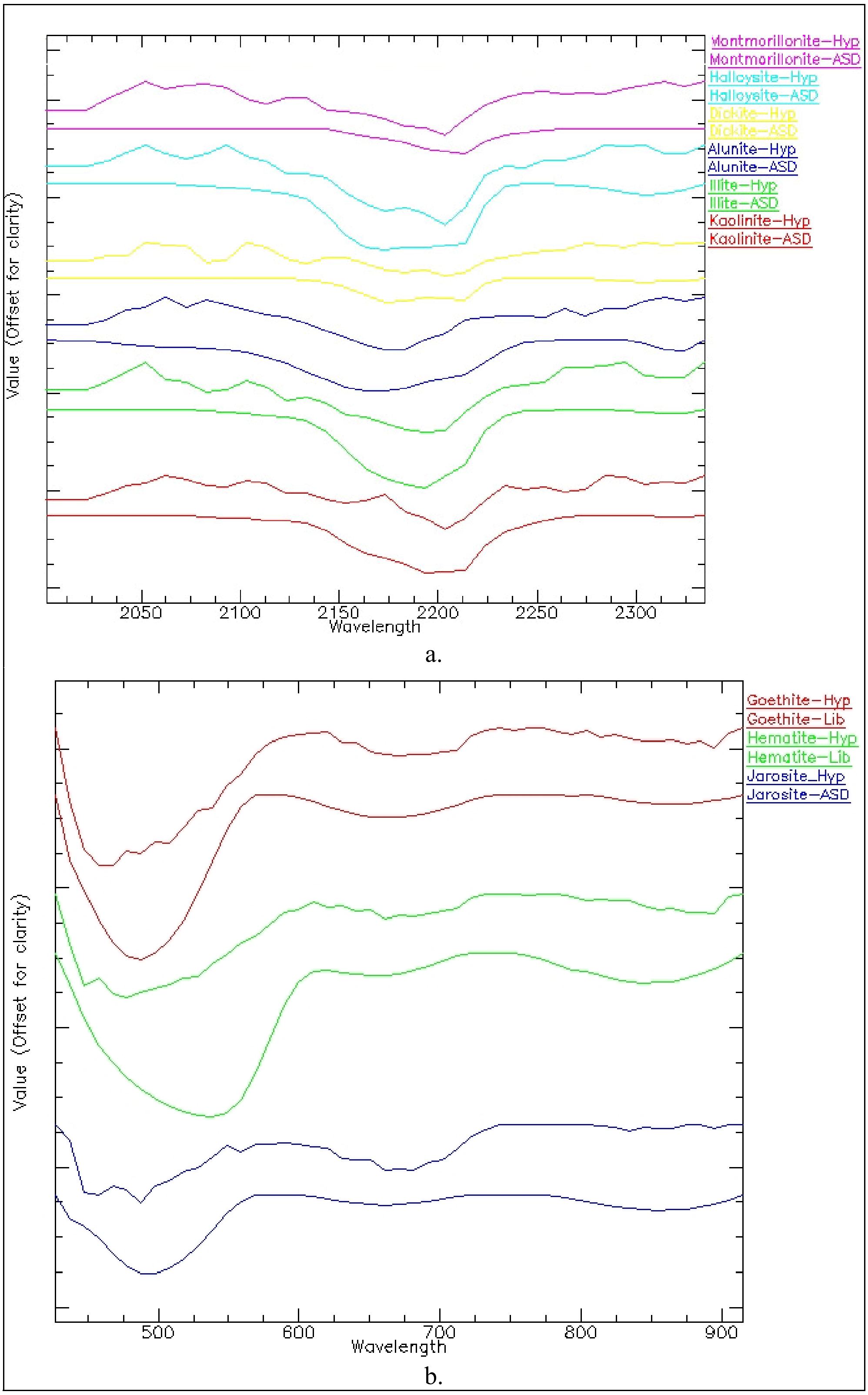

Figure 4.19 Selected endmembers and reference ASD library data overlaid for a. VNIR and b. SWIR regions (wavelengths in nm).

4.5.3 Unmixing

Three methods are tested for unmixing the image data according to the endmembers selected in the previous section. These methods are Linear Spectral Unmixing (LSU), Matched Filtering (MF) and Mixture Tuned Matched Filtering (MTMF). Results are displayed in Figures 4.20 through 4.22 respectively. All the results are rescaled between 0 and 1 and displayed as kaolinite, dickite and halloysite in respective RGB channels. In all images darker pixels depict the low tendency in representing the endmember. On the contrary, bright pixels are the result of a better match between endmembers and the image data. Here only kaolinite, dickite and halloysite endmembers are used for comparison plots.

4.5.3.1 Linear Spectral Unmixing

LSU is the simplest method and it uses the data itself without any transformations to perform linear unmixing and gives a very noisy output where stripes are mapped as endmembers (Figure 4.20). Large areas on the northwest are misidentified as argillic alteration which makes this method very unreliable with this data and the study area.

4.5.3.2 Matched Filtering

MF introduces the use of Minimum Noise Fraction (MNF) transformation in unmixing. Input bands are transformed to MNF space with the endmember spectra and matching scores are averaged for all bands. Use of MNF enhances the output by discriminating noise from the data. Better matching is represented by brighter pixels on the main alteration zones but still stripes and misidentifications are present (Figure 4.21).

4.5.3.3 Mixture Tuned Matched Filtering

MTMF brings enhancements to the MF unmixing method by introducing extra band and filtering option. In MTMF, besides the MF scores, infeasibility scores are used additionally. Input data should be an MNF output and by analyzing the MNF bands, noise free bands can be selected. First four MNF bands are used for this step.

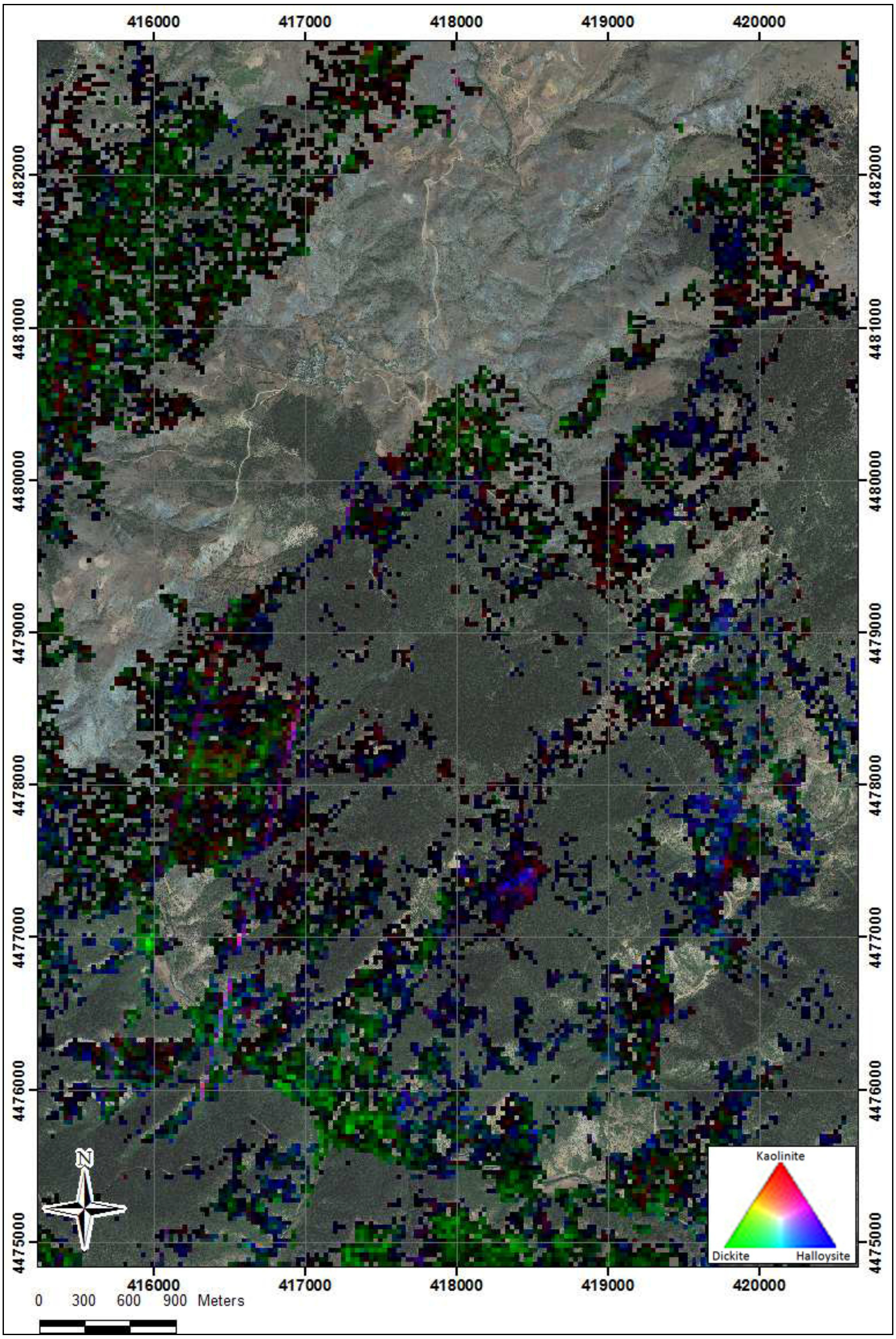

Figure 4.20 Linear Spectral Unmixing (LSU) result.

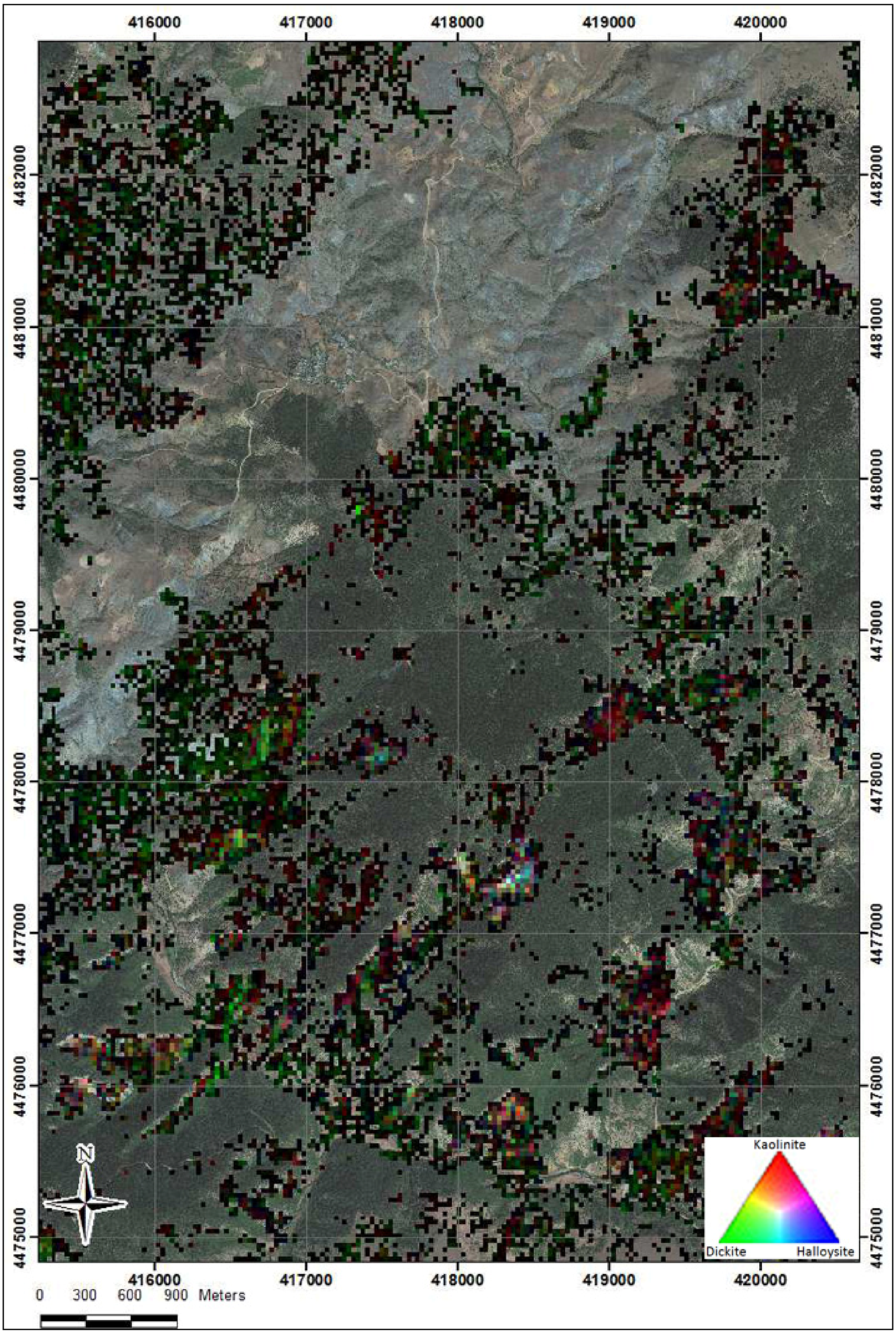

Figure 4.21 Matched Filtering (MF) result.

2D scatter graphs are used to mask out pixels with low match scores and high infeasibility scores. As a result, most of the sensor related stripes and misidentifications mapped by previous methods are eliminated by MTMF. In Figure 4.22 whiter response at the main zones indicate high matching for argillic endmembers as a mixture. The resultant MTMF bands are displayed in Figure 4.23.

The results of the methods are given in the previous section and the image statistics are used for a better comparison of the ability of unmixing.

For comparing the unmixing outputs, the known alteration zones are used where ground control is available by means of mapping and spectrometry (Figure 4.24). Three methods are tested in the same area represented by a polygon (200 pixels) which is located within a known alteration zone. This zone is identified as argillic alteration with a little oxidation by field data.

The results of the three methods in this polygon are tabulated in Table 4.5. For all methods, the results are given in two columns. These are the number of pixels equal to or greater than 95 % confidence level and the DN values at the 95 % confidence level. DN numbers are rescaled to 0-255.

The number of pixels is approximately the same denoting that all the methods are identifying same number of pixels with varying accuracies.

The values in DN columns, however, show a systematic increase towards MTMF except for VNIR endmembers. In the SWIR region, the average DN values for the methods are 151, 167 and 192 for LSU, MF and MTMF respectively (Figure 4.25a). This will result in brighter pixels in MTMF output.

In VNIR region, the average DN values for LSU, MF and MTMF are 144, 184 and 162. The selected test area is characterized by argillic alteration. Therefore, the expected trend for iron oxides is a systematic decrease towards MTMF. However, LSU values do not follow the trend (Figure 4.25b). This might be explained by the consistent noise that is observed visually in the outputs. Excluding the LSU, systematic decrease from MF to MTMF is observed. For VNIR endmembers, MTMF displays the darker pixels. Both trends are shown in Figure 4.25.

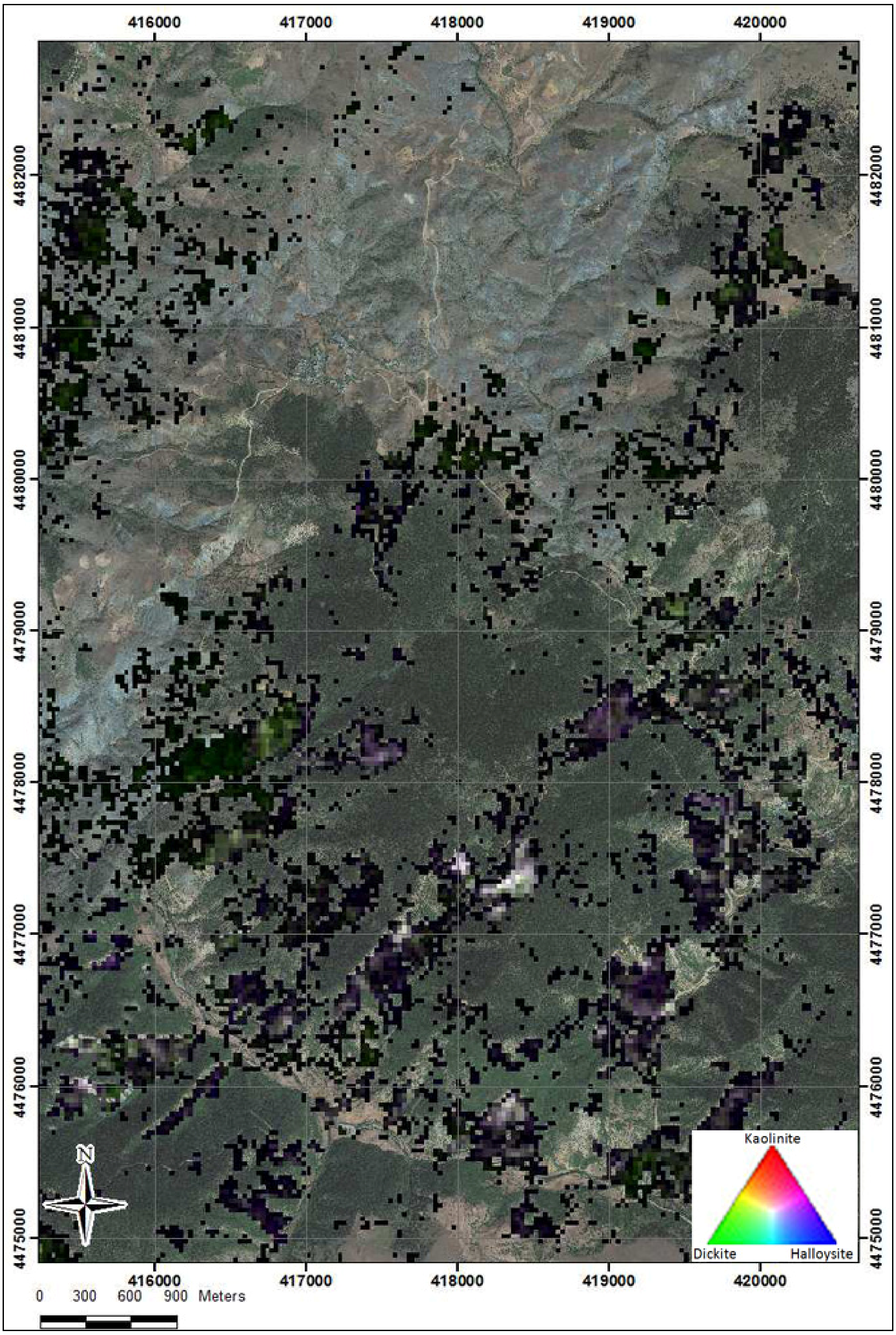

Figure 4.22 Mixture Tuned Matched Filtering (MTMF) result.

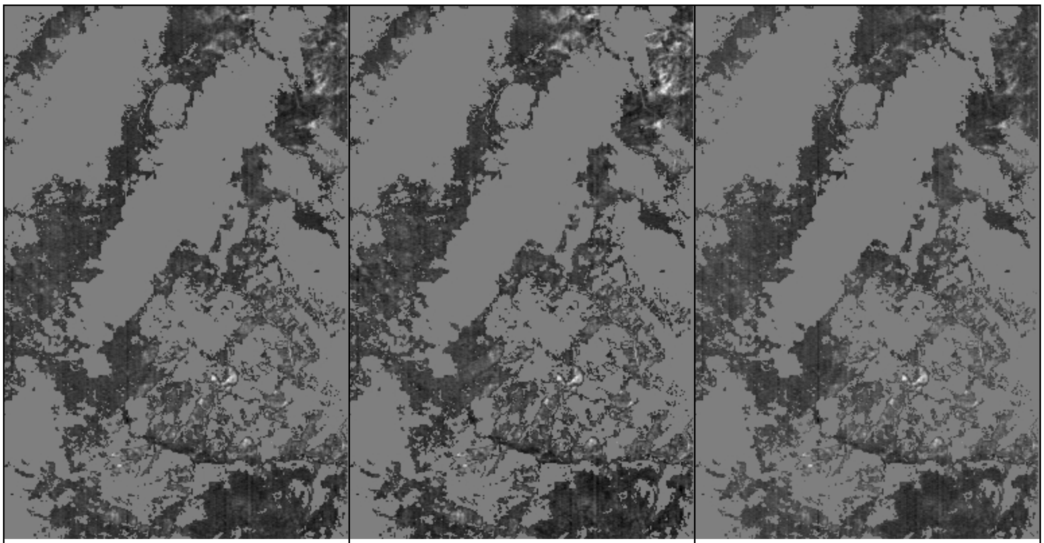

Kaolinite Dickite Halloysite

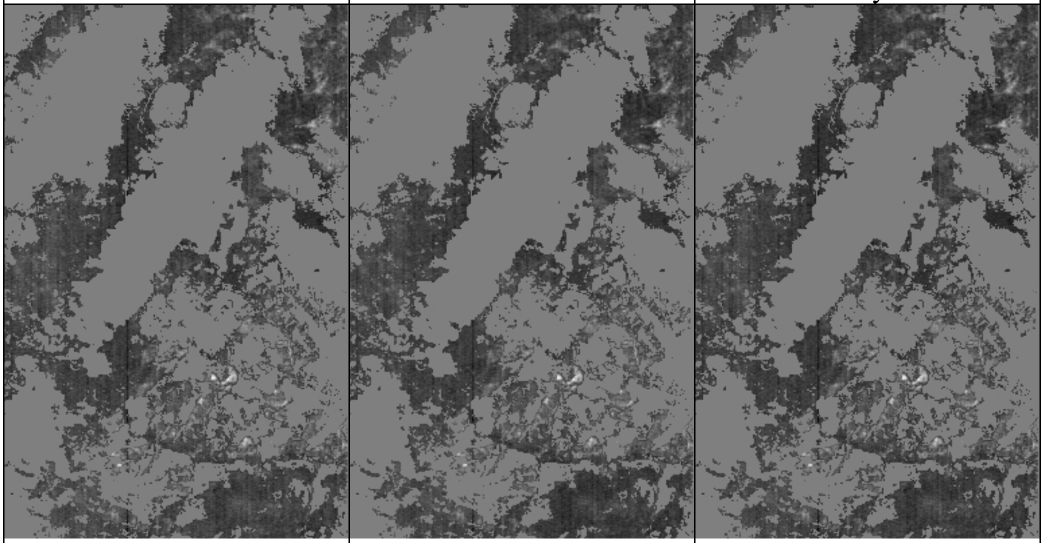

Alunite Illite Montmorillonite

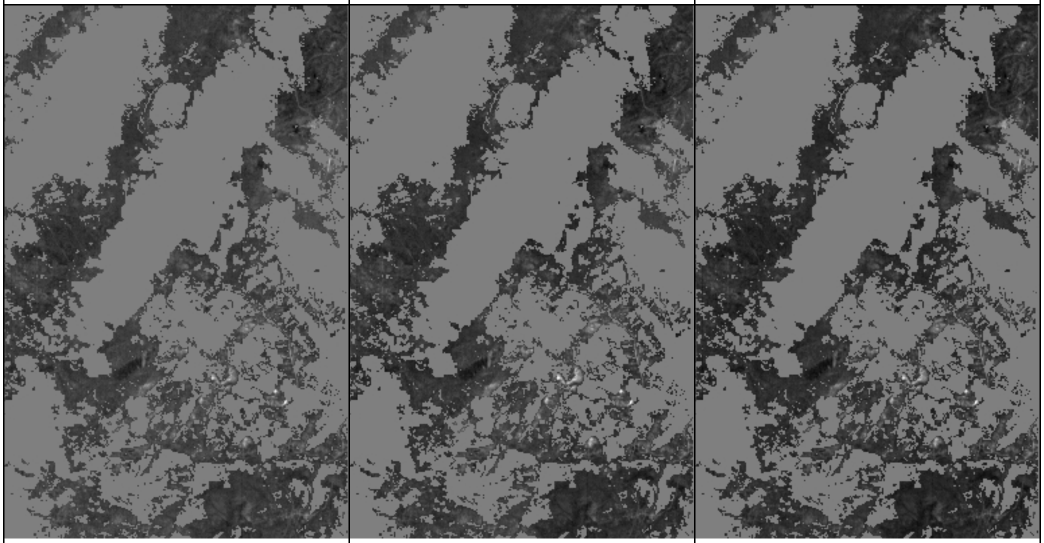

Hematite Goethite Jarosite

Figure 4.23 MTMF results for endmember comparison of unmixing techniques

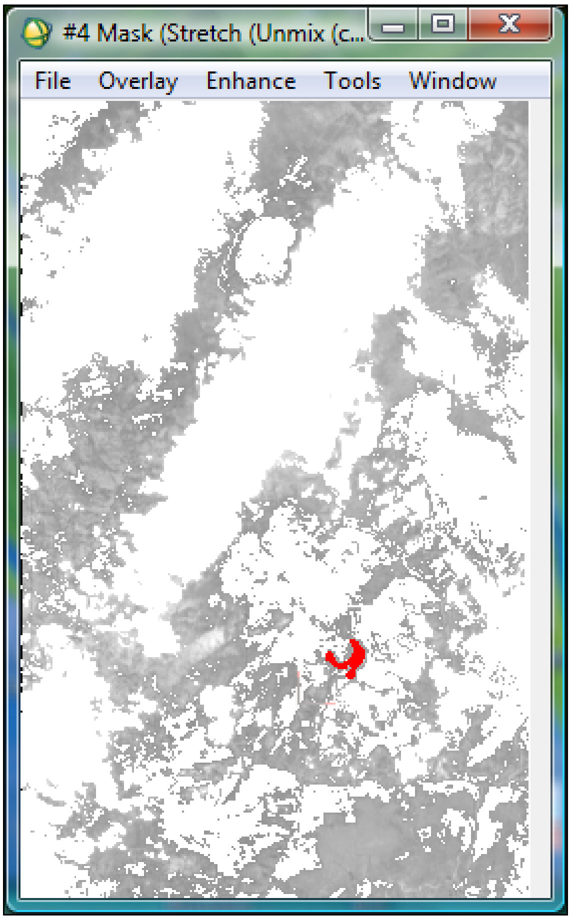

Figure 4.24 The subset used to assess the unmixing results is shown in red polygon.

Table 4.5 Statistical comparison of the unmixing methods.

Endmembers		**Number of Pixels >= 95 % Confidence**			**DN Value at 95 % Confidence**		
		LSU	**MF**	**MTMF**	**LSU**	**MF**	**MTMF**
Clays	Kaolinite	19	20	19	157	174	192
	Dickite	18	20	18	134	183	189
	Halloysite	20	20	20	184	145	194
	Alunite	17	19	18	101	170	192
	Illite	20	18	18	149	155	194
	Montmorillonite	20	18	20	181	174	191
Iron Oxides	Hematite	20	20	19	210	189	152
	Goethite	16	20	20	92	185	176
	Jarosite	19	20	20	131	177	159

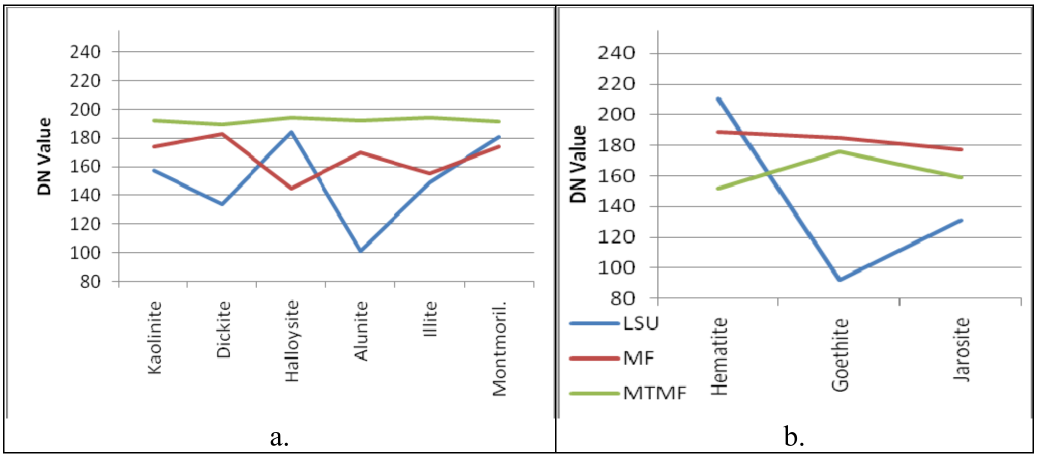

Figure 4.25 Graphical comparison of three methods used to unmix the a. clay minerals b. iron oxide endmembers.

MTMF is thus selected to be the best unmixing method. Therefore the classification in the next section included the enhanced endmembers selected by MTMF output.

4.5.4 Classification

The standard classification procedure involves the use of conventional methods like Binary Encoding (BE), Spectral Information Divergence (SID) and Spectral Angle Mapper (SAM) by means of spectral fitting algorithms. Additionally, unmixing techniques can be applied where there is high spatial and spectral resolution with adequate ground control. The Hyperion dataset has high spectral and low spatial resolution combined with low SNR values. Therefore, an integrated approach combining the unmixing and classification is developed and tested for this study.

In order to obtain the final alteration map by using the results of the MTMF, selected endmembers are validated and updated by using the matched scores and infeasibility scores comparatively. An example of this graph displaying the matched scores and the infeasibility scores is shown. In two dimensional scatter graphs, pixels having high matching scores (>0.5) and low infeasibility scores (<0.25) are selected and the image endmembers are updated accordingly (Figure 4.26).

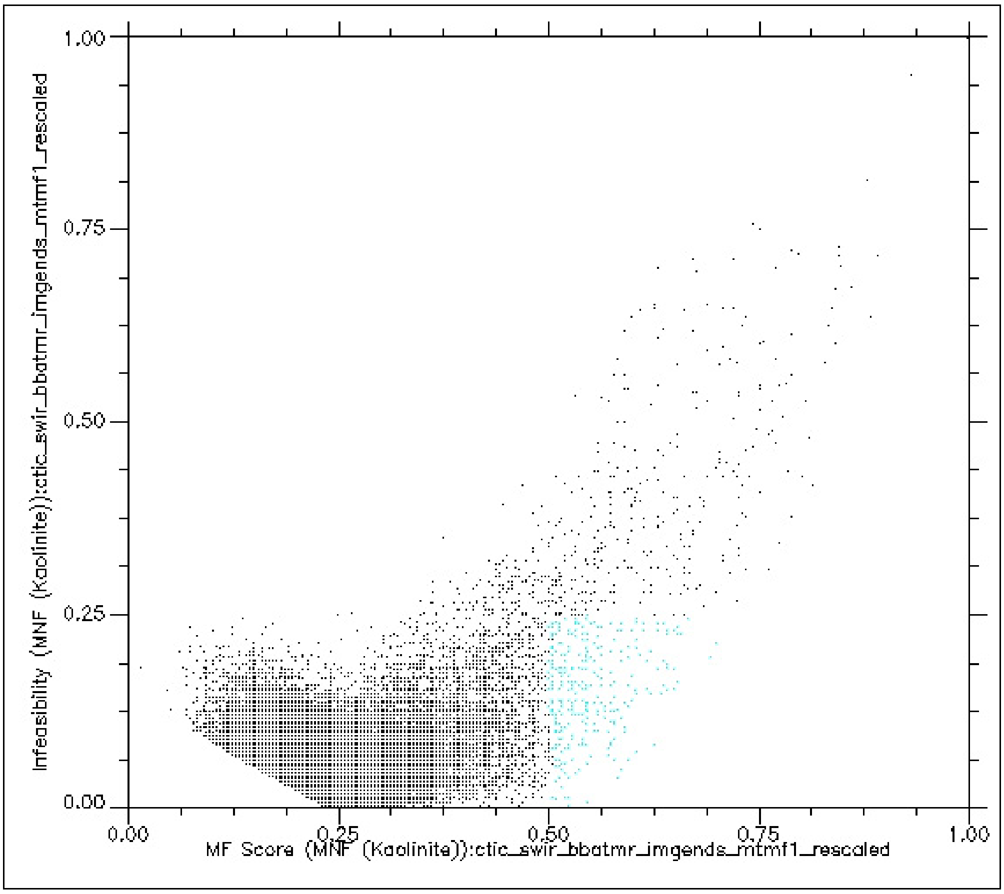

Figure 4.26 2D Scatter graph of matched score vs. infeasibility for MTMF Kaolinite output.

In Figures 4.27 and 4.28 the scatter graphs of the nine endmembers are given. The scatter graphs of SWIR and VNIR endmembers also show a correlation. The similarity between the pairs like kaolinite-dickite and illite-montmorillonite for the SWIR and hematite-goethite for the VNIR is observed. This correlation is a good indication of the coexistence of mineral pairs that are found in the same image pixel as a mixture.

Spectral Correlation Mapper (SCM) is used for the final classification of the updated endmembers. The algorithm is prepared in ENVI language and implemented to the software (Coulter, 2006). Pixels having correlation higher than 0.9 (out of 1) are selected and contrast stretched (Figure 4.29). The resultant map shows an abundant association of the endmembers identified. The evaluation of the classification result is discussed in the next chapter.

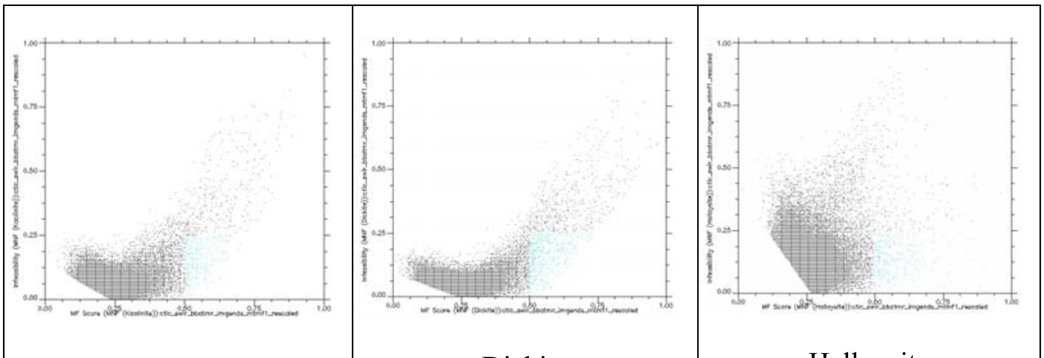

Kaolinite Dickite Halloysite

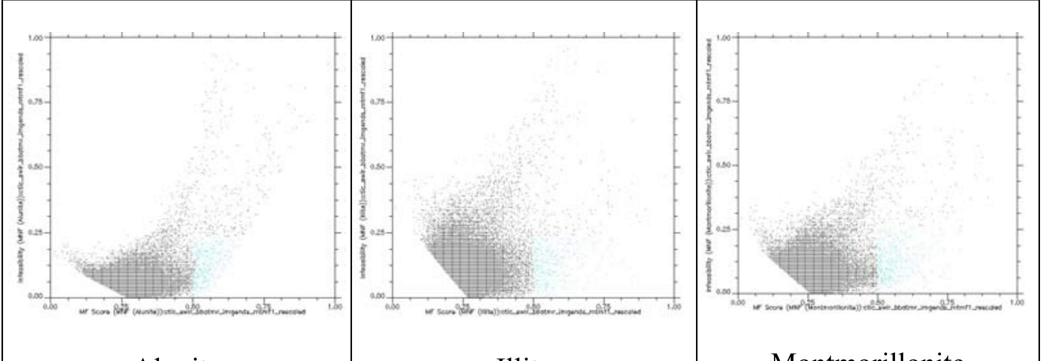

Alunite Illite Montmorillonite

Figure 4.27 2D Scatter graphs of MF Score vs. Infeasibility Score for SWIR endmembers

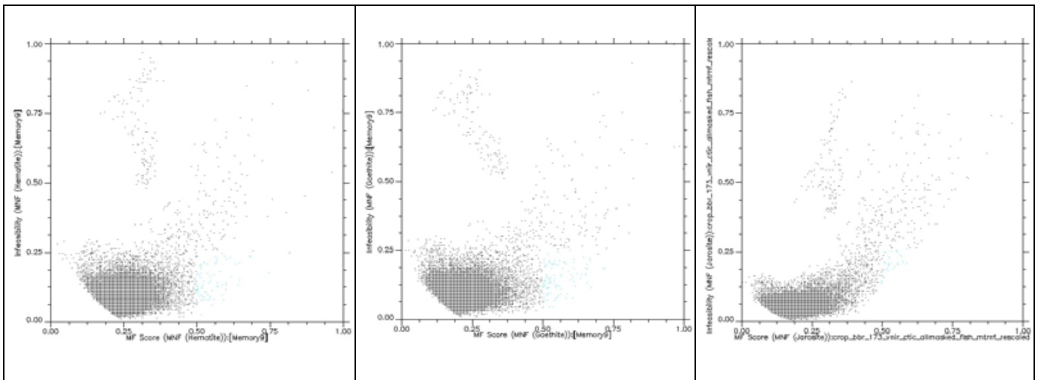

Hematite Goethite Jarosite

Figure 4.28 2D Scatter graphs of MF Score vs. Infeasibility Score for VNIR endmembers

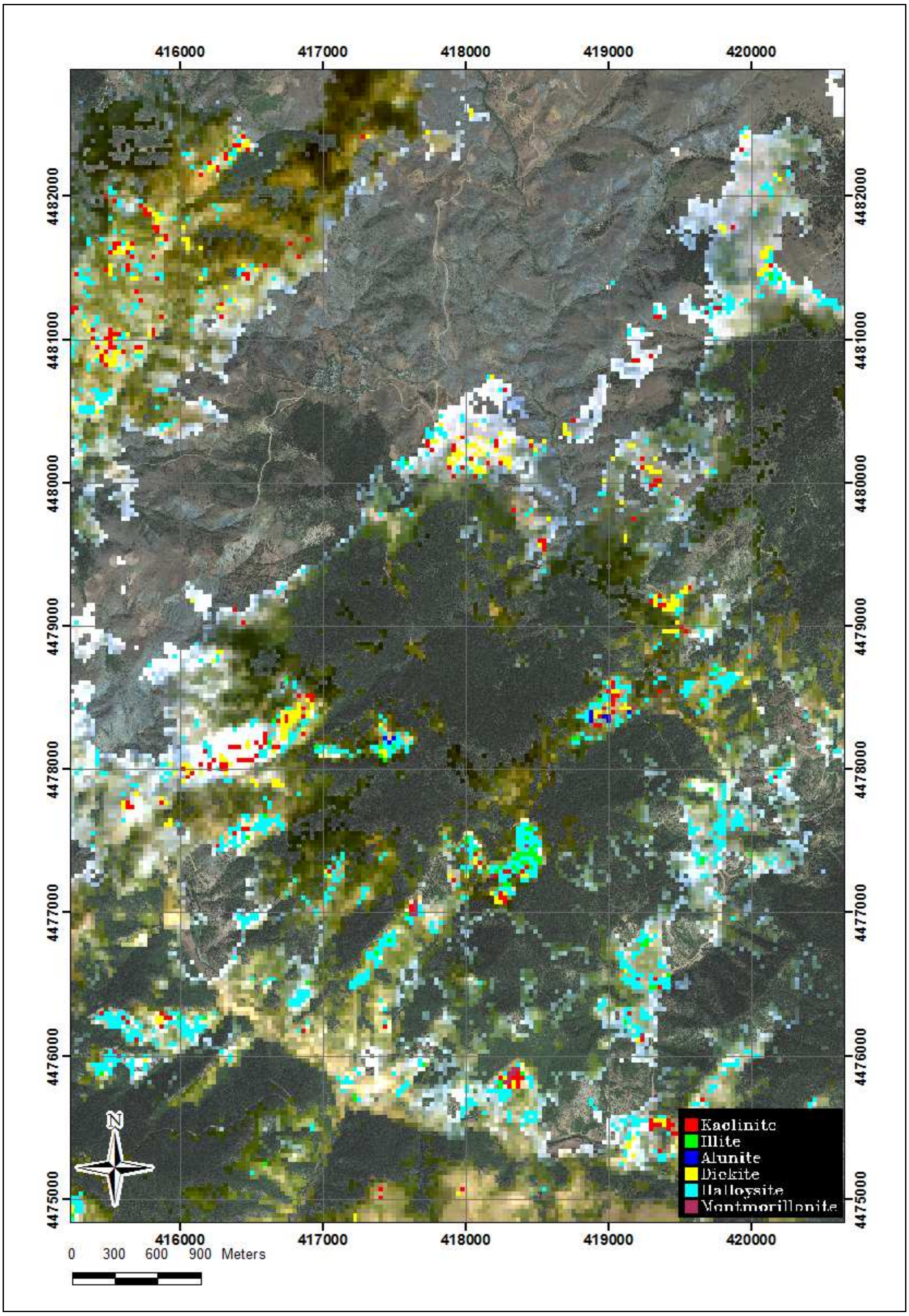

Figure 4.29 Highlighted classification result of argillic endmembers.

4.5.5 Accuracy Assessment

The validation of the whole process is performed in two phases. In the first phase, the spectral cross correlations are calculated for raw ASD survey data which is collected before and after the image analysis. VNIR and SWIR portions of the image data are cross correlated separately with the ASD readings and the correlations are recorded in this phase. In the second phase the assessment is performed spatially by using the identified minerals qualitatively on site by the ASD survey.

i. Phase 1

Being a part of the exploration program the ASD survey is carried out and 566 samples are collected. Location map of these samples are already shown in Figure 4.18. After the masking of image, 204 of these samples fall inside the processed image. Mean correlation coefficient for VNIR region is calculated as 0.78 and for SWIR as 0.47. This result is very identical to SNR values of the representing bands of these regions. Low SNR is the main reason for the lower correlation in the SWIR region.

After the initial process is completed, ten additional samples are collected from the selected sites to validate the process results (Figure 4.30). One sample falls to the masked area and therefore is discarded. Cross correlation results of these ASD spectrometer readings and the image data is given in Figure 4.31. The mean correlation coefficient for this phase of validation is 0.90 for VNIR and 0.69 for SWIR regions. The difference between two phases can be explained as survey defects like calibration errors, measurement errors, fresh surface readings and coordinate errors.

ii. Phase 2

Spatial correlation between the image derived endmembers and the ASD identified minerals is calculated in this phase. The minerals identified by spectrometric analysis are taken as the reference points, and the image pixels corresponding to these reference points are analyzed according to the clay endmembers. Table 4.6 shows the mean and minimum correlation values of the corresponding pixels for six clay endmembers. The numbers in bold show the

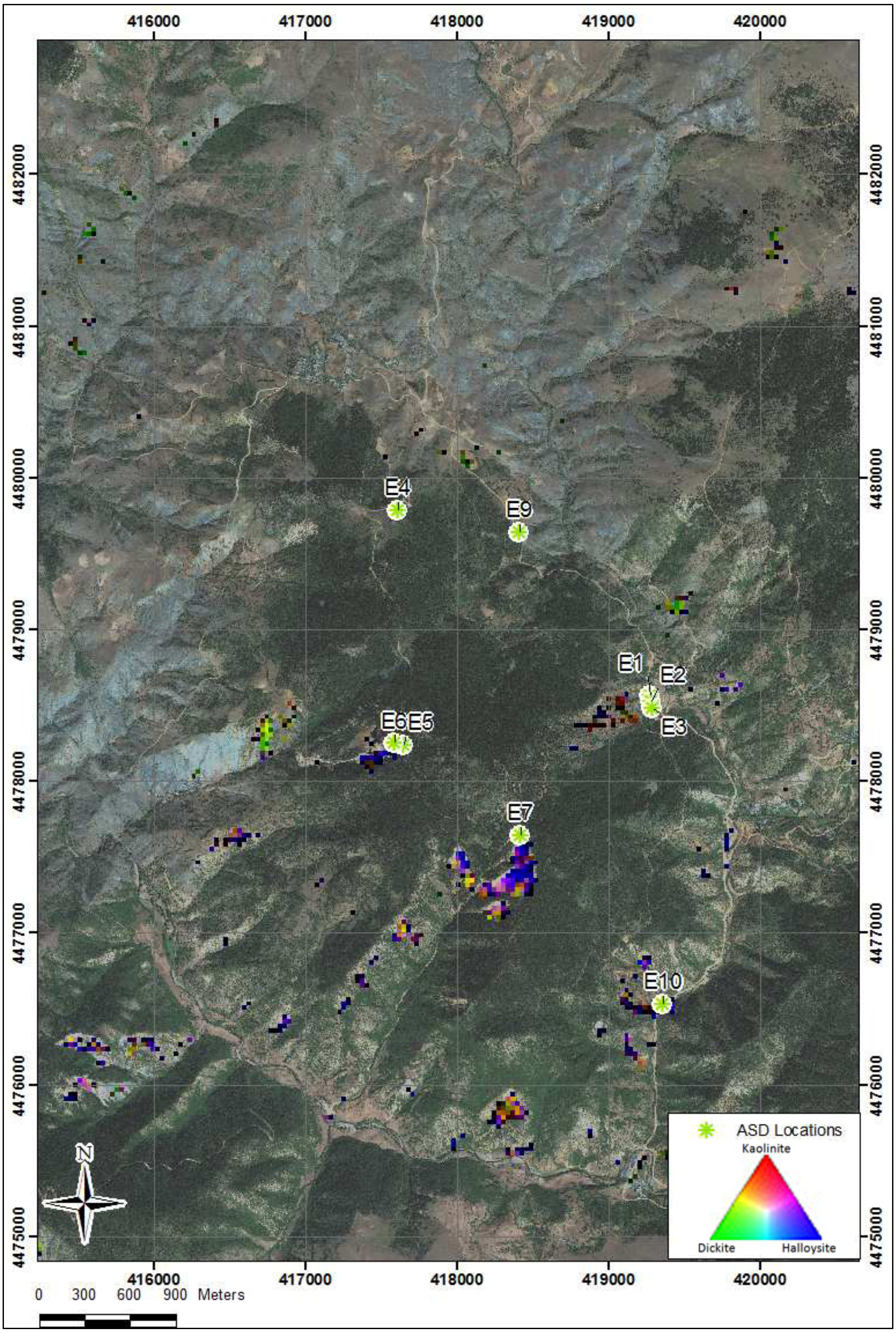

Figure 4.30 ASD survey sample locations for the second phase of validation.

correlation for the matching case which the reference points are mapped by the image. For the mean values the highest numbers around 0.80 in the diagonals belong to halloysite and illite minerals, where for the rest the correlation is around 0.60. Checking with the minimum values, halloysite gives the highest correlation with 0.73. The image data can discriminate halloysite with 80 % accuracy, highest of all. Illite is the second highest scored mineral that can be identified with approx. 80 % accuracy a minimum of 0.46. Dickite and kaolinite minerals have identical mean scores but the minimum of kaolinite is the lowest of all. Having the same chemical formulae dickite and kaolinite have different crystallography and can be discriminated with spectroscopy. The low signal quality for the image data actually creates the 60 % accuracy for kaolinite and dickite group of clay minerals. The lowest minimum correlation (0.18) is recorded for kaolinite. The absorption feature around 2200 nanometer is very similar with illite and the second order mineral identified by spectroscopy for illite is kaolinite. Mean correlation for montmorillonite is similar to kaolinite but with greater minimum value, indicating a higher accuracy than kaolinite. With the hydroxyl in the formulae, alunite is chemically different from the phyllosilicates group of clay minerals. Both alunite and dickite have absorption feature around 2180 nanometers and that is why the dickite is the second order mineral identified by the field spectrometer. Relatively low accuracy (56 %) for alunite is also another example of the scale problem between the image and spectrometer.

Spectrally and spatially the image data shows a certain coherence with the ground data also in the light of geological and alteration mapping. The next chapter interprets and discusses the results in this perspective.

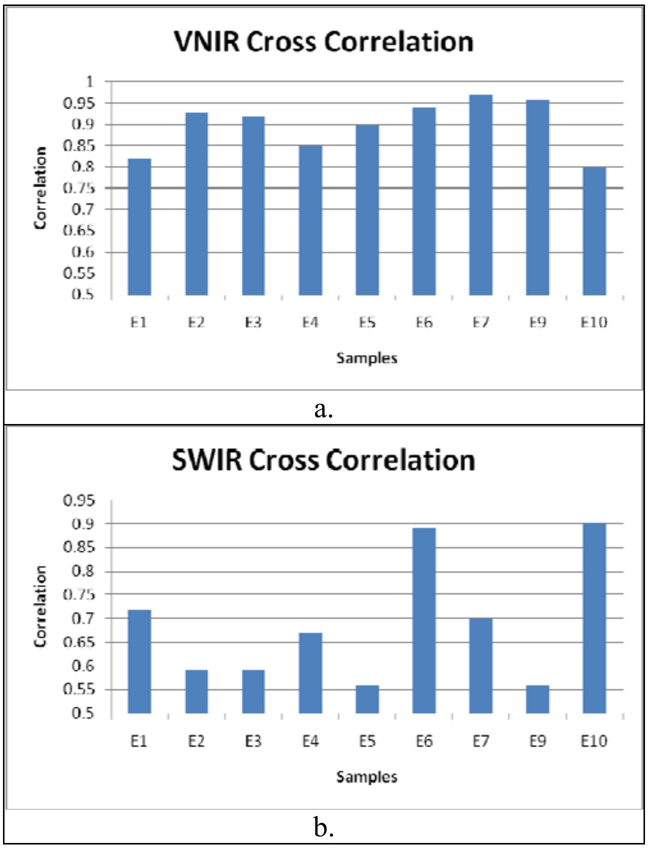

a.

b.

Figure 4.31 Spectral validation of image data with ASD for a. VNIR and b. SWIR regions.

Table 4.6 Mean and minimum correlation values of the coinciding ground points and image pixels for six clay endmembers.

Mean ASD/Hyperion	**Dickite**	**Halloysite**	**Illite**	**Alunite**	**Kaolinite**	**Montmorillonite**
Dickite	**0.63**	0.84	0.84	0.63	0.70	0.67
Halloysite	0.66	**0.83**	0.83	0.64	0.71	0.68
Illite	0.60	0.82	**0.81**	0.59	0.67	0.63
Alunite	0.56	0.80	0.80	**0.56**	0.63	0.59
Kaolinite	0.54	0.72	0.72	0.52	**0.59**	0.54
Montmorillonite	0.58	0.81	0.81	0.58	0.64	**0.61**
Minimum ASD/Hyperion	**Dickite**	**Halloysite**	**Illite**	**Alunite**	**Kaolinite**	**Montmorillonite**
Dickite	**0.49**	0.76	0.75	0.48	0.57	0.52
Halloysite	0.44	**0.73**	0.72	0.44	0.53	0.48
Illite	0.20	0.46	**0.46**	0.18	0.24	0.21
Alunite	0.41	0.66	0.65	**0.42**	0.49	0.42
Kaolinite	0.15	0.24	0.27	0.13	**0.18**	0.11
Montmorillonite	0.49	0.76	0.76	0.51	0.57	**0.53**
	Dickite	**Halloysite**	**Illite**	**Alunite**	**Kaolinite**	**Montmorillonite**
# of points	23	9	69	29	8	6

CHAPTER 5

DISCUSSION

5.1 Hyperion Data

Hyperspectral remote sensing techniques are evolving with the introduction of new technologies in the area. As the airborne hyperspectral sensors are easy to deploy and test, improved routines are developed faster than the research in satellite based systems.

Hyperion is one of the first satellite borne hyperspectral sensor and it has acted as a frontier system from sensor design to signal processing issues. With the success of multispectral and high resolution satellite missions, the idea to combine the spectral resolution capabilities of airborne systems and the low cost high profitable satellite missions led the development of space borne hyperspectral missions.

Hyperion was the result of this idea and was a testing board after all. Experimental mission brought its own amenities and drawbacks together. The spectral resolution at the first sight had to be cropped with the poor signal quality. Although, standard radiometric correction at sensor routines are developing day by day the delivered data still includes atmospheric and sensor related artifacts.

The Hyperion imaging system is known to have sensor specific errors (Christian and Krishnayya, 2007). Therefore, to be able to use the data properly and to create valid results, certain corrections have to be applied. Some of the errors can be corrected by applying the methods explained in the previous chapter. The applications applied in this study are radiometric correction, CTIC and cloud-shadow masking. With the consistent noise in certain bands, instead of correction, removal is applied. Uncalibrated and noisy bands are therefore removed. Total number of bands after removal is reduced from 242 to 173.

During the planning of data gathering, seasonal conditions are considered. However, the geographical location of the study area, with the surrounding high topographic relief makes the cloud coverage unpredictable. New processing steps are introduced due to considerable amount of cloud covering the study area in the image. Cloud covered pixels are not usable for the analysis; therefore, those pixels are removed by masking.

Clouds inevitably create another source of error in the form of shadow. With the current studies shadow can be corrected by signal processing techniques (Oo, 2007) but this subject is another research topic which is beyond the scope of this study. Therefore shadow is not corrected but removed by masking. Excluding these types of errors from the image reduces the total pixels that are going to be used in for further analysis.

On radiometric correction a number of atmospheric modeling techniques are available. Conventional Flat Field (FF) and Internal Average Radiance (IAR) methods are not used as it is not meaningful to search for spectrally flat areas with a noisy image data. Commercial models like Atmospheric Correction Now (ACORN) and Atmospheric Correction (ATCOR) are tested in previous studies (San, 2008). Selection of the model is based on the availability for this study therefore FLAASH model in ENVI is used.

Illumination variation across the tracking direction is a sensor specific error but it shows variance between different image datasets (Pearlman et al., 2003).To decide on the method and the order of removal of this variation, several attempts are made by trial and error. Third order additional model is selected to remove this effect for this dataset, but this might be different for other image sets.

5.2 Analysis

Three major analysis carried out in this study are endmember identification, unmixing and classification.

In the selection of endmembers a special attention should be given. With the availability of large number of ground control data unique and available endmembers selected specifically for alteration identification.

Unmixing techniques are applied usually to image data with high spectral and spatial resolution. Hyperion dataset satisfies the spectral resolution criteria with its 196 calibrated bands. But with its low signal quality and spatial resolution it is not a perfect match to apply unmixing procedures for mineral identification. While comparing the techniques from simple (LSU) to complex (MTMF) it is obvious that, for Hyperion image the unmixing procedure cannot be finalized with linear approach. For MTMF, selection of MNF bands is the key step for enhancing the results. Use of infeasibility values together with matched scores is used to test and update the endmembers. The resultant unmixed image shows closeness of image spectra to the endmember spectra. Therefore pixels having brighter outputs show a mixture of the corresponding endmembers.

Because of the certain limiting factors related with the image specifications, unmixing is used to modify the endmembers and final classification is carried out by using Spectral Correlation Mapper (SCM). Other than BE, SAM and SID, SCM introduces negative correlation parameter in the output giving a more reliable classification result. Highly correlated pixels with values greater than 0.8 and 0.9 are selected for final classes to concentrate and evaluate the alteration minerals.

5.3 Evaluation of Results

With the methods explained in Chapter 3, alteration identification for Sisorta prospect is performed by using the corrected apparent reflectance Hyperion data. Alteration characterization through geology is approved by the field spectroscopic survey and the endmembers are selected according to their abundances in the image itself. For iron oxide analysis VNIR portion of the image spectrum is used and for the argillic group SWIR portion is used.

Finally, kaolinite, dickite and halloysite are used for argillic group; alunite, illite and montmorillonite are used for intermediate-advanced argillic group and goethite, hematite and jarosite are used for iron oxide group. Results are given and discussed for the highlighted sites in detail (Figure 5.1).

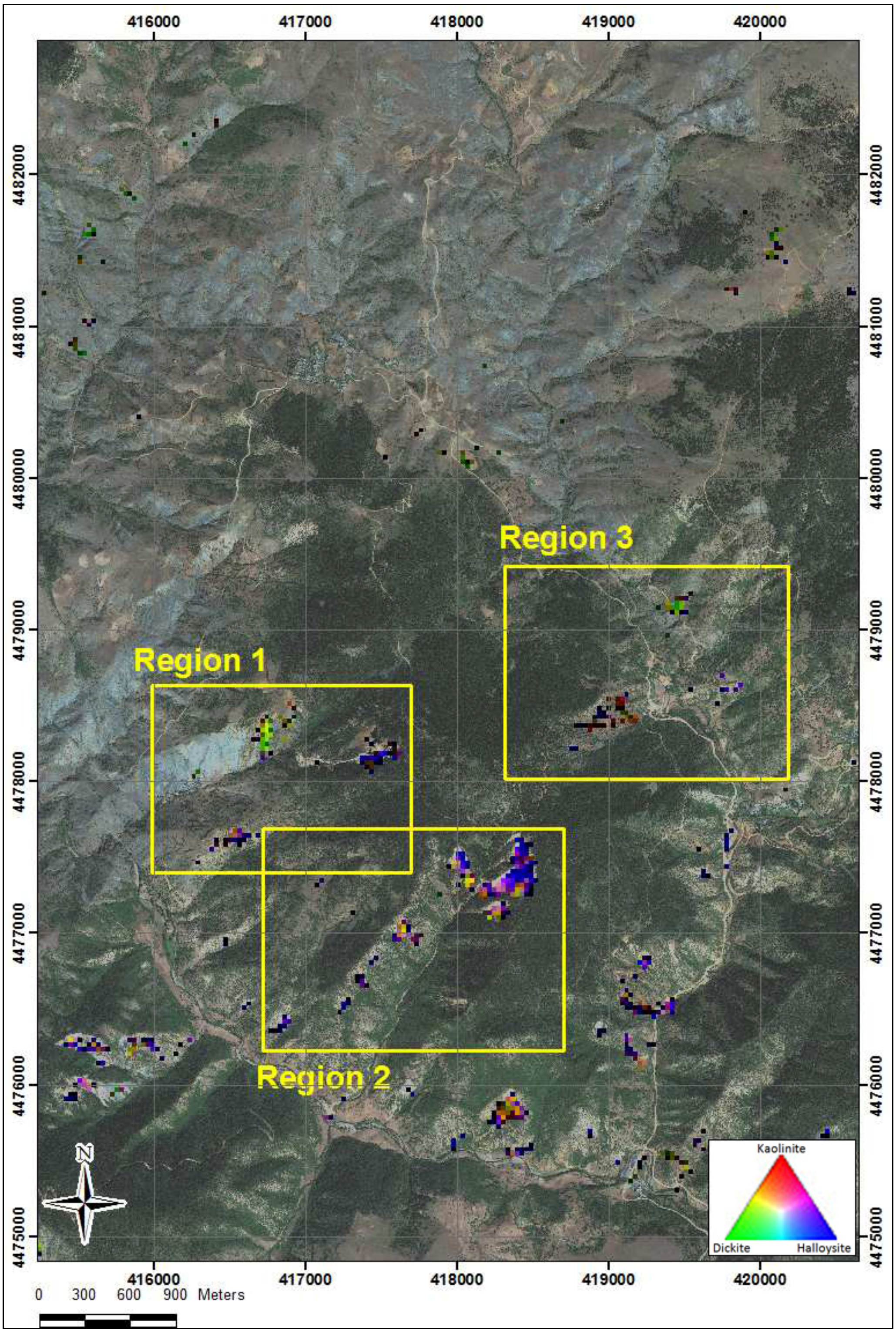

Figure 5.1 Location map for regions selected for detailed interpretation.

5.3.1 Argillic Group

Argillic alteration group of minerals are selected as kaolinite, dickite and halloysite.

The argillic group in region 1 is shown in Figure 5.2. There are three main responsive areas found in this area. The bright green to yellowish zone is denoted as “A”. Yellowish and greenish dominant correlation shows the high amount of dickite-kaolinite and relatively low halloysite.

The areas B and C include dark bluish colors reflecting low halloysite-kaolinite response.

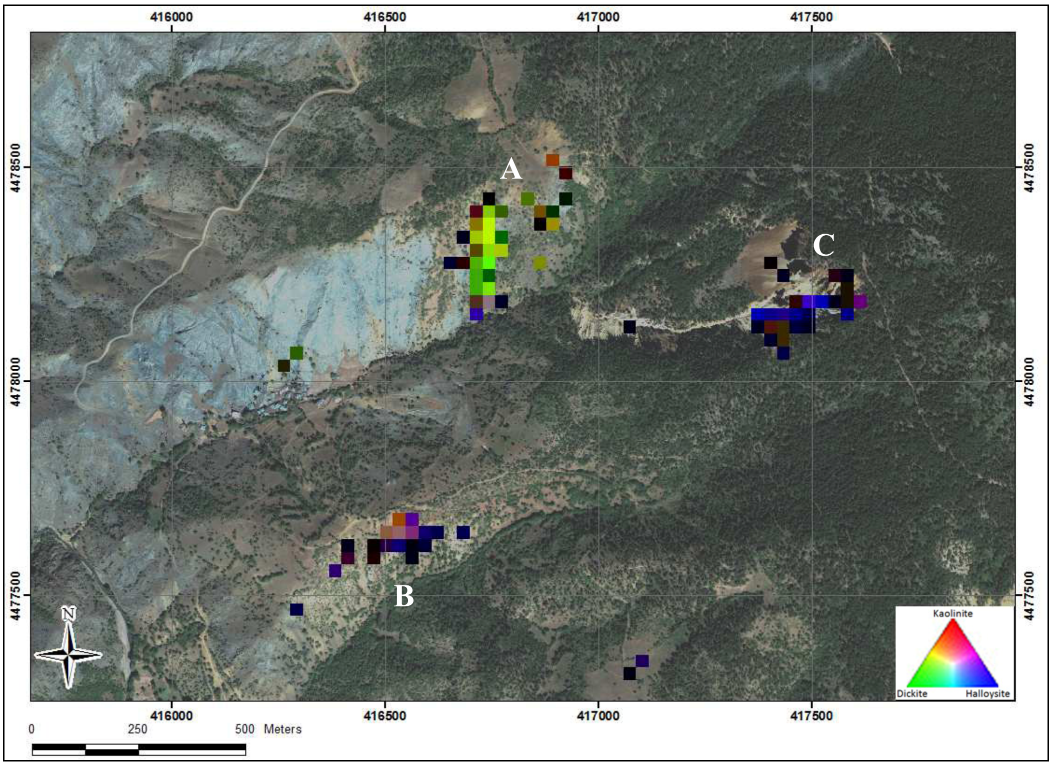

Figure 5.2 Region 1 Argillic group of mineral classes.

Region 2 includes the largest scale fault related scarp in the study area (Figure 5.3). This area dominantly includes blue pixels in varying tones with dark red and yellow patches. Also a gradual change from halloysite to kaolinite-dickite is observed in the main zone. This graduation can be related to the change in mixture composition due to high relief and accumulation in downslope direction.

Responsive pixels also show a linear alignment in the direction parallel with the valley and stream.

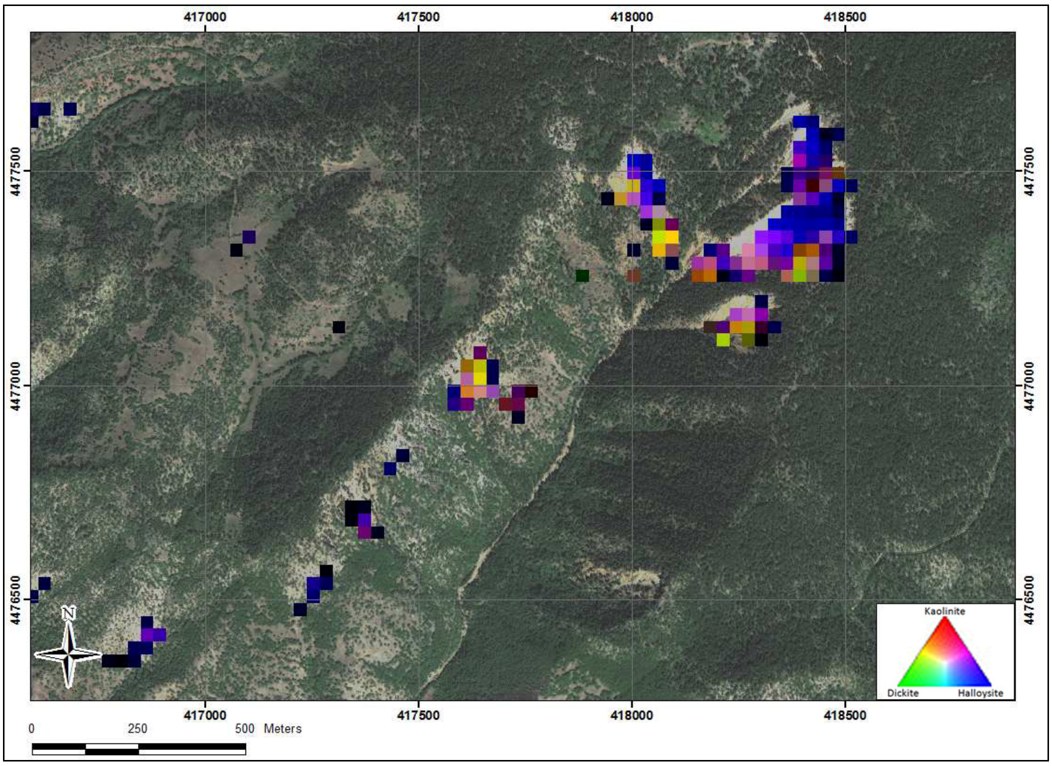

Figure 5.3 Region 2 Argillic group of mineral classes.

Relatively darker tones of red, green and blue are displayed in region 3 (Figure 5.4). In area denoted by “D” dark red and dark blue pixels reflect a low kaolinite and halloysite response. Area “E” is displaying a low response of Dickite. Pixels in areas A and B are relatively found as clusters. In area F, separate dark blue pixels are clustered denoting a low halloysite response.

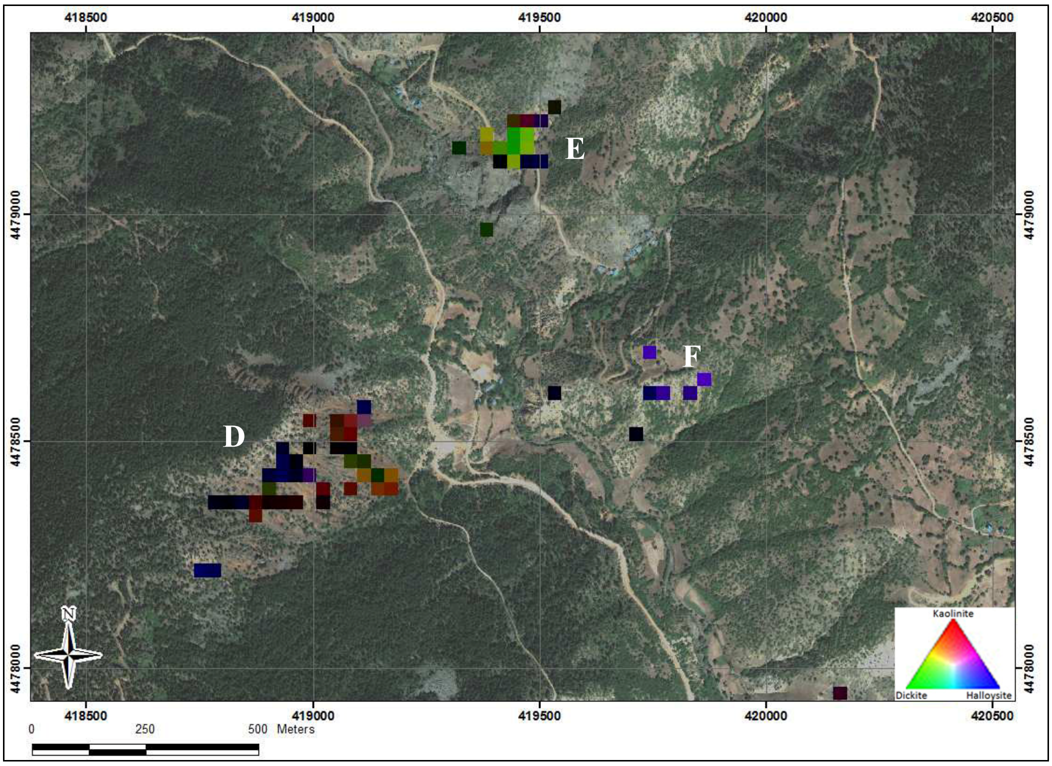

Figure 5.4 Region 3 Argillic group of mineral classes.

5.3.2 Advanced Argillic Group

The intermediate-advanced argillic group of minerals includes alunite, illite and montmorillonite.

The classification result for region 1 is characterized by small number of pixels with bright tones (Figure 5.5). In area A, blue montmorillonite pixels are observed together with a little response of alunite in neighboring pixels. In areas B and C illitic response is dominant. Small numbers of alunite pixels are mapped in area C. The illitic response shows a parallel alignment with the stream valley.

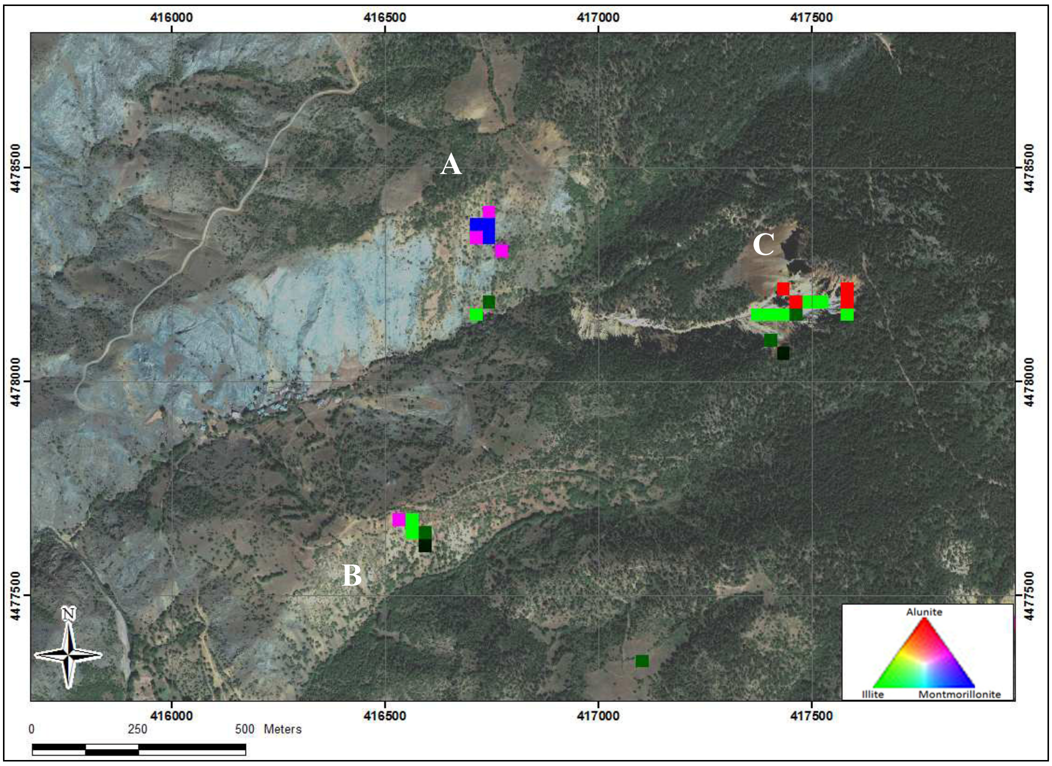

Figure 5.5 Region 1 Adv.-Int. Argillic group of mineral classes.

Very bright green pixels cover the main zone in region 2 depicting an illitic response (Figure 5.6). As it was the case in argillic group, a gradual change in down slope direction is also apparent in this region. Change from green to red and magenta again points the change in mixture constituents. The presence of white pixels is another indicator of the highly responsive mixture.

Region 3 is characterized by bright red to magenta pixels in area D and no response is mapped for the area E. Alunite is found as a cluster of pixels showing a similarity with the argillic group. Little response of Illite is mapped in area F (Figure 5.7).

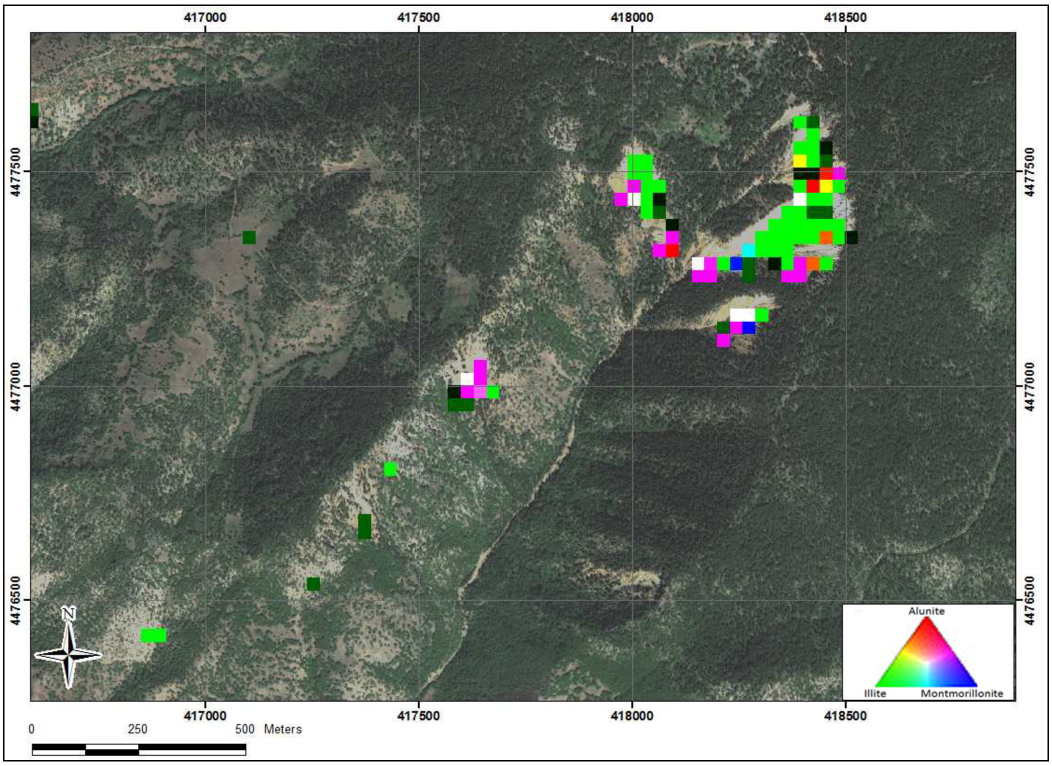

Figure 5.6 Region 2 Advanced-Intermediate Argillic group.

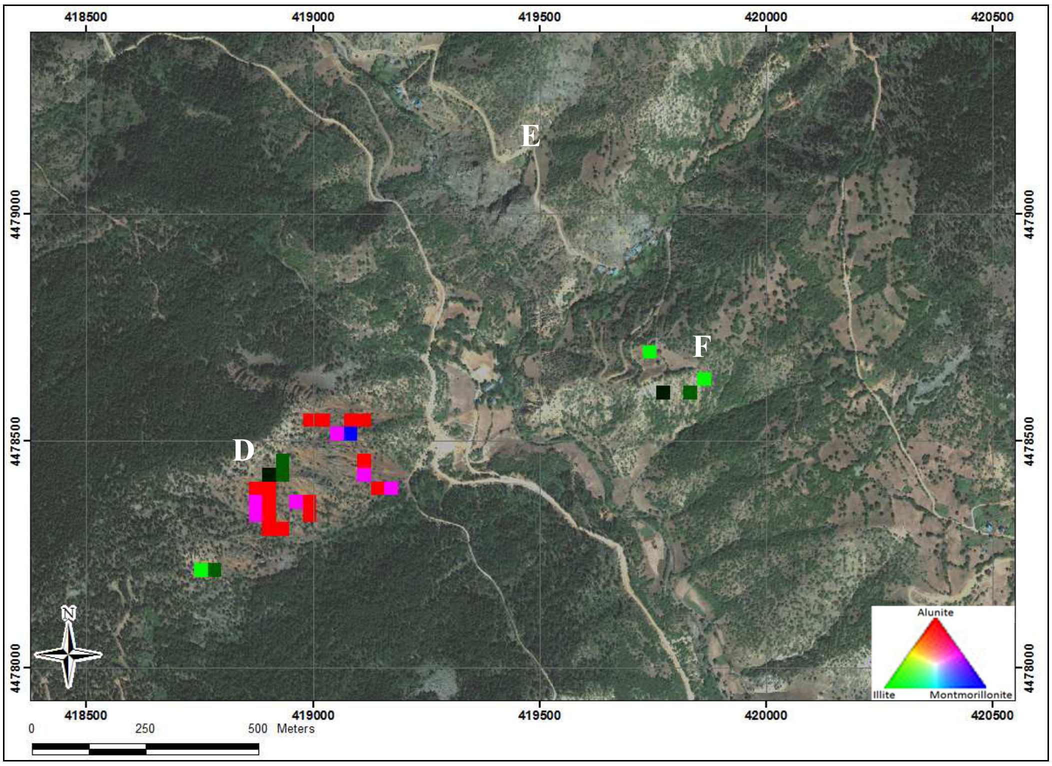

Figure 5.7 Region 3 Advanced-Intermediate Argillic group

5.3.3 Iron Oxide Group

Iron oxide group is formed from endmembers identified using the VNIR region of spectrum. These are goethite, hematite and jarosite.

In region 1 bright blue and yellow pixels are higher in number than the green pixels (Figure 5.8). Area A is classified with blue and dark green with a little yellow response. The map shows mainly jarosite and in decreasing order of hematite and goethite in the composition. However, a strong response of bright blue and yellow pixels is mapped in area B. There is a gradual change from blue to yellow towards the center of this area showing a change from jarosite to hematite-goethite mixture. In the area C iron oxide pixels are outlining the scarp and also the argillic classes mapped previously towards the center.

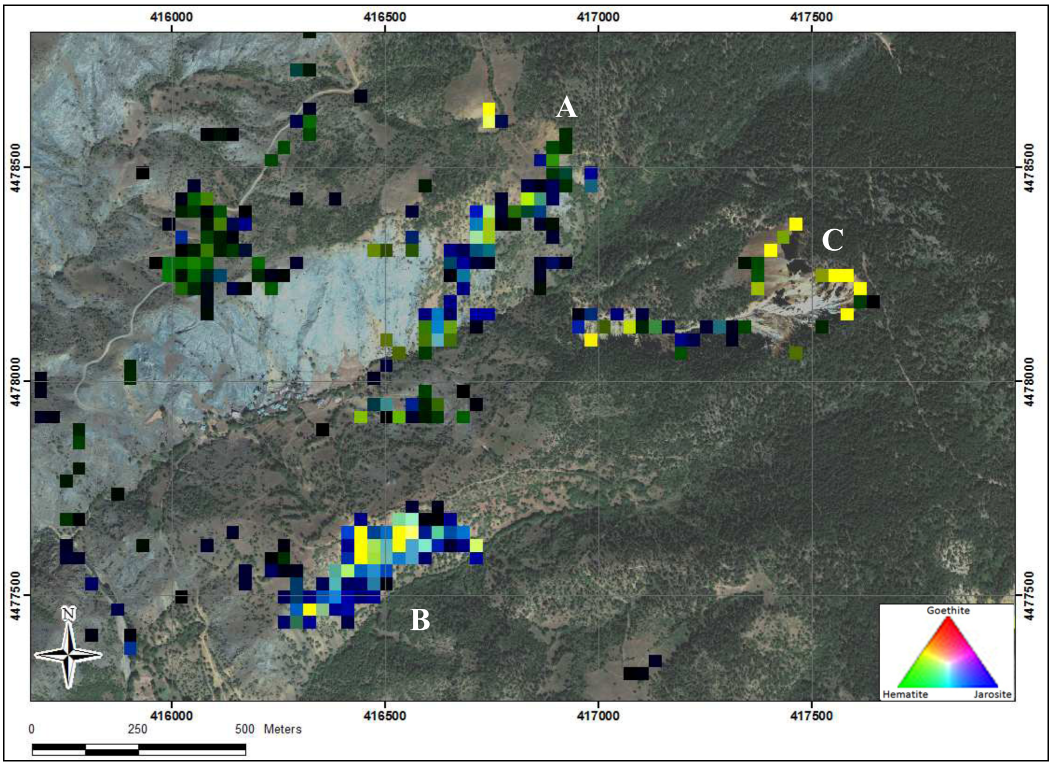

Figure 5.8 Region 1 Iron oxide group of endmembers.

Main zone in region 2 shows yellow and blue pixels outlining the scarp (Figure 5.9). Goethite and hematite mixture is mapped just along the scarp boundaries and jarositic response is observed in parallel alignment with the stream valley.

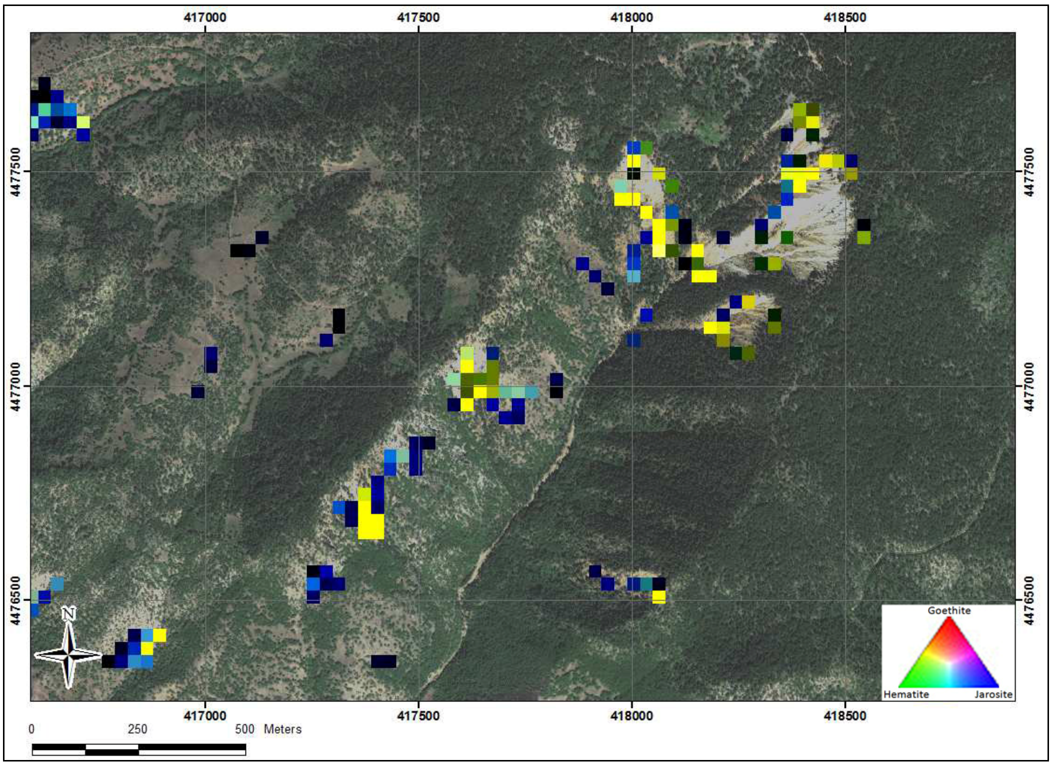

Figure 5.9 Region 2 Iron oxide group of endmembers.

With a little dark green exposure region 3 is also dominated by bright blue and yellow pixels (Figure 5.10). Area D has the highest density of pixels in the whole region. Jarositic response at the boundaries with blue pixels changes to a goethite-hematite mixture towards the center. At the center of the area white pixels denotes responsive mixture of three endmembers. Dark green, hematitic response is mapped in area E with jarosite outlining the area. Also a linear yellow trend of goethite-hematite mixture is identified in this area. Area F shows the highest number of pixels identified compared with argillic group of endmembers. Blue pixels dominate this area with varying tones depicting a jarositic character with minor goethite-hematite mixture.

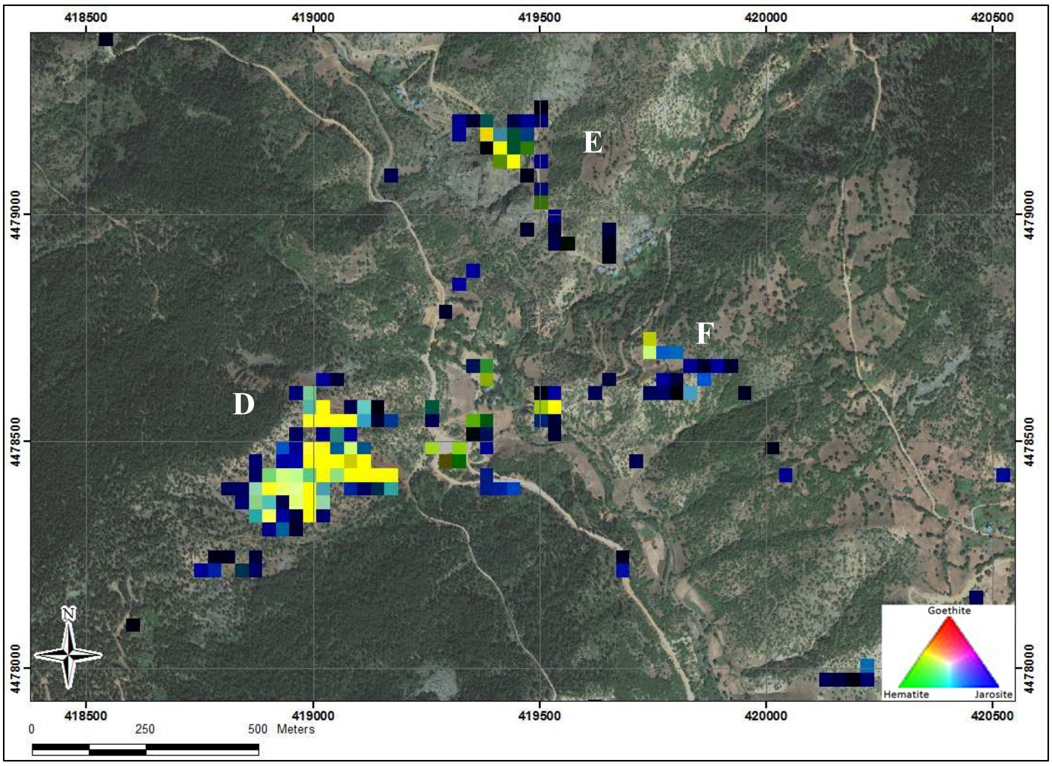

Figure 5.10 Region 3 Iron oxide group of endmembers.

5.3.4 Comparing Results with Geology

Classification results of argillic and iron oxide groups are given in the previous sections taking individual endmembers into consideration. In order to obtain the mineral associations in a combined way, the endmembers are added by band addition for three groups. The output images are thresholded for values greater than 2.7 out of 3. Maximum value, 3 denotes the pixels having perfect correlation for all endmembers for the respective group, meaning a perfect mixture. The results are mapped for three regions together with the alteration information explained in second chapter of the thesis.

The alterations identified by ASD survey is used as an additional tool to the field observations on identifying the alteration types. Therefore, for the six clay endmembers the ASD readings are converted to a qualitative grid displayed in Figure 5.11. The overlay of clay polygons in the figure displays a good correlation in the three regions with the grid. It should be noted here the grid space is not regular and due to the nature of interpolation it is only used for visual interpretation.

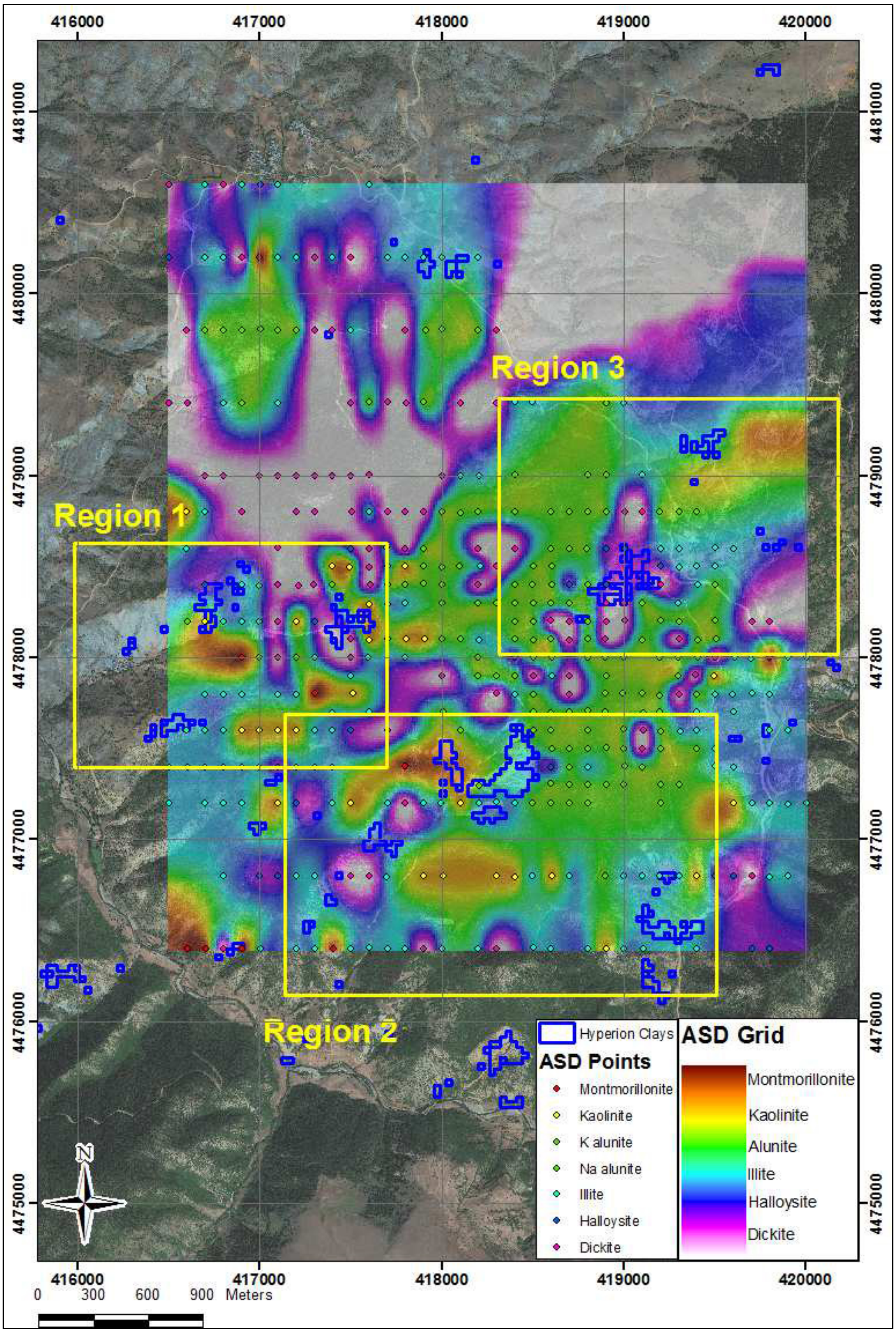

Figure 5.11 Overlay of ASD results and the Hyperion clay group polygons.

In Region 1, there is a very significant overlap between the mapped alteration and the Hyperion derived alteration polygons in area C. Clay polygons are almost wholly included in the argillic altered mapped area. Iron oxide polygons surround the clay polygons and the mapped ferricrete displays this association. Parallel alignment of the image polygons and the northeast structures also gives an important clue on the structural control in alteration (Figure 5.12).

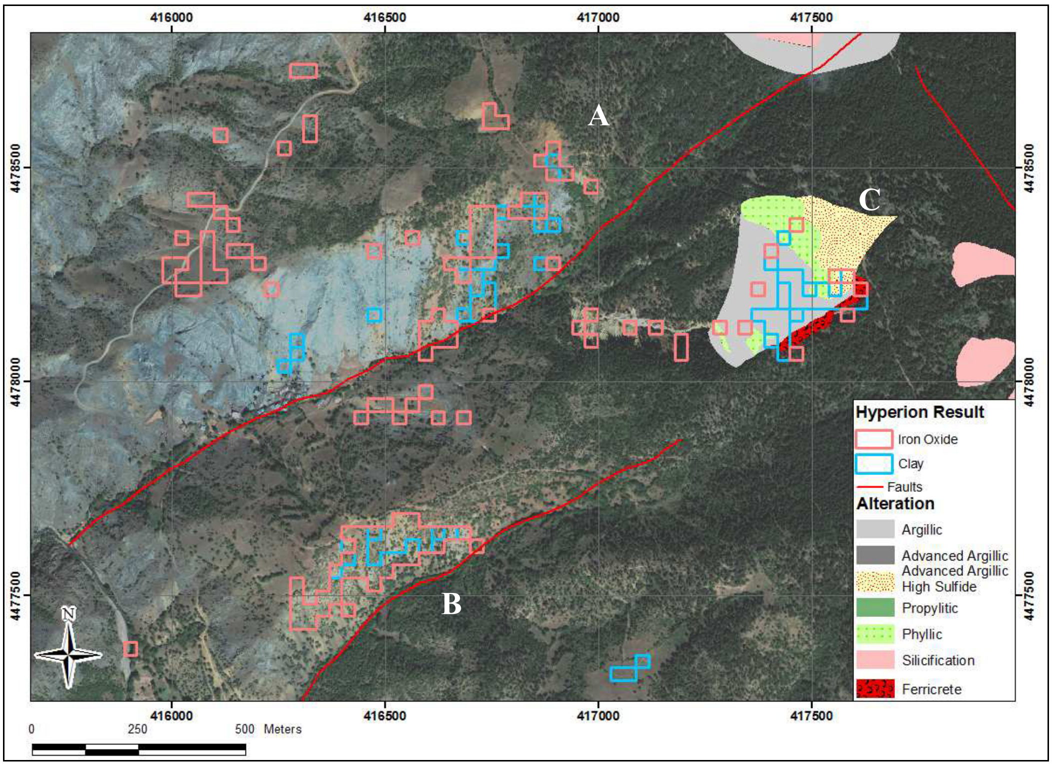

Figure 5.12 Comparison of image polygons with alteration map for region 1.

The main alteration zone in region 2 is identified as argillic both by field map and the image polygons. The clay mixture is dominant with the weak surrounding oxidation. Both the valley and the scarp are again in the control of northeast trending fault and the polygons are in same alignment (Figure 5.13).

The most responsive area in region 3 is area D and it displays an important overlap with the mapped phyllic alteration. As in definition (chapter 2), phyllic alteration also has clay minerals associated. Also an overlap of Hyperion polygons of ironoxide and clay groups is shown (Figure 5.14).

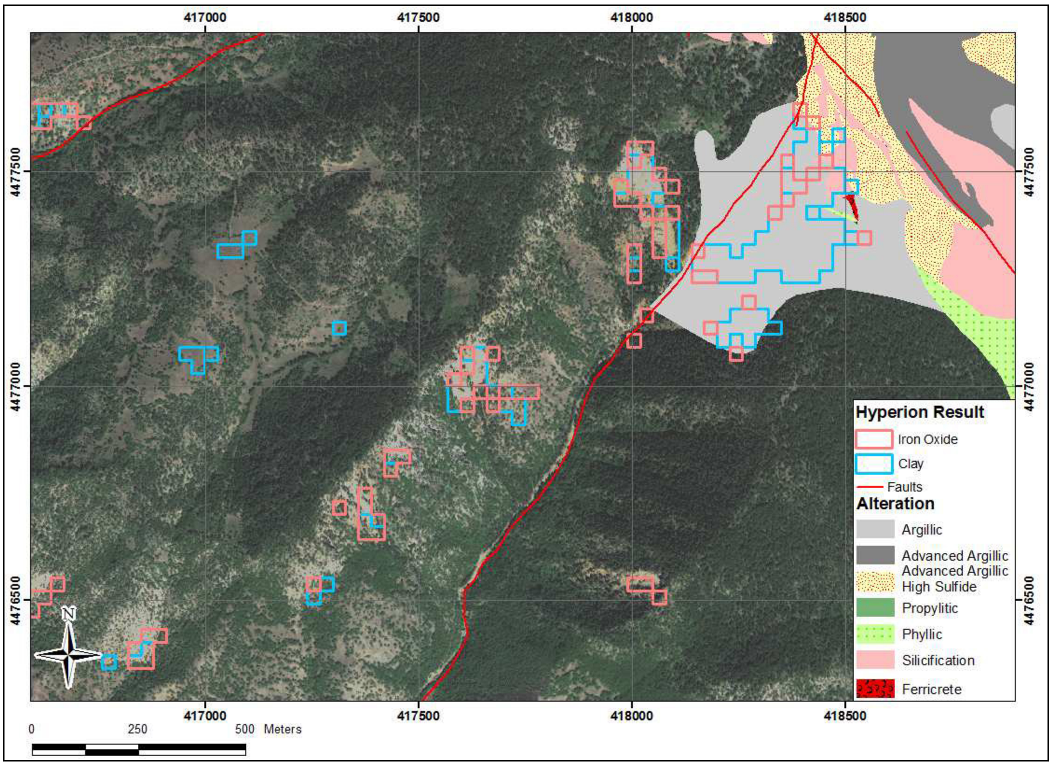

Figure 5.13 Comparison of image polygons with alteration map for region 2.

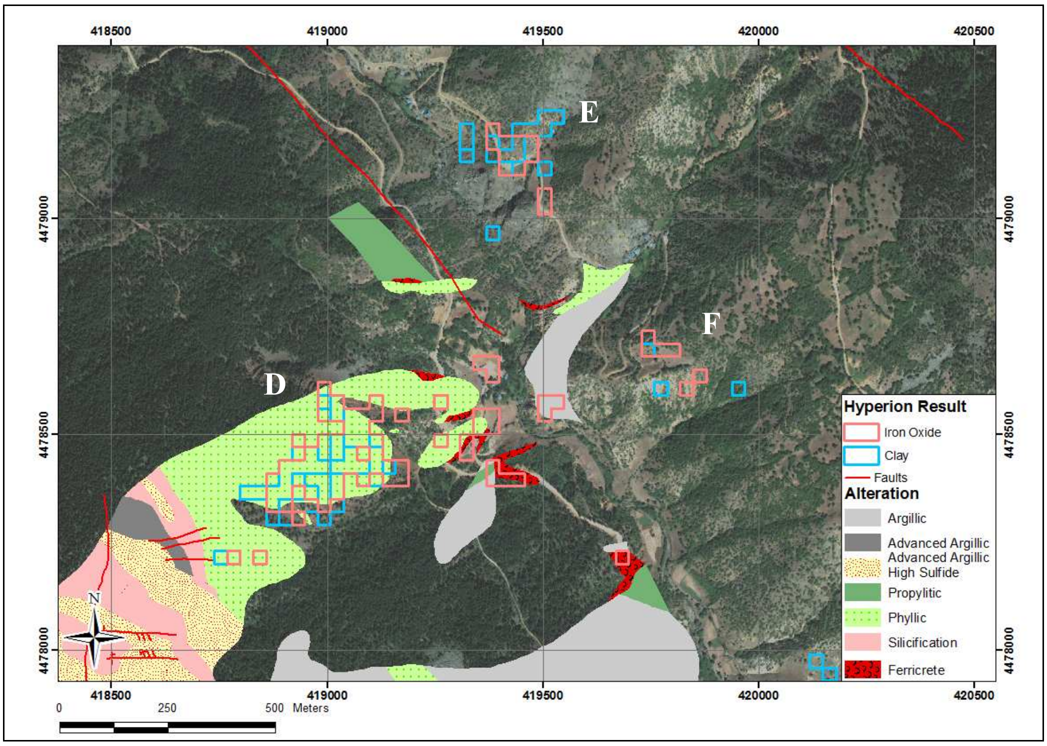

Figure 5.14 Comparison of image polygons with alteration map for region 3.

In Figures 5.15 to 5.17 field photos are given. Photos give field looks of regions explained in previous section with wide angle and close ups where available.

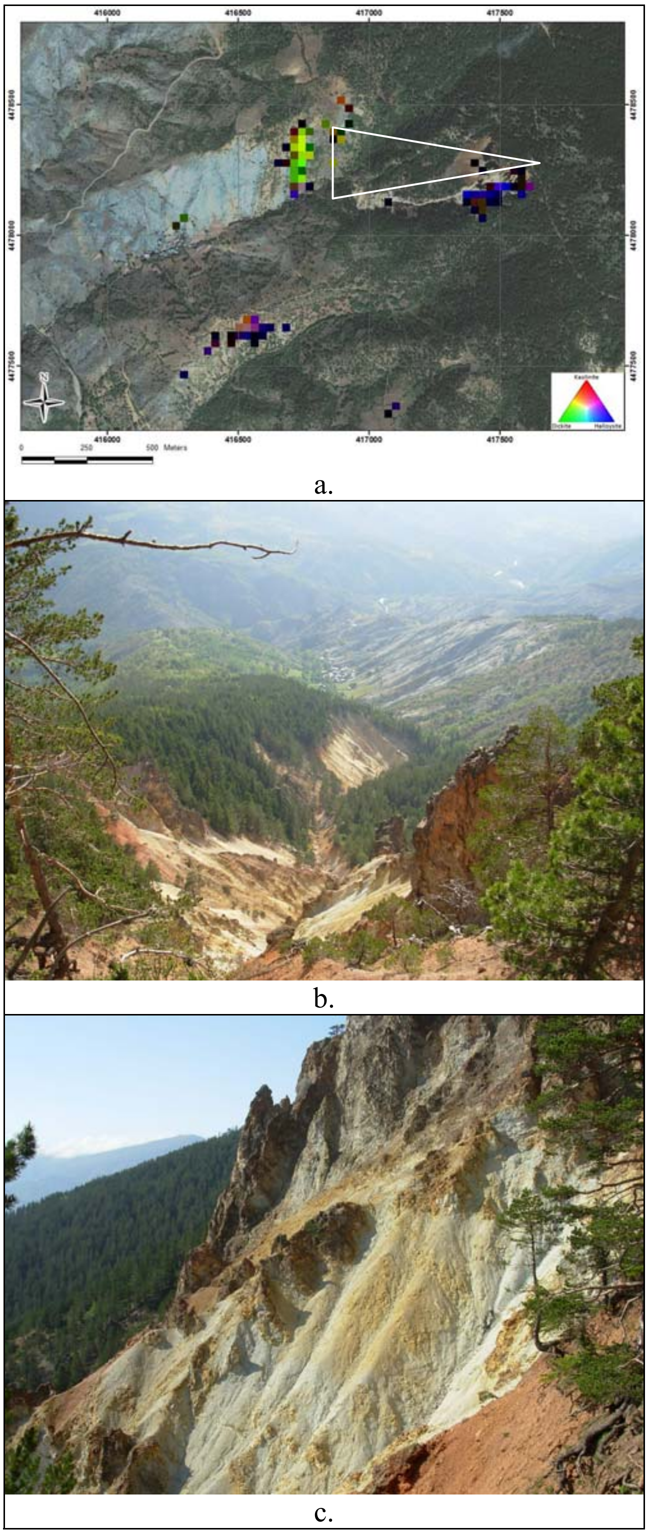

Figure 5.15 Field photos of Region 1. a. Photo location with field of view, b. general view, and c. detailed outcrop

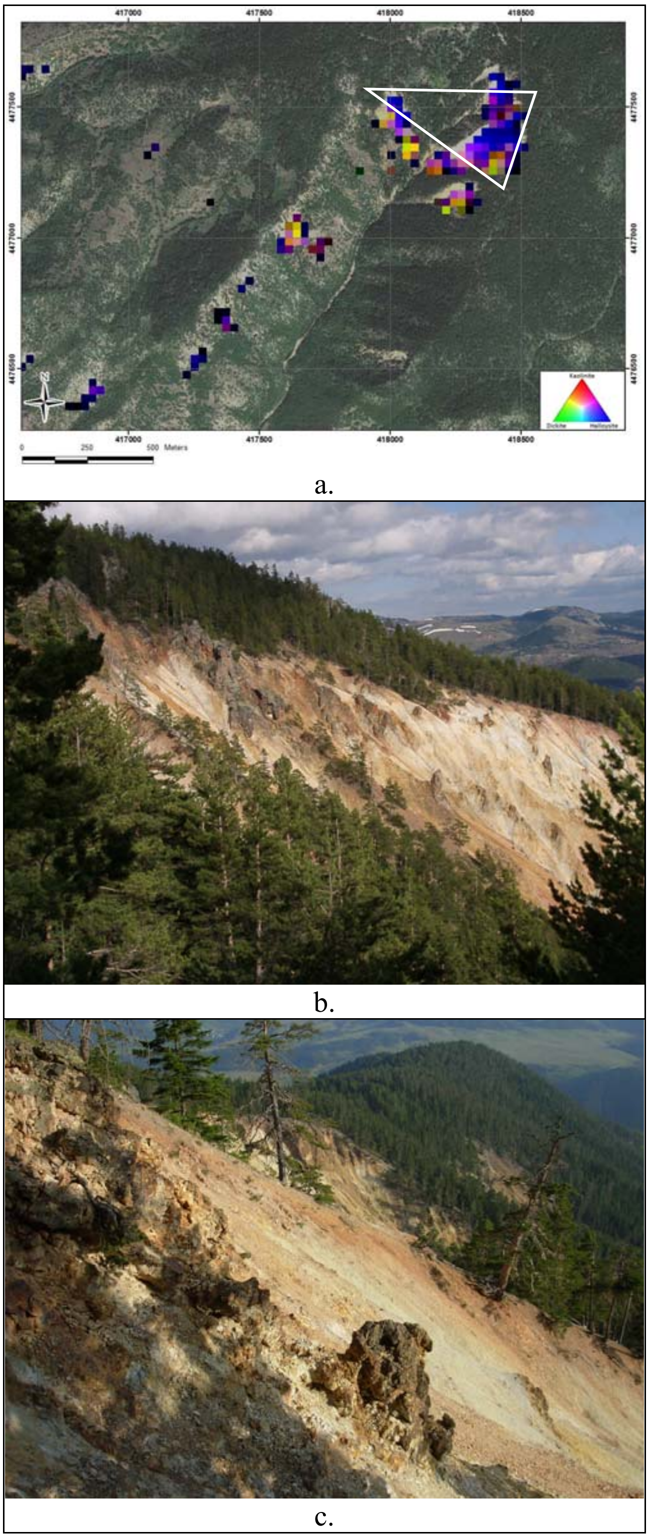

a.

b.

c.

Figure 5.16 Field photos of Region 2. a. Photo location with field of view, b. general view, and c. detailed outcrop

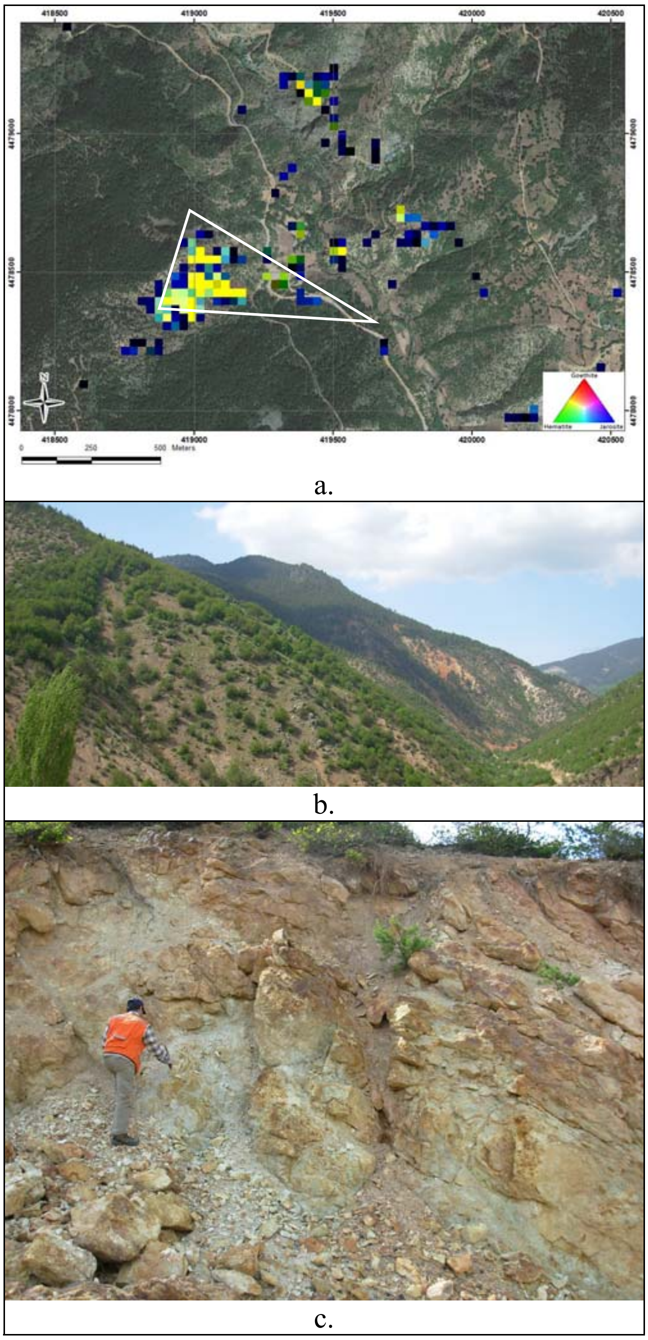

Figure 5.17 Field photos of Region 3. a. Photo location with field of view, b. general view, and c. detailed outcrop

CHAPTER 6

CONCLUSIONS

6.1 Conclusions

Hyperion, being an experimental satellite based hyperspectral imaging system has certain restrictions generated from its “experimental” nature. High spectral resolution in a satellite system is a very important technological improvement for letting the use of spectrometric measurements made on the ground. Hyperion image has high spectral resolution with a low signal quality. So much effort is given to get the useful information out of Hyperion with applying sensor specific corrections and models. The combination of low signal quality and low spatial resolution is not preferred while researching for a ground application.

Illumination variation in the cross track direction is accepted as systematic noise for Hyperion and standardly should be removed on the first part. Cloud and shadow on the other hand can be found on any satellite and/or airborne image dataset. Applied methods can be used as a base for detecting cloud and shadow in other satellite image data.

With the current specifications Hyperion is not a good data source to be used as a standard image product for ground applications like alteration identification.

The study area is selected on the basis of good ground control data by means of maps and survey data. The collection of ground control data is very important on validation and interpretation of results. Use of field spectrometer is a very powerful tool to correlate image with the ground.

The alteration types mapped in the field are not all identified from the image data. Epidote, chlorite, sericite and silica are eliminated. For the selected endmembers mainly clay and iron oxide minerals are grouped together. High correlations between image and ground data for these groups are recorded. In major alteration zones that are exposed in fault related scarps the argillic mixture is identified agreeing the field alteration map. Interestingly the iron oxides are mapped on the borders of these fault scarps coinciding with the ferricrete outcrops mapped. In main alteration zone the linear alignment of mineral groups also verified the structural control.

The unmixing methods show that Hyperion is not an appropriate data set for straight forward algorithms like LSU. Advanced use of MTMF parameters are very valuable on testing and updating the processing steps. As MTMF included the use of MNF transformed data, noise is still the part of the unmixing procedure. With the issues in Hyperion signal quality, final classification is made by SCM rather than unmixing and interpreted directly with the correlation values.

Hyperion data set is not designed for ground applications with high precision. This study demonstrates the steps to correct and evaluate the image data. In all aspects the described routines can form the basis of a similar study but for different Hyperion image sets modifications may arise.

6.2 Recommendations for Further Study

Unmixing algorithms are more convenient than classification techniques in order to map distribution of alteration with airborne imaging systems. The automated integration of unmixing and classification methods is important to standardize the procedure.

New ways to increase the SNR values for Hyperion is needed. Data fusion with other sensors can help understand and remediate the noisy image data.

REFERENCES

Adamia, S. A., Chkhotva, Mb., Kekelia, M., Lord, M., Shavishvili, I. and Zachariadze, G., 1981. Tectonics of the Caucasus and Adjoining Regions: Implications of the Evaluation of the Tethys Ocean, *Jour. Struct. Geol. Vol. 3, p. 437-447.*

Akın, H., 1979, Geologie, Magmatismus und Lagerstättenbildung im Ostpontischen Gebirge/Türkei aus der Sicht der Plattentektonik, *Geol. Rdschau. 68, 253-283.*

Akıncı, Ö.T., 1980, "Major Copper Metallogenic Units and Genetic Igneous Complexes of Turkey", *Soc. Geol. Applied to Mineral Deposits Spec. Pub. 1, 199-208.*

Akıncı, Ö.T., 1984, The Eastern Pontide volcano-sedimentary belt and associated massive sulphide deposits, *in* J.E. Dixon and A.H.F. Robertson, eds., The Geological Evolution of the Eastern Mediterranean: *Geological Society Special Publication, no. 17, p. 415-428.*

ASD, 2009, Product specifications – LabSpec. *http://www.asdi.com/products/labspec-2500-2600.*

Beane, R.E., 1982, Hydrothermal alteration in silicate rocks, southwestern North America *in* Titley, S. R., ed., Advances in Geology of the Porphyry Copper Deposits, Southwestern North America: Tucson, *Univ. Ariz. Press, Chapter 6.*

Bedi, Y., 1998, Geology of the region between Mesudiye (Ordu)-Ortakent (Koyulhisar-Sivas) and the Petrographical-Geochemical analysis of the magmatic rocks, *Ph. D. Thesis, Selçuk University, 193 s*.

Bektaş, O., 1984, The shoshonitic volcanism of Upper Cretaceous age in Eastern Pontides and its geotectonic importance: *Karadeniz University, Earth Sciences Bull., 3, 1-2, 53-62 (in Turkish)*, Trabzon-Turkey.

Boardman, J.W. F.A. Kruse, and R.O. Green, 1995, Mapping target signatures via partial unmixing of AVIRIS data. In *Proceedings, Sixth AVIRIS Airborne Geoscience Workshop*. JPL Publication 95-1. 1:23-26.

Chadwick, T., 2005, Geology of Sisorta prospect, *Eurasian Minerals Inc. report*.

Christian, B., Krishnayya, N.S.R., 2007, Spectral signatures of teak (Tectona grandis L.) using hyperspectral (EO-1) data, *Current Science*, vol. 93, No. 9.

Clark, R. N., 1999, Chapter 1: Spectroscopy of Rocks and Minerals, and Principles of Spectroscopy, in Manual of Remote Sensing, Volume 3, *Remote Sensing for the Earth Sciences*, (A.N. Rencz, ed.) John Wiley and Sons, New York, p 3- 58.

Clark, R. N., G. A. Swayze, K. E. Livo, R. F. Kokaly, S. J. Sutley, J. B. Dalton, R. R. McDougal, and C. A. Gent, 2003, Imaging spectroscopy: Earth and planetary remote sensing with the USGS Tetracorder and expert systems, *J. Geophys. Res.*, 108(E12), 5131.

Coulter, D. W., 2006, Remote Sensing Analysis of Alteration Mineralogy Associated with Natural Acid Drainage in the Grizzly Peak Caldera, Sawatch Range, Colorado, PhD. Thesis, *Colorado School of Mines, Colorado, USA.*

Çakır, M. and Kesgin, Ö., 1999, Evliya Tepe (Ortakent – Koyulhisar – Sivas) Altın Yatağı Maden Jeolojisi Raporu, *MTA report No. 10217*, MTA, Ankara Files.

De Backer, S., P. Kempeneers, W. Debruyn, P. Scheunders, 2005, A band selection technique for spectral classification. *IEEE Geoscience and Remote Sensing Letters*. 2 (3): 319-323.

Goetz, A.F.H, G. Vane, J.E. Solomon, and B.N. Rock, 1985, *Imaging spectrometry for earth remote sensing, Science,* 228, 1147-1153.

Green, A.A., M. Berman, P. Switzer, and M.D. Craig. 1988. A transformation for ordering multispectral data in terms of image quality with implications for noise removal. *IEEE Transactions on Geoscience and Remote Sensing*. 26(1):65-74.

Guilbert, M. John, Park, F. Charles, 1986. *The Geology of Ore Deposits*. W.H. Freeman, New York.

Harsanyi, J.C. and C.I. Chang. 1994. Hyperspectral image classification and dimensionality reduction: an orthogonal subspace projection approach. *IEEE Transactions on Geoscience and Remote Sensing*. 32:779-785.

Hunt, G.R., 1982, Spectroscopic properties of rocks and minerals, *in Handbook of Physical properties of rocks, Volume I*, (R. S. Carmichael, ed.) CRC Press, Boca Raton, 295-385.

Hyperteach, 2006. Training in Imaging Spectroscopy, *Belgian Science Policy*, 63-70.

Ketin, İ., 1966, Tectonic units of Anatolia. *MTA Bull.*, 66, 23-34.

Khain, V. E., 1984. The Alpine-Mediterranean Fold Belt of the USSR: *Episodes, Vol. 7/3 p. 20-29.*

Landgrebe, D. A., 2003, *Signal Theory Methods in Multispectral Remote Sensing,* John Wiley and Sons, Inc., Hoboken, New Jersey, USA, 508 p.

Lowell, J. D., and Guilbert, J. M., 1970, Lateral and vertical alteration-mineralization zoning in porphyry ore deposits: *Econ. Geol. 65, 373-408.*

Oo, K.S., 2007, Digital Surface Model based Image Matching for Image Registration, *Geoinformation Forum Japan 2007, Applications of surveying Technologies.*

Pearlman, J. S., Barry P. S., Segal C. C., Shepanski J., Beiso D. and Carman S. L., 2003, Hyperion, a Space-Based Imaging Spectrometer, *IEEE Transactions on Geoscience and Remote Sensing,* vol. 41, No.6.

Pima, 2009, Product specifications – Pima. *http://www.pimausa.com/pima2.html*

RSI 2005a. *ENVI User's Guide – 4.2*. Research Systems Incorporated. Boulder, Colorado.

San, B. T., 2008, Hyperspectral Image Processing of EO-1 Hyperion Data For Lithological and Mineralogical Mapping, PhD. Thesis, *Middle East Technical University, Ankara, Turkey.*

Schneider, H. J. and Özgür, N., 1988. Relationship between Alteration, Rare Earth Element Distribution and Mineralization of the Murgul Copper Deposit, Northeastern Turkey, *Econ. Geol., Vol. 83, p. 1238-1246.*

Soylu, M. 1999. Modeling of Porphyry Copper Mineralization of the Eastern Pontides. PhD. Thesis. *Middle East Technical University, Ankara, Turkey.*

Tokel, S., 1977. Doğu Karadeniz Bölgesinde Eosen Yaşlı Kalk-alkalen Andezitler ve Jeotektonizma, *TJK Bül., Vol. 20, p. 49-54.*

Şengör, A. M. C., Yılmaz, Y. and Ketin İ., 1980. Remnant of a Pre-Late Jurassic Ocean in Northern Turkey: Fragments of Permian-Triassic Paleo-Tethys?, *Geol. Soc., America Bull. Vol. 91/1, p. 599-609.*

Van der Meer, F. and Bakker, W., 1998. Validated surface mineralogy from high-spectral resolution remote sensing: a review and a novel approach applied to gold exploration using AVIRIS data. *Terra Nova, Vol. 10, No. 2, 112-19.*

Van der Meer, F.D. 2000. Imaging spectrometry for geological applications. *Encyclopedia of Analytical Chemistry, Applications of Instrumental Methods, Remote Sensing.* (R.A. Meyers gen. ed., P.M. Mather section ed.). J. Wiley & Sons Ltd. Chinchester, UK.

Van der Meer, F.D., 2004. Analysis of spectral absorption features in hyperspectral imagery. International journal of applied earth observation and geoinformation : *JAG, 5-1, pp. 55-68.*

Van der Meer, F.D., 2006. The effectiveness of spectral similarity measures for the analysis of hyperspectral imagery. *International Journal of Applied Earth Observation and Geoinformation* 8:3-17.

Vigar, J. A., Meldrum S., Giroux G., Soylu M., 2009, Technical Report on the exploration results and resource estimates for the Sisorta property Sivas province, Turkey, *Mining Associates Pty Limited NI-43101 Report.*

Yetkin, E., 2003. Alteration Mapping by Remote Sensing: Application to Hasandağ-Melendiz Volcanic Complex, M. Sc. Thesis, *Middle East Technical University, Ankara, Turkey*, 97 pgs

VITA

ERDEM YETKİN

Date and Place of Birth: 1978, Ankara
Marital Status: Single
e-mail: erdemyet@yahoo.com

EDUCATION

Degree	Institution	Year of Graduation
PhD	METU, Geological Engineering	2009
MS	METU, Geological Engineering	2003
BS	METU, Geological Engineering	2000
High School	Gazi Anatolian High School	1996

WORK EXPERIENCE

Year	Place	Enrollment
2009-Recent	Independent Consultant	Remote Sensing & GIS Geologist
2003-2009	Eurasia Madencilik Ltd. Şti. (Ankara)	Remote Sensing & GIS Geologist
2002-2003	Mineral Madencilik ve İnşaat Ltd. Şti.(Ankara)	Field Exploration Geologist
2000-2002	Hava Toprak Su Environment & Consultancy (Ankara)	On Site Health & Safety Engineer

PUBLICATIONS

Yetkin E., Toprak V., Süzen M.L, 2004, Alteration Mapping by Remote Sensing: Application to Hasandağ – Melendiz Volcanic Complex, Central Turkey, XXth ISPRS Congress, Istanbul, p. 385.

Yetkin, E., 2003, Uzaktan Algılama ile Hidrotermal Alterasyon Haritalaması: Kapadokya Volkaniklerine Uygulama, Mersin University 10th Anniversary Geology Symposium, p. 120.

Yetkin, E., 2003. Alteration Mapping by Remote Sensing: Application to Hasandag-Melendiz Volcanic Complex, M. Sc. Thesis, Middle East Technical University, Ankara, Turkey, 97 pgs.